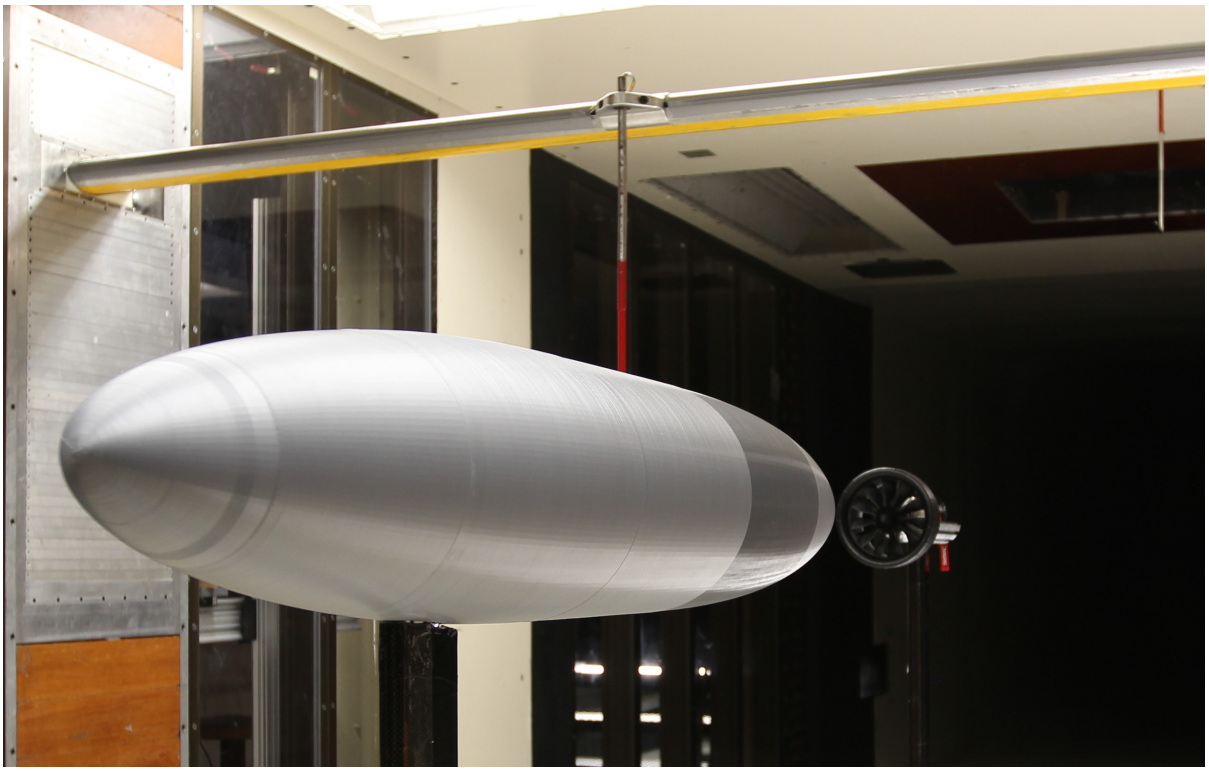

Master of science thesis

Experimental investigation of boundary layer ingestion in integrated propulsion systems

Alan E. Voogd

January 16, 2020

German-Dutch Wind Tunnels

Experimental investigation of boundary layer ingestion in integrated propulsion systems

by

Alan E. Voogd

to obtain the degree of Master of Science in Aerospace Engineering
at Delft University of Technology,
to be defended publicly on Friday January 17th, 2020.

Thesis committee:	Prof. dr. ir. G. Eitelberg,	TU Delft, chair and supervisor
	Dr. A. Gangoli Rao,	TU Delft
	Dr. M. Kotsonis,	TU Delft
	Dr. Ir. R. Habing,	National Aerospace Centre (NLR), daily supervisor

TU Delft

Contents

Abstract

This thesis experimentally assesses the benefit of Boundary Layer Ingestion (BLI) at the unaccelerated condition (thrust equals drag) of an integrated system in an industrial wind tunnel setting. The boundary layer or wake flow of the fuselage is ingested by the propulsor. Previous research shows that ingesting the boundary layer can lead to beneficial savings in terms of power compared to a compared to a non-BLI propulsor. Traditional thrust-bookkeeping methods are not suitable for BLI systems because of the ambiguity between thrust and drag of BLI systems. In order to analyse the performance of such integrated systems the theoretical framework developed by Mark Drela is used: the Power Balance Method (PBM). Furthermore, the classical definition of propulsive efficiency, also named "Froude" efficiency, is not valid for these systems, thus a relatively new propulsive efficiency definition is used.

The wind tunnel tests were carried at the Low Speed Wind tunnel (LST) from the German-Dutch Wind tunnels (DNW) located in Marknesse. Four different configurations were tested in the wind tunnel: i) isolated propulsor, ii) isolated propulsor including an upstream strut, iii) BLI configuration and iv) Wake Ingestion (WI) configuration. The isolated propulsor, simply a propulsor in free-stream flow, is used as a reference to compare with the BLI system. The unaccelerated condition at which these systems were tested is at Mach number $M = 0.176$. The mechanical flow power, jet dissipation and propulsive efficiency are quantified experimentally by using a five-hole probe. Other relevant physical parameters are also measured such revolutions per minute (RPM), thrust and body drag. The designed fuselage is axisymmetric simplifying the measurements and computations.

The results from the experiment reveal that BLI systems have power savings around $29\% \pm 2.9\%$ when using the electrical power as a reference compared to the non-BLI system. For WI the power savings are slightly lower $24\% \pm 2.9\%$. Moreover, the power savings have also been computed using the mechanical flow power, but a larger variance has been observed in the results from 29.25% up to 56.27% for the BLI case. The flow specially at the outlet plane is shown to be asymmetric between the starboard and port sides. Furthermore, the jet dissipation decreases up to 78% compared to a non-BLI system. The slow moving wake flow of the fuselage is re-energized leading to a decrease in jet dissipation. The propulsive efficiency increases between 8% to 10% for both BLI and WI configurations compared to the free-stream propulsor.

Acknowledgements

This work would not have been possible without the cooperation of the Royal Dutch National Aerospace Centre (NLR), the German-Dutch Wind Tunnels (DNW) and TU Delft. I'm glad I had the special opportunity to work together with them.

I would like to first thank my supervisor at NLR Remco Habing for giving me the opportunity to work on such a challenging project. You taught me to plan ahead, coordinate and to think what are necessary steps in order to reach my goals.

I would also like to thank my supervisor from TU Delft, Georg Eitelberg, for supporting me and to make me think why certain details are important. I appreciate your valuable feedback and long discussions over the BLI theory.

I'm grateful to DNW's staff at the Low-speed Wind Tunnel for their help with the wind tunnel experiments, in particular Marc Cruellas Bordes, Gerrit Feenstra and Inge Swart.

I would like to thank David Engler Faleiros for his guidance when setting-up the PIV system and for his patience when we found out that the laser was broken. Also, I would like to thank Martijn Tuinstra, Mark-Jan van der Meulen and Jaap Cornelissen for their help with the calibration of the system.

Nomenclature

List of Abbreviations

AFC	Active flow control
BLI	Boundary layer ingestion
CFD	Computational fluid dynamics
CV	Control volume
DNW	German-dutch wind tunnels
LST	DNW's Low speed wind tunnel
NLR	Dutch aerospace centre
PBM	Power balance method
PIV	Particle image velocimetry
PSC	Power savings coefficient
RPM	Revolutions per minute
TP	Trefftz plane
WI	Wake ingestion

Nomenclature

$\bar{\bar{\tau}}$	Viscous stress tensor
$\dot{E}_a$	Wake streamwise kinetic energy deposition rate
$\dot{E}_p$	Wake pressure-defect work rate
$\dot{E}_v$	Wake transverse kinetic energy deposition rate
$\dot{E}_w$	Wake pressure-work and kinetic energy outflow rate
$\dot{h}$	Climb rate
η_o	Overall efficiency
η_p	Propulsive efficiency
γ	Climb angle
$\mathbf{V}$	Flow velocity $\mathbf{V} = \sqrt{(u + V_\infty)^2 + v^2 + w^2}$
Φ	Viscous dissipation rate
Φ_{jet}	Jet dissipation
ρ	Air density
ρ_∞	Air density at free-stream
C_{P_E}	Non-dimensional electric power

C_{P_K}	Non-dimensional mechanical flow power
C_x	Non-dimensional net streamwise force
D_{body}	Body drag
F_x	Net streamwise force
J	Advance ratio
M	Mach number
M_∞	Mach number at free-steam
p	Static pressure
p_∞	Static pressure at free-stream
P_K	Mechanical flow power
P_S	Propulsive shaft power
p_t	Total pressure
P_V	Net pressure-volume power
$p_{t\infty}$	Total pressure at free-stream
Re	Reynolds number
S_{ref}	Reference area
T_{prop}	Thrust of the propulsor
u, v, w	Flow velocity perturbations
V_∞	Free-stream flow velocity
W	Aircraft weight

List of Figures

List of Tables

Chapter 1

Introduction

In 2018 around 4 billion passengers flew to their destinations, the International Air Transport Association (IATA) claimed that the amount of passengers is estimated to double in 2037. (International Air Transport Association, 2018). With the steady rise in number of passengers, it is expected from the aviation industry to manufacture more efficient and quieter aircraft. For the past few decades, there is a steady decline in fuel consumption in the aircraft industry due to several reasons, e.g. by increasing the bypass ratio of turbofan engines, new innovative materials etc.

New research is focusing on propulsion integration. Propulsion integration refers to the interfaces of aerodynamic, structural and other subsystems(hydraulics, electrical, control etc.) between engine and airframe. Nowadays the traditional aircraft configuration is the tube and wing, where the engine is mounted on a pylon. The reason to mount the engine on a pylon is to minimize the effects between the airframe and engine so that the engine has its own aerodynamic characteristics and performance, independent of the aircraft's body. In order to meet the $N + 3$ goals proposed by NASA several new designs are being proposed such as distributed propulsion systems, hybrid propulsion etc. (Committee on Propulsion and Energy Systems to Reduce Commercial Aviation Carbon Emissions, Aeronautics and Space Engineering Board, Division on Engineering and Physical Sciences, & National Academies of Sciences, Engineering, and Medicine, 2016)

Boundary layer ingestion (BLI) is a possible solution for aircraft to become more efficient. Boundary layer ingestion aims to reduce the power consumption and increase the efficiency of the aircraft. The BLI technology has been already investigated for marine propulsion since the 1950s, e.g. in torpedoes (L. H. Smith, 1993). However, unlike for conventional aircraft configurations the thrust and drag cannot be differentiated anymore. This is due to the coupling between the fuselage and engine. This is depicted in Figure 1.1. One can observe on the left hand side (LHS) the uncoupled system, where thrust and drag are clearly defined. On the other hand, in Figure 1.1b the thrust and drag cannot be differentiated anymore. This is a challenge for the industry since conventional thrust-bookkeeping cannot be used anymore. Organizations such as the Dutch Aerospace Centre (NLR) and German-Dutch Wind Tunnels (DNW) are interested in gaining knowledge on the testing and simulation of integrated propulsion systems.

(a) Non-BLI propulsion system. Clear distinction between thrust and drag

(b) BLI propulsion system. Thrust and drag are ambiguous

Figure 1.1: Conventional thrust bookkeeping not possible with highly integrated systems. (Lieu, 2015)

A solution to this problem is to use the Power Balance Method (PBM) developed by Drela in which the focus is on a power and kinetic energy analysis instead of a momentum analysis. In this theory a power balance equation is obtained, where it contains the input power terms such as the input mechanical

flow power, shaft-power and output terms such as the kinetic energy deposition rates, dissipation and potential energy. (Drela, 2009)

The classical definition of propulsive efficiency, also named "Froude" efficiency, is not valid for BLI systems because it can reach values higher than 100%, since it ignores the pressure term in the momentum balance equation. Several new definitions of efficiency have been developed but there is no standard definition to follow. In a recent study published by Hall et al. (2017) a new general propulsive efficiency has been proposed, which does not exceed 100%. The benefit of BLI was known since the late 1940s and has been subject of numerous studies e.g. (A. Smith, 1947)(L. H. Smith, 1993)(Drela, 2009). One way to measure the benefit of BLI systems over non-BLI systems is to compute the Power Saving Coefficient (PSC) which compares the input mechanical power between BLI and non-BLI systems, as was first developed by L. H. Smith (1993).

1 Contributions

The different research objectives that follow from the limitations of the current research status are summarized in this section. The aim of this research is to:

1. Provide guidelines to wind-tunnel test suppliers such as DNW and research institutes such as NLR on the experimental methods for highly integrated propulsion systems.
2. Quantify the BLI benefit at the unaccelerated condition of a highly integrated propulsion system by testing experimentally in an industrial wind tunnel using: the direct method and indirect method. See Section 2.2 for further information on each method. The performance of a BLI system is compared to a non-BLI system.
3. Quantify the effect of the direction of the velocity vector at the inlet and outlet of the propulsor on the mechanical flow power, jet dissipation and consecutively BLI benefit.
4. Quantify the propulsive coefficient of a BLI engine using the definition given in Hall et al. (2017).

2 Research questions

The research questions were formulated after a literature survey which is summarized in Section 2:

- *"For a highly integrated propulsion system with Boundary Layer Ingestion (BLI), what is the effect of the direction of the velocity* $\boldsymbol{V}$ *at the inlet and outlet planes of the propulsor on the magnitude of the mechanical power* P_K *and jet dissipation* Φ_{jet} *defined using the Power Balance Method?"*
- *"What are the effects of the position of the propulsor in Boundary Layer Ingestion (BLI) or Wake Ingestion (WI) on the recent definition of propulsive efficiency presented in Hall et al. (2017)?"*

3 Thesis overview

The thesis is divided in two parts: I) Theory and II) Wind tunnel test. In the first part an introduction to the concept of BLI is presented in Chapter 2 followed by a summary of the most relevant work on BLI. Furthermore Section 2.1 shows the most relevant studies prior to the Power Balance Method, then Section 2.2 shows the studies after Drela's paper published in 2009. Drela's theory is an important distinction since most of the recent papers use his theory to explain and investigate phenomena relating to boundary layer ingestion and integrated propulsion. Then, a detailed description of PBM is described in Section 3. Subsequently, a description of an important parameter to measure the performance of a BLI system, the power savings coefficient, is given in Chapter 3. The last chapter of the theory, Chapter 4, deals with the new definition of propulsive efficiency for BLI systems.
In Part II, Chapter 5 describes the overall experimental set-up. This chapter also includes a description of the test campaign. The processed results from the wind tunnel tests are given in Chapter 6. Moreover, Chapter 7 shows the uncertainty for the computed terms. Lastly, the conclusions are shown in Chapter 8 followed by the recommendations in Chapter 9.

Part I

Theory

Chapter 2

Boundary Layer Ingestion

1 Introduction to BLI

The boundary layer is a thin layer of fluid next to a solid surface such as a flat plate, where the effect of viscosity is significant. Figure 2.1 shows a schematic of a boundary layer of a flat plate. The velocity grows from zero at the surface itself (no-slip condition) and grows to free-stream value away from it. Boundary Layer Ingestion (BLI) as the name indicates is the ingestion of the boundary layer flow through the integrated engine.

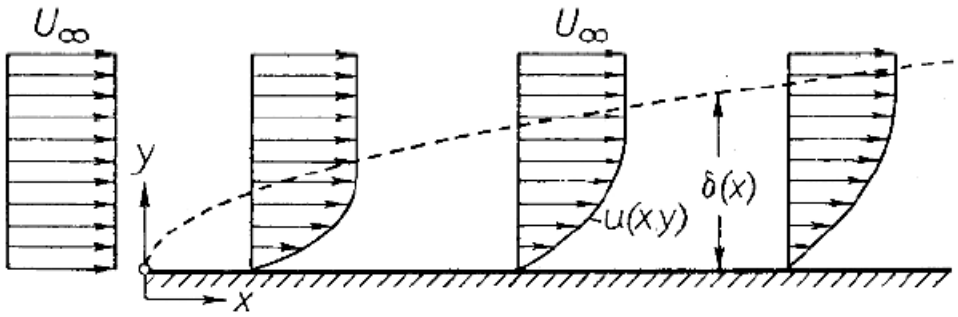

Figure 2.1: Boundary layer growth at flat plane with zero incidence (Schlichting & Gersten, 2016).

Following the theoretical framework developed by Drela (2009) the benefit of BLI is explained as follows. Figure 2.2 shows two aircrafts one with podded engines and one with boundary layer ingesting engines. The kinetic energy of the jet is "wasted" in the podded engine case. However, for the BLI case the engine "fills in" the wake reducing the stream-wise flow velocities and wasted kinetic energy. Thus, the power dissipation is reduced in this case.

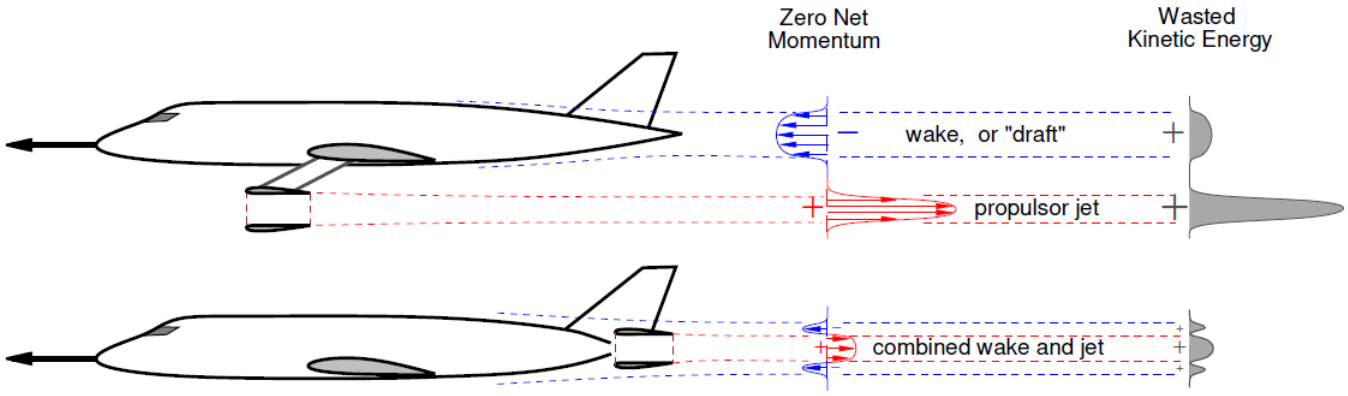

Figure 2.2: BLI reduces the wasted kinetic energy compared to the podded engines case (Uranga et al., 2014)

However, the boundary layer flow is a highly distorted flow which reduces the lifespan of the propulsor's blade.

2 Previous studies on BLI assessment

The evolution on the investigation of the effects boundary layer ingestion is relevant to this research. In this section a literature survey is summarized in two sections: i) from 1950 to 2009 and ii) from 2009 to 2018. A clear distinction has been set at 2009 due to the importance of the PBM which was published in 2009 by Drela and subsequently influenced newly published research. (Drela, 2009)

2.1 Boundary layer ingestion 1950-2009

Boundary layer ingestion was first used for marine applications such as torpedoes and ships. In the field of aircraft engineering, one of the first studies that demonstrated the benefits of BLI for aircraft propulsion was carried out by A. Smith (1947) cited in Plas (2006). In this study, a BL ingesting engine was shown to reduce fuel consumption between 5 to 10%.

In 1962 NASA conducted an investigation of a 1/20 airship model with stern propellers to investigate the characteristics and the effect of propellers on the airship. (McLemore, 1962) These tests were conducted at the NASA Langley full-scale tunnel. The measured characteristics were the propeller thrust and power, aircraft force and moment, fuselage boundary layer and wake characteristics. The results of these tests show a much higher propulsive efficiency than that of a conventional podded propeller.

A study in 1970 investigated the propulsive efficiency of BLI aircraft (Douglass, 1970). Two different cases were investigated, viz. BLI system and a non-BLI system where the ratio of the velocity increment V_e to the flight speed V is kept constant. Douglas assumed: i) incompressible flow, ii) flow at the inlet is at ambient static pressure and iii) one seventh power law profile was used for the ingested boundary layer. The author concluded that BLI is beneficial due to a reduction in Kinetic Energy (KE) of the wake and the jet. Furthermore the maximum improvement in propulsive efficiency for a typical aircraft is stated to be 16%, assuming no losses at the inlet. However, if losses at the inlet are considered and the effect of BLI on the Brayton cycle, the efficiency can be reduced.

L. H. Smith (1993) investigated the benefits of wake ingestion (WI). A method was developed to estimate the propulsive power savings one could achieve when the viscous wake of a body is used as part of the propulsive power. The propulsive power P_p is represented by the kinetic energy flux in the downstream wake, assuming that the wake is at ambient static pressure. Smith in his derivation starts with actuator disk theory for a non-wake ingesting propulsor and eventually accounts for the wake ingestion and other terms. The savings in power of the propulsor can be documented with the so-called *Power Saving*

Coefficient (PSC).

$$PSC = \frac{P'_p - P_p}{P'_p} \tag{2.1}$$

The prime is used when the wake is not ingested. The PSC is an important parameter later used in many studies where the performance of highly integrated propulsion systems are analyzed. Smith also mentions that the previous formulation of propulsive efficiency can exceed 100% thus it should be called coefficient instead of efficiency.
Numerical computations were performed and several conclusions about the power saving were reached: i) the power saving is the largest for small propulsors, ii) the power saving is the greatest when the propulsor is located in a position where the wake has not dissipated or flattened much by the shear stress of the fluid, iii) it is favourable when the wake profile is flattened by reversible energy addition of the propulsor and iv) power savings can be in the range of 20% in some cases.

Plas (2006) in his master thesis in 2006, later continued and published as a paper Plas et al. (2007), presented a performance analysis of an aircraft with highly integrated propulsion with the presence of BLI and flow distortion. In this case an analysis of the fan in ultra high bypass engines is carried with the intention of establishing the flow benefit due to BLI. This benefit is shown to be sensitive to changes in magnitude of fan and duct losses. The results show that BLI can provide a decrease in fuel burn up to 3.8%. The figure of merit used for comparison between BLI and non-BLI systems is the power saving coefficient developed by L. H. Smith (1993). Some other important conclusions from this paper are:

- Flow distortion for aircraft with BLI is a high risk (fan) design concept due to the lack of experience and an investigation is needed to mitigate these risks.
- Ignoring the technical challenges, BLI does achieve a substantial reduction in fuel burn compared to conventional engines.

Kawai, Friedman, and Serrano (2006) from NASA conducted a study focused on determining the potential of highly integrated propulsion systems improvement using BLI inlets and Active Flow Control(AFC). The analysis was performed on a Blended Wing Body aircraft with turbofans mounted on top of the aft side of the aircraft. The different designs proposed were compared to a baseline design: a conventional pylon-mounted turbofan on the aft end of the blended wing body. This study also determined the potential benefits of using AFC with BLI inlets since it reduces the inlet distortion and prevents flow separation which results in reduced ram and viscous drag. Thus also reducing the propulsion integration weight and overall fuel burn. The results show a benefit up to a 10% reduction in fuel burned, if AFC is used combined with BL control to enable a short offset BLI inlet.

2.2 Boundary layer ingestion 2009-2018

With highly integrated systems where the engines and body are highly coupled one cannot differentiate between drag and thrust. Conventional thrust-bookkeeping methods cannot be used. In 2009 Drela (2009) developed the Power Balance Method. The previous authors were focusing on a momentum analysis on the control volume (CV), M.Drela on the other hand focused on mechanical power and kinetic energy of the flow. Therefore this method does not need separate definitions for thrust and drag and it can be used for aircraft optimization of highly coupled systems. This method is further expanded in Section 3. Sato (2012) expands on the PBM by using it to estimate the performance of aircraft configurations with tightly integrated propulsion systems. The PBM was applied to a system-level optimization of a hybrid wing body with a BLI propulsion system. With increasing BLI, the fuel burn of this aircraft is shown to decrease monotonically up to a 11% improvement with respect to a non-BLI aircraft.

A study published by Hardin, Tillman, Sharma, Berton, and Arend (2012) investigated the fuel burn benefits associated with BLI for a generation-after-next (N+2) and propulsion system concepts. A detailed Ultra-High-Bypass (UHB) propulsion with BLI is analyzed using a numerical model where propulsion systems can be simulated. The results of the study show that a 3 to 5% BLI fuel burn benefit can be achieved for N+2 aircraft with respect to the baseline aircraft without BLI, pylon mounted, UHB propulsion system. It is also estimated that N+3 configurations have larger benefits due to higher fractions of boundary layer are ingested.

P. Lv and Rao (2013) investigated the fundamentals of BLI for aircraft with highly integrated propulsion systems. This conceptual analysis, which focuses on the BLI effect of energy saving and the impact

that BLI has on the body drag, uses the PBM as a theoretical framework. The conclusions from this paper show that for BLI systems the wake energy is eliminated and it has a favourable effect even if the body drag remains the same. However, the viscous and pressure drag increase due to the body-propulsor interaction. The Froude efficiency exceeds 100% for BLI systems due to not being the true energy output over the propulsor energy input for the fluid.

Three years later the authors expanded on the previous study. P. Lv, Rao, Ragni, and Veldhuis (2016) present a conceptual study evaluating the performance of WI and BLI systems: propulsors and their associated vehicles. The PBM is used for a power conversion analysis to develop and understand the power-saving mechanism of WI and BLI. It is deduced from this analysis that "the Froude's propulsive efficiency as a figure of merit should be separated from the power conversion efficiency in these configurations". A short analysis of the performance for different cases is presented starting by analyzing a free-stream actuator, then an ideal wake-filling actuator and a general WI actuator, where it is explained why the propulsive efficiency exceeds unity and varies from case to case. In addition, the study presents a more general picture by analyzing the isolated body and the integrated system for both BLI and WI cases.

A study published by Uranga et al. (2014) quantified the aerodynamic benefits of BLI with wind tunnel experiments for the D8 transport aircraft, also called the "double-bubble" concept. The concept can be observed in Figure 2.3. There is significant research on the D8 aircraft regarding BLI as many papers were published later.

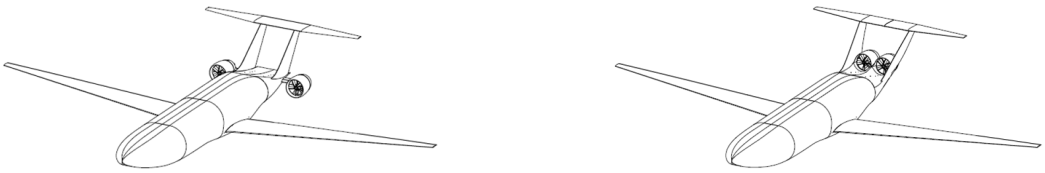

(a) Non-BLI podded propulsion system

(b) BLI propulsion system

Figure 2.3: D8 Aircraft model with BLI propulsors at the NASA Langley subsonic wind tunnel. (Uranga et al., 2014)

Two different configurations were tested, a BLI and a non-BLI concept to compare their performance. These two powered models 1:11 scale and 13.4 ft span were tested at the NASA Langley 14x22 foot subsonic wind tunnel. The two configurations have the same basic airframe (or body) and propulsor units to minimize any other possible effect and focus on quantifying the BLI effects. These two configurations are compared for a zero net streamwise force, which simulates cruise condition. The PBM is used as the theoretical framework to determine the benefit of BLI. It is noteworthy that the PSC, also named BLI Benefit, is computed in terms of electrical power instead of flow power because the flow measurements were not available at the time. The benefit of BLI is quantified as the difference between the mechanical flow power or in this case electric power of the BLI system w.r.t. the non-BLI system divided by the non-BLI mechanical flow power, similar to the definition given by L. H. Smith (1993).

$$\text{PSC} = \frac{{P_K}^{non-BLI} - {P_K}^{BLI}}{{P_K}^{non-BLI}} \simeq \frac{{P_E}^{non-BLI} - {P_E}^{BLI}}{{P_E}^{non-BLI}} \tag{2.2}$$

Where P_K is the mechanical flow power rate and P_E is the electric power. The electrical propulsor power required for cruise is measured, where the model with integrated propulsion requires 6% less power than for the model with podded engines.

Lieu (2015) in his master thesis "*Quantification of the Boundary Layer Ingestion Benefit for the D8-Series Aircraft Using a Pressure Rake System*" presents the results of a set of experiments carried at the NASA Langley Research Center (LaRC) $14'x22'$ subsonic wind tunnel to determine the BLI benefit for the D8 aircraft. In order to compute the PSC, flow surveys were carried at the inlet and outlet of the propulsor using a rotating rake system for both configurations(BLI and non-BLI). These two configurations are analyzed using the PBM. The mechanical flow power at cruise condition (zero net streamwise force) is computed from the flow measurements and CFD computations.
The pressure rakes do not provide the direction of the flow, therefore the flow angles were obtained from

CFD simulations. The power saving can be computed comparing the BLI system with respect to the non-BLI system. The BLI benefit was found to be $8.2\% \pm 0.8\%$. The uncertainties arise from the computation of the flow angles and instrumentation errors, since the pressure rakes do not provide flow angles and cannot properly access the propulsor inlet and outlet planes. Thus, the mechanical flow power cannot be measured directly.

Van Dam (2015) in her master thesis assesses the inflow towards the propulsors and the pressure distribution at the propulsor fan-face for the BLI D8 aircraft, and examines the dependence of the model, the propulsor and the flight condition on the inlet distortion. The experiments are carried out at the NASA Langley subsonic wind tunnel, where five-hole probes were used for pressure surveys and mini-tuft for flow visualization. The results of these experiments are then compared to CFD simulations. The distortion coefficient was computed from the pressure distributions, the maximum variation in pressure of a specified circumferential segment 60 deg:

$$DC(60) = \frac{P_f - P_\theta}{q_f} \tag{2.3}$$

where P_f is the mean total pressure at the propulsor face, P_θ the mean total pressure in the lowest stagnation pressure sector of the face of angle θ and q_f is the free-stream dynamic pressure.
The experiments were analyzed for several mission points: start of climb, top of climb, cruise and descent. CFD was only performed for top of climb and cruise. At cruise the $DC(60) \sim 0.3$ for the D8 aircraft and for conventional aircraft this is usually $DC(60) \sim 0.1 - 0.2$. The larger distortion coefficient is expected due to several reasons:

- The aircraft model, the D8, causes a cross-flow which directs the flow to the side of the model.
- There is an asymmetry between the left and right propulsor regarding the flow direction. This is caused by the rotation of the propulsors, since they rotate in the same direction.
- The engines are conventional engines optimized for uniform free-stream flow, instead for slow and non-uniform BL flow.

The experimental results when compared with CFD show a 1% deviation in $DC(60)$ at top of climb and 6% at cruise. The pressure distributions are similar and the pressure coefficient scale equally.
A recommendation to reduce the distortion is to eliminate the cross-flow induced by the model by changing its design. Furthermore, the engines should be re-designed in order to account for non-uniform flow. Sabo and Drela (2015) presented an experimental study about the propulsive power reduction due to BLI, for an electric ducted fan behind a NACA0040 body of revolution at a Reynolds number of $2.4 \cdot 10^5$. The experiment is carried for a zero net streamwise force, mimicking the cruise condition of an aircraft and its electrical propulsive power is measured. The net streamwise force is computed using a load cell. The PSC for different propulsor positions is computed. The largest power saving is obtained when the ducted fan is closest to the fuselage and centered on the body axis. The experiments were repeated with boundary layer tripping and without tripping. The results show savings for the untripped case are up to 26% and for a tripped flow case 29%. A second iteration of the tests show a maximum power saving of 25% for a tripped flow case. When the propulsor is placed further downstream and away from the body axis, smaller power saving benefits are obtained.
A criticism of this wind tunnel experiment pointed out by professor G. Eitelberg is that only the net streamwise force was measured and not the torque. *When the propulsor is set off the body axis, it produces a torque since the forces are not co-linear anymore. This torque causes the flow to have a certain gradient which is not measured by this balance. One should account for all the forces and moments by measuring with e.g. a 6-components balance.*

Hartuç (2015) investigated and analyzed both BLI and Wake Ingestion (WI) aircraft configurations. In his master thesis different cases where analyzed: free-stream, WI and BLI configurations for their shaft-power saving. The power terms are identified using the PBM and quantified experimentally using PIV at the low-speed wind tunnel of Delft University of Technology. Figure 2.4 shows the different experiments performed at the wind tunnel.

The propulsor in the WI case is placed where the static pressure downstream of the body recovers to ambient conditions. Furthermore the configurations tested are compared using non-dimensional parameters such as propeller efficiency and thrust-power coefficient. The objective is to experimentally quantify the increase in propeller efficiency for the WI and BLI configurations. During the wind tunnel testing two different conditions were set:

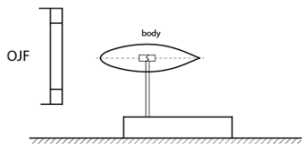

(a) Isolated body

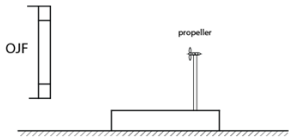

(b) Free-stream propulsor

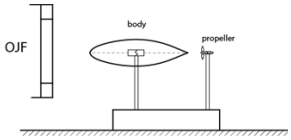

(c) Wake Ingestion

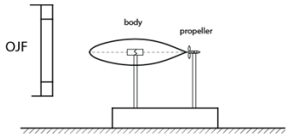

(d) Boundary Layer Ingestion

Figure 2.4: Different configurations tested in Hartuç (2015).

- Equilibrium: the net streamwise force is set to zero. This mimics the cruise condition of the aircraft.
- Constant-speed: the wind-speed is fixed and the thrust of the propulsor varies.

The result for a propulsor in WI configuration saves 9% shaft-power with respect to an identical propulsor in free-stream configuration for the equilibrium case. For BLI the power saving is larger where 18% power saving is measured. The power saving is due to the propulsor being immersed in the slower moving wake. The classical definition of propulsive efficiency for BLI and WI can generate values that exceed 100%. In this thesis several definitions of propulsive efficiency were investigated and one new definition introduced which does not exceed 100% for perfect wake-filling configurations. In the experiment the propulsor and airframe were decoupled, the forces were measured separately thus increasing the uncertainty. Therefore a suggested improvement is to use a common balance between the two systems to find the net streamwise force with lower uncertainty. Furthermore the processing of PIV data required more experience and preparation, leaving no results for the BLI configuration due to this reason. The dynamic pressure of the wind tunnel contains large deviations at very low wind speeds, causing large scatter for non-dimensionalized coefficients.

Uranga et al. (2017) presented a paper assessing the BLI benefit of the D8 aircraft where experiments were carried out from 2010 to 2015 for the NASA N+3 Phase 2 Program. The PSC or BLI benefit is computed for a zero net streamwise force. The net streamwise force is measured using a six-component internal force balance. An important consideration is that *no wind-tunnel corrections were applied to the results of the balance*. This is due to the focus of the research is on relative changes between BLI and non-BLI systems, i.e. the PSC. Since both terms, for BLI and non-BLI systems would have the same wind-tunnel corrections due to having the same blockage and lift coefficient (C_L). Of course, this assumption is only valid if the two geometries considered BLI and non-BLI are very similar. This is the case for the D8 aircraft with podded engines and integrated engines.
Furthermore, the mechanical flow power is measured using two different methods: the direct method and the indirect method.

1. *Direct Method*: The flow field is measured using flow surveys. The details of this method are presented in Lieu (2015).
2. *Indirect Method*: The electrical power of the propulsor is measured during testing and can be converted to mechanical flow power. For this conversion offline experiments are needed in order to compute the shaft and fan efficiencies. The details of this method are presented in Uranga et al. (2014) and Siu (2015).

The results from these two methods give a BLI benefit of 8.6% at cruise condition and it is found to be unchanging to the various modeling and processing assumptions. This benefit is specific for this aircraft where roughly 13% of the total airframe surface viscous dissipation is ingested by the BLI propulsors. A larger benefit is expected with a higher fraction of ingestion. The propulsive efficiency and BLI benefit are evaluated through the mechanical flow power. An important conclusion is that this work presents a BLI benefit of 8.6% but this only represents a fraction of the total potential savings an aircraft could have with BLI, since the aircraft can be optimized e.g. smaller and lighter propulsors can be used, thus

reducing the size of the vertical tail and reducing overall weight. It is estimated that the BLI benefit is close to 19% (Uranga et al., 2014).
Hall et al. (2017) published a paper where the physical principles of the power saving mechanism for BLI propulsion and a quantitative evaluation of BLI benefit for advanced civil aircraft are described. In this paper the PBM is used for the analysis of highly integrated propulsion systems. When defining these systems in terms of power and mechanical energy flow instead of momentum flux and forces one can define relevant physical mechanisms and quantify the performance of integrated propulsion systems. The paper concludes that the principal causes or mechanisms of the benefit that BLI systems provide are:

1. *a reduction in jet dissipation* caused by a lower than free-stream inlet velocity producing the same force with a lower jet velocity
2. *a reduction in airframe viscous flow dissipation* caused by a reduced nacelle wetted area and the addition of energy to the wake fluid.

As mentioned in Uranga et al. (2017) the D8 aircraft has shown a mechanical power reduction of 8.7% due to BLI, where 60% of this benefit comes from a decreased jet dissipation and the other 40% comes from reduced airframe dissipation. However, these results are highly dependent on the fraction of ingested BL, which in this case is 40% of the fuselage boundary layer and the sizing of the propulsion in each configuration. The propulsive efficiency can be quantified using the PBM. *The propulsive efficiency is defined in terms of power quantities and a definition is proposed as "the ratio of net propulsive power to mechanical flow power"* (see equation 4.8) (Hall et al., 2017). The results show that increasing the amount of BL ingested leads to a decrease of the required mechanical flow power. If the mass flow is increased, the propulsive efficiency for both BLI and non-BLI systems is also increased but *BLI systems produce a higher efficiency for the same mass flow.*

In a recent study published by Uranga, Drela, Hall, and Greitzer (2018) a quantitative analysis of the aerodynamic benefit from BLI for transport aircraft is presented. The reduction in jet, wake and surface dissipation are the cause of the aerodynamic benefit of BLI systems. Wind tunnel tests were performed on the D8 aircraft where the BLI analysis framework is applied at the NASA Langley $14x22$ foot subsonic wind tunnel. The comparison between non-BLI and BLI configurations are presented for various cases: equal nozzle area, equal propulsor mass flow, equal jet velocity and equal propulsive efficiency. The power reduction ranges from 4% up to 9% depending on the case.
However there are important considerations regarding the system level benefits, not just BLI benefits. For example, if a BLI and a non-BLI propulsor have equal amount of power, the BLI propulsor would be around 40% smaller in size and considerably lighter. The parametric model presented was applied to subscale, subsonic data, but the modeling equations do not depend on the Reynolds number therefore this model is valid for full-scale aircraft.

3 Power Balance Method

The thrust-bookkeeping method used currently can only be applied to podded nacelles where there is no boundary layer ingestion. The thrust and drag are well defined parameters using the momentum equation. The main body and propulsor can be tested separately to account for drag and thrust respectively. This is illustrated in Figure 2.5. However, in the integrated propulsion system when the airframe and propulsor are highly integrated and BLI is present the contribution of each part cannot be separated, as shown in Figure 2.5. The power balance method is a solution presented by Drela (2009) to asses the performance of highly coupled systems and later expanded by Sato (2012). Instead of focusing on momentum equation analysis, this method focuses on a mechanical power and kinetic energy analysis.

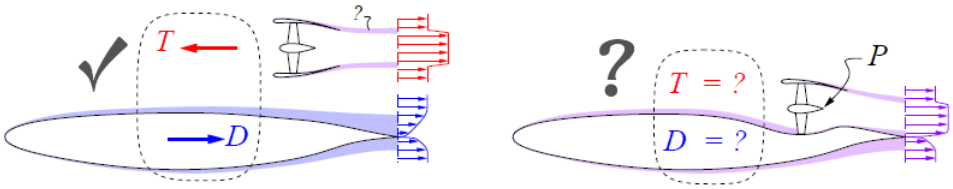

Figure 2.5: Clear definition of thrust and drag for the non-integrated propulsion compared to the boundary layer ingesting system. (Drela, 2009)

3.1 Power Balance equation

The main equation of the Power Balance method is derived in this section. Firstly, the control volume (CV) around an aerodynamic body is defined as can be seen in Figure 2.6. The boundary of the CV, S, is partitioned into two different surfaces:

- The outer boundary S_O which is far away from the body.
- The inner or body boundary S_B which is the surface of the body.

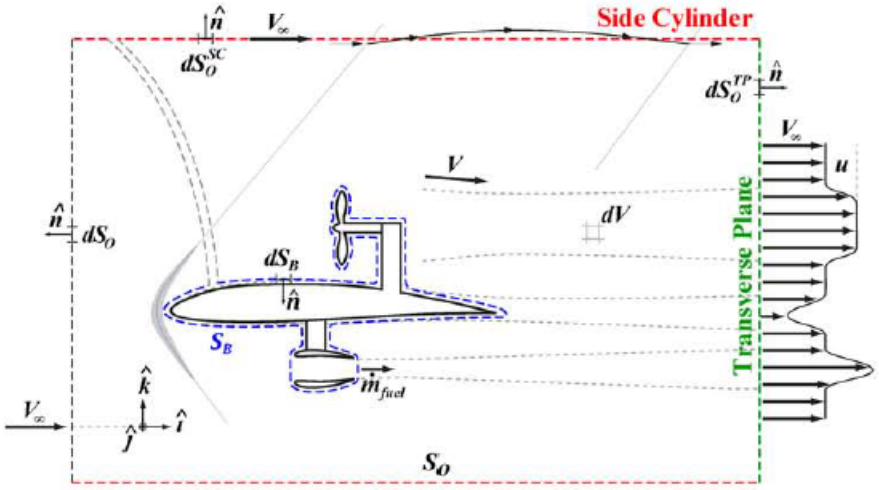

Figure 2.6: Three-dimensional CV surrounding an aerodynamic body from a two-dimensional cutaway view. Modified by S. Sato. (Drela, 2009) (Sato, 2012)

The flow is perturbed by the aerodynamic body, therefore the local fluid velocity $\boldsymbol{V}$ is defined as:

$$\boldsymbol{V} = (u + V_\infty)\hat{X} + v\hat{Y} + w\hat{Z} \tag{2.4}$$

where V_∞ is the magnitude of the free-stream velocity, u, v and w are the perturbations of the free stream velocity in their corresponding directions. The momentum equation in differential form for a compressible flow with no body forces is:

$$\nabla \cdot (\rho \boldsymbol{V}\boldsymbol{V}) = -\nabla p + \nabla \cdot \bar{\bar{\tau}} \tag{2.5}$$

If equation 2.5 is multiplied by dot $\boldsymbol{V}$, then one obtains:

$$\nabla \cdot (\rho \boldsymbol{V} \frac{1}{2} V^2) = -\nabla p \cdot \boldsymbol{V} + (\nabla \cdot \bar{\bar{\tau}}) \cdot \boldsymbol{V} \tag{2.6}$$

One can then integrate equation 2.6 over the whole control volume dV:

$$\iiint_V [\nabla \cdot (\rho \boldsymbol{V} \frac{1}{2} V^2)] dV = \iiint_V [-\nabla p \cdot \boldsymbol{V} + (\nabla \cdot \bar{\bar{\tau}}) \cdot \boldsymbol{V}] dV \tag{2.7}$$

The next step is to apply Gauss Theorem which states that for any continuous vector field $\boldsymbol{A}$:

$$\iiint_V \nabla \cdot \boldsymbol{A} dV = \oiint_{S_O} \boldsymbol{A} \cdot \hat{n} dS_O + \oiint_{S_B} \boldsymbol{A} \cdot \hat{n} dS_B \tag{2.8}$$

The result of applying Gauss theorem and rearranging terms is the power balance equation:

$$P_S + P_V + P_K = W\dot{h} + \dot{E}_a + \dot{E}_v + \dot{E}_p + \dot{E}_w + \Phi \tag{2.9}$$

Where the three terms on the left hand side (LHS) are the mechanical power supply, power inflow to the control volume and power production. The terms on the right hand side (RHS) represent the power outflow and consumption, in other words the mechanical power dissipation, conversion to potential energy and the outflow from the control volume. The definition for each term is:
Propulsive shaft power, P_S

$$P_S = \oiint [-(p - p_\infty)\hat{n} + \bar{\bar{\tau}} \cdot \hat{n}] \cdot \boldsymbol{V} dS_B \tag{2.10}$$

Represents the power provided by components moving relative to the CV, it is the integrated force times velocity over the body CV surface S_B. This term includes positive contributions from a compressor and negative contributions from a turbine, it is only non-zero if the control volume wraps around a moving surface such as propeller blades.
Net pressure-volume "PdV" power, P_V

$$P_V = \iiint (p - p_\infty) \nabla \cdot \boldsymbol{V} dV \tag{2.11}$$

P_V is defined as the volumetric mechanical power (P dV) provided by fluid expanding against atmospheric pressure. This term will only have a contribution wherever heat is added or removed from the flow. For instance combustion can be present inside of the CV.

The net propulsor mechanical energy flow rate into the CV, P_K

$$P_K = \oiint -[(p - p_\infty) + \frac{1}{2}\rho(V^2 - V_\infty^2)]\boldsymbol{V} \cdot \hat{n} dS_B \tag{2.12}$$

P_K is the net pressure power or work rate and kinetic energy inflow rate across S_B and into the CV. This term accounts for the bottom propulsor in Figure 2.6, for power sources whose moving elements are not covered by the body surface boundary.

The potential energy rate $W\dot{h}$ is the power used in increasing the potential energy of the body.

$$W\dot{h} = WV_\infty \sin(\gamma) \tag{2.13}$$

Where γ is the climb angle, $\dot{h}$ the rate of change of altitude and W the weight of the aircraft. When $\dot{h} > 0$ it consumes power, when $\dot{h} < 0$, during descent, it becomes a power source.

Wake streamwise kinetic energy deposition rate, $\dot{E}_a$

$$\dot{E}_a = \iint \frac{1}{2}\rho u^2 (V_\infty + u) dS_O^{TP} \tag{2.14}$$

$\dot{E}_a$ is the rate of streamwise kinetic energy being deposited into the flow out of the CV, through the Trefftz(transverse) plane. This kinetic energy deposition is produced by the wake generated by the body and the jet produced by propulsors.

Wake transverse kinetic energy deposition rate, $\dot{E}_v$

$$\dot{E}_v = \iint \frac{1}{2}\rho(v^2 + w^2)(V_\infty + u) dS_O^{TP} \tag{2.15}$$

$\dot{E}_v$ is the rate of transverse kinetic energy being deposited into the flow out of the CV through the transverse plane. This kinetic energy deposition is produced by the trailing vortex from a lifting body. If the

free stream velocity is much larger than u, $V_\infty >> u$, then equation 2.15 is the same as the induced drag D_i times V_∞. Of course this only holds for a Trefftz plane that is relatively close such that the vortex wake has not dissipated.

Wake pressure-defect work rate, $\dot{E}_p$

$$\dot{E}_p = \iint (p - p_\infty) u dS_O^{TP} \tag{2.16}$$

is the rate of pressure work done on the fluid crossing the Trefftz Plane at the pressure p different from its freestream or ambient value p_∞.

Wave pressure-work and kinetic energy outflow rate, $\dot{E}_w$

$$\dot{E}_w = \iint [p - p_\infty + \frac{1}{2}\rho(u^2 + v^2 + w^2)] \boldsymbol{V} \cdot \hat{n} dS_O^{SC} \tag{2.17}$$

is the pressure work and kinetic energy deposition rate of the fluid crossing the side cylinder (SC). This term becomes only relevant for supersonic flows, where oblique waves are dominant and this term becomes equal to the wave-drag power.

The viscous dissipation rate, Φ

$$\Phi = \iiint (\bar{\bar{\tau}} \cdot \nabla) \cdot \boldsymbol{V} dV \tag{2.18}$$

This term accounts for all the kinetic energy dissipated inside the CV.

Application of the power balance equation

The power balance method is applied over the control volume containing the "aircraft" tested shown in Figure 2.7. The "aircraft" consists of a body which resembles a fuselage and a propulsor behind it. The power balance equation (equation 2.9) is simplified to:

$$P_K = \Phi + \dot{E} - F_x V_\infty \tag{2.19}$$

The only input term in this equation is the mechanical flow power P_K. The system is tested at low subsonic Mach numbers, meaning that incompressible flow can be assumed. Therefore, $\nabla \cdot \mathbf{V} = 0$, thus P_V is zero. Since the control volume does not cover the moving blades of the propulsor, the shaft power (P_S) is not present. For the output terms the total dissipation is present $\Phi + \dot{E}$. In this experiment the system is tested at the unaccelerated condition thus $F_x = 0$. The equation is simplified even further:

$$P_K = \Phi + \dot{E} \tag{2.20}$$

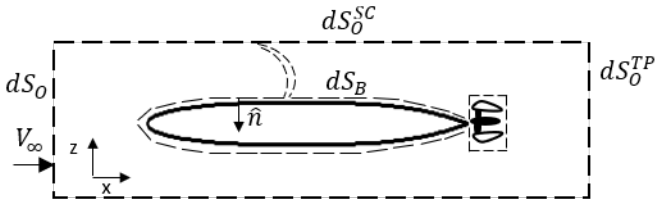

Figure 2.7: Control volume definition for the tested system

Chapter 3

Power Savings Coefficient

One of the methods of evaluating and quantifying the performance of BLI systems is by computing the power savings coefficient. The evaluation of the PSC requires the definition of several parameters. The important term to be investigated is the required power to produce a zero net stream-wise force, since in a fully integrated system it is not possible to differentiate between thrust and drag. For a control volume which fully envelopes the propulsor, assuming a low-speed, the only input power term in the power balance equation is the net mechanical propulsor power P_K.
The net mechanical propulsor power P_K can be defined in terms of total pressure:

$$P_K = -\oiint (p_t - p_{t\infty})\boldsymbol{V} \cdot \hat{n} dS \tag{3.1}$$

where p_t is total pressure. This term can be measured with two different methods, i.e. the indirect and direct method. The direct method consists of surveying the propulsor inflow and outflow planes with flow measurement techniques (e.g. PIV or 5-hole probe). The direct method was used in the experiments of Lieu (2015) where he used a rotating Pt-rake system and calculated the direction of the velocity from CFD calculations. Furthermore, the result can be non-dimensionalized into a power coefficient:

$$C_{P_K} = \frac{P_K}{q_\infty V_\infty S_{ref}} \tag{3.2}$$

The indirect method to compute the BLI benefit is to obtain the propulsor power from the measured electrical power P_E supplied to the motor, combined with the fan efficiency η_f and motor efficiency η_m. This electrical power can be non-dimensionalized:

$$C_{P_E} = \frac{P_E}{q_\infty V_\infty S_{ref}} \tag{3.3}$$

and it can be related to the propulsor power through the efficiencies:

$$C_{P_K} = \eta_f \eta_m C_{P_E} \tag{3.4}$$

The motor efficiency is the power delivered to the shaft divided by the electrical power input to the motor. The fan efficiency is power delivered to the air divided by the shaft power. The disadvantage with this method is that separate experiments are needed to compute these efficiencies and they introduce additional uncertainties when computing C_{P_K}. The overall efficiency can be easily computed and is defined as the ratio between the mechanical flow power and the electric power:

$$\eta_o = \frac{C_{P_K}}{C_{P_E}} \tag{3.5}$$

Since the forces are ambiguous in highly integrated systems, the net stream-wise force F_X is utilized and it can be non-dimensionalized:

$$C_X = \frac{F_X}{q_\infty S_{ref}} \tag{3.6}$$

The definition of the PSC given by L. H. Smith (1993) can be applied to this case, where the objective is to obtain the required power to achieve a zero net-streamwise force:

$$\text{PSC} = \left.\frac{{P_K}^{non-BLI} - {P_K}^{BLI}}{{P_K}^{non-BLI}}\right|_{F_X=0} = \left.\frac{C_{P_K}^{non-BLI} - C_{P_K}^{BLI}}{C_{P_K}^{non-BLI}}\right|_{C_X=0} \tag{3.7}$$

In Uranga et al. (2014), it is assumed that the fan and motor efficiencies are not changing significantly between the BLI and non-BLI configurations for the same operating point. Therefore it is assumed that the benefit can be computed as:

$$\text{PSC} \simeq \left.\frac{C_{P_E}^{non-BLI} - C_{P_E}^{BLI}}{C_{P_E}^{non-BLI}}\right|_{C_X=0} \tag{3.8}$$

Chapter 4

Propulsive efficiency

The classical definition of propulsive efficiency, also named Froude efficiency, exceeds the value of unity for BLI systems (see Section 2.1). Therefore, this definition cannot be applied to such systems because it would suggest to produce energy without any cost. Section 1 introduces the classical definition of propulsive efficiency and Section 2 introduces a new definition based on the power balance method.

1 Propulsive efficiency for a non-BLI system

The propulsive efficiency is a quantitative measure relating the useful power available and the total power generated by a propulsive device as defined in equation 4.1.

$$\eta = \frac{\text{useful power available}}{\text{total power generated}} \tag{4.1}$$

Consider Figure 4.1 where a propulsor is shown ingesting a flow with velocity V_∞ and exiting with velocity V_{exit}. The air from the exhaust can be seen moving with a velocity of $V_{exit} - V_\infty$ and the associated kinetic energy of this air is $\frac{1}{2}m(V_{exit} - V_\infty)^2$. This kinetic energy is completely wasted and the wasted power can be written as $\frac{1}{2}\dot{m}(V_{exit} - V_\infty)^2$, where $\dot{m}$ is the mass flow through the propulsor. On the other hand, the power available provided by a propulsor moving through the air with a velocity V_∞ can be defined as:

$$P_A = T_A V_\infty \tag{4.2}$$

Where T_A is the thrust available. Therefore the total power generated by the propulsor is the sum of the available power and the power wasted. Recalling equation 4.1, the propulsive efficiency is then:

$$\eta = \frac{T_A V_\infty}{T_A V_\infty + \frac{1}{2}\dot{m}(V_{exit} - V_\infty)^2} \tag{4.3}$$

Neglecting the small pressure term, the thrust of the propulsor can be derived to be :

$$T_A = \dot{m}(V_{exit} - V_\infty) \tag{4.4}$$

Substituting 4.4 into equation 4.1:

$$\eta = \frac{\dot{m}(V_{exit} - V_\infty)V_\infty}{\dot{m}(V_{exit} - V_\infty)V_\infty + \frac{1}{2}\dot{m}(V_{exit} - V_\infty)^2} \tag{4.5}$$

Simplifying the equation, one obtains the classical definition of propulsive efficiency or "Froude" propulsive efficiency:

$$\eta = \frac{2}{1 + \frac{V_{exit}}{V_\infty}} \tag{4.6}$$

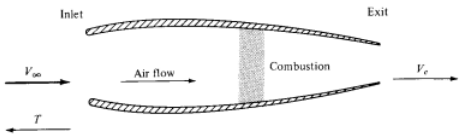

Figure 4.1: Schematic of a jet propulsion engine (Anderson, 2016)

The Froude efficiency shows that a 100% efficiency can be obtained when $V_{exit} = V_\infty$. In other words, imagine that the propulsor moves at a velocity V_∞, the surrounding air is standing still and the air exhausted at the back of the propulsor at a relative velocity V_{exit}. The exhaust velocity is the same velocity at which the propulsor moves $V_\infty = V_{exit}$. This means that a person standing in front of the propulsor sees a propulsor moving at a velocity V_∞ and the air exhausted from the back has no velocity. Therefore there is no wasted kinetic energy. However, if $V_{exit} = V_\infty$ then the propulsor thrust (see Equation 4.4) becomes zero. Therefore a trade-off has to be made depending on the mission in order to have best efficiency and thrust.
Efficiencies higher than 100% can be obtained for $V_{exit} < V_\infty$. This is the case for wind turbines where the flow is decelerated at the back.

2 Propulsive efficiency for a BLI system

Following the classical definition of propulsive efficiency, L. Lv (2019) shows that the propulsive efficiency can reach higher values than 100% for for a general WI system. Other research shows that BLI systems e.g. McLemore (1962) and L. H. Smith (1993), shows high values of propulsive efficiency, requiring to re-define it.

Equation 4.1 still applies for BLI systems. The wind tunnel tests are carried out at low subsonic mach numbers, therefore one can assume incompressible flow and as a consequence the net pressure-volume $P_V = 0$. Furthermore, the moving blades of the propulsor are not covered by the control surface thus the shaft power $P_S = 0$, so only the mechanical flow power is present $P_K \neq 0$. The net propulsive power is defined as the difference between the mechanical flow power P_K and the power lost due to dissipation in the mixing of the jet Φ_{jet}. The mechanical flow power is defined in Equation 3.1 and the jet dissipation is defined as the kinetic energy deposition rate defined at the propulsor outlet:

$$\Phi_{jet} = \dot{E}_a + \dot{E}_v + \dot{E}_p = \iint [\frac{1}{2}\rho(u^2 + v^2 + w^2)(u + V_\infty) + (p - p_\infty)u]dS_{TP} \tag{4.7}$$

Recalling equation 4.1, the propulsive efficiency is defined as the ratio of net propulsive power to mechanical flow power: (Hall et al., 2017)

$$\eta_p = \frac{P_K - \Phi_{jet}}{P_K} \tag{4.8}$$

If there is no dissipation present, the propulsive efficiency is 100%. With this definition the propulsive efficiency cannot exceed values above 100%. Furthermore, if this equation is applied to a non-BLI configuration it reduces to the Froude propulsive efficiency definition. To derive the Froude propulsive efficiency from this equation, a one dimensional analysis is required and a uniform jet velocity V_{jet} at free-stream static pressure is assumed, in the same manner as it was derived in the previous section. The propulsor's mass flow can be defined as:

$$\dot{m} = \rho V_{jet} S_{jet} \tag{4.9}$$

The mechanical flow power at the inlet is zero since the propulsor ingests free-stream flow velocity. At the outlet the mechanical flow power is:

$$P_{K,f} = \frac{1}{2}\dot{m}(V_{jet}^2 - V_\infty^2) \tag{4.10}$$

The jet dissipation on the other hand is equal to the excess mechanical energy deposition rate at the propulsor's outlet:

$$\Phi_{jet,f} = \frac{1}{2}\dot{m}(V_{jet} - V_\infty)^2 \tag{4.11}$$

Substituting equations 4.10 and 4.11 in equation 4.8 and simplifying the terms:

$$\eta_{p,froude} = \frac{P_{K,f} - \Phi_{jet,f}}{P_{K,f}} = \frac{\frac{1}{2}\dot{m}(V_{jet}^2 - V_\infty^2) - \frac{1}{2}\dot{m}(V_{jet} - V_\infty)^2}{\frac{1}{2}\dot{m}(V_{jet}^2 - V_\infty^2)} = \frac{2}{1 + \frac{V_{exit}}{V_\infty}} \tag{4.12}$$

Results in the Froude propulsive efficiency definition.

Part II

Wind Tunnel Test

Chapter 5

Experimental set-up

This chapter describes the set-up of the wind tunnel tests performed to study the effects of boundary layer ingestion. Firstly, an overview of the test campaign is shown in Section 1, followed by a description of the wind tunnel facilities in Section 2. Subsequently, the wind tunnel model is described including a detailed explanation of the design process in Section 3. The instrumentation used during the experiments is discussed in Section 4 also including a brief explanation of the data processing.

1 Test campaign overview

In this section an overview of the test campaign is described. Firstly, this thesis applies the Power Balance Method (explained in Chapter 2) in order to understand and compute important performance parameters for integrated systems where BLI occurs. In order to answer the research questions stated in Chapter 1 the most important parameters needed to be derived are: the mechanical flow power P_K defined in equation 3.1, the jet dissipation Φ_{jet} defined in equation 4.7, the PSC defined in equation 3.7 and finally the propulsive efficiency η_{jet} defined in equation 4.8. To derive these terms a suitable experiment has been designed with proper instrumentation.
The condition chosen to be tested is the unaccelerated case, where thrust equals drag, and where the Mach number equals 0.176, roughly the free-stream flow velocity is $60 m/s$ for standard atmospheric conditions. Five different configurations are tested:

- Isolated body, see Figure 5.1.
- Isolated propulsor, see Figure 5.2.
- Isolated propulsor including an upstream strut, see Figure 5.3.
- BLI integrated system: body and propulsor, see Figure 5.4.
- WI integrated system: body and propulsor, see Figure 5.5.

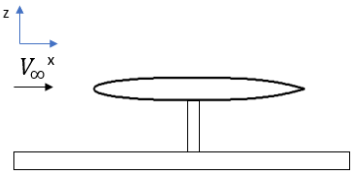

Figure 5.1: Isolated body configuration

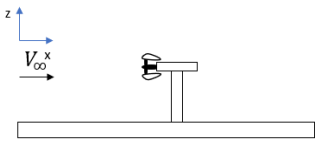

Figure 5.2: Isolated propulsor configuration

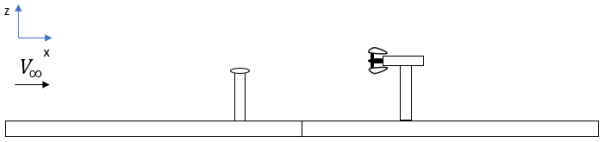

Figure 5.3: Isolated propulsor including an upstream strut

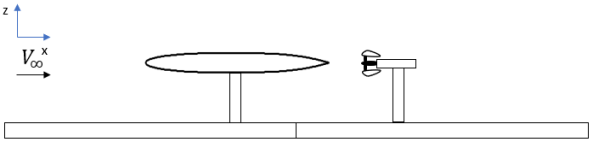

Figure 5.4: BLI configuration

Figure 5.5: WI configuration

The first test is to measure the drag of the isolated body at the "cruise" or unaccelerated condition (at Mach = 0.176) as shown in Figure 5.1. The drag can be measured using the internal load cell of the body. The subsequent step is to measure the body wake size. The body wake is measured with the five-hole probe by directly measuring behind the body in a cross-shape, as shown in Figure 5.6. The reason of measuring a cross is to find whether the body wake is axisymmetric, since PIV measurements were not possible.

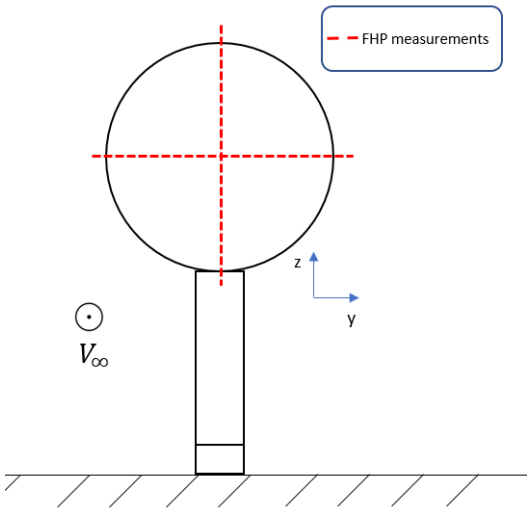

Figure 5.6: Five-hole probe measurements at the back of the body to measure the wake size and check axisymmetry (view looking upstream)

Another important measurement is to determine the position where the static pressure recovers in the body wake. For this purpose the wake is measured using a five-hole probe and the body is moved upstream using the rail system. Figure 5.7 shows a schematic of the pressure measurements behind the body.

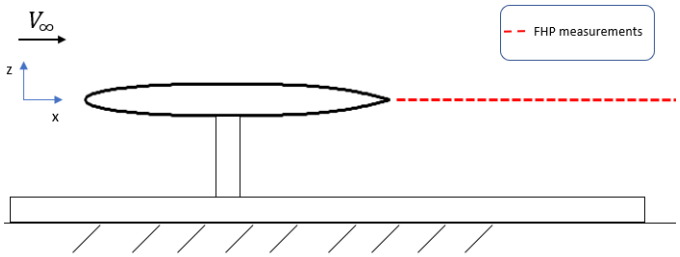

Figure 5.7: Measurements of the static pressure behind the body using a five-hole probe

Then, the drag of the body at M=0.176 is used as an input for the required thrust of the isolated propulsor in order to simulate a non-BLI configuration, as shown in Figure 5.2. The thrust of the propulsor is measured using a load cell. The power required given the required thrust for this configuration is used as a reference for the Power Savings Coefficient. In order to obtain the mechanical flow power, jet dissipation and propulsive efficiency five-hole probe measurements are carried at the control surface of the propulsor. Instead of measuring the whole control surface, the analysis is simplified using the assumption of axisymmetry. Therefore, on a line around the control surface is measured as depicted in Figure 5.8. The detailed measurement path of the five-hole probe around the ducted fan is depicted in Figure 5.26.Moreover, in order to further check the symmetry of the measurements, the same five-hole probe measurements are repeated in the opposite side. Also, at the inlet of the propulsor a cross-shape of five-hole probe measurements is completed in a similar manner as with the isolated body configuration (see Figure 5.6).

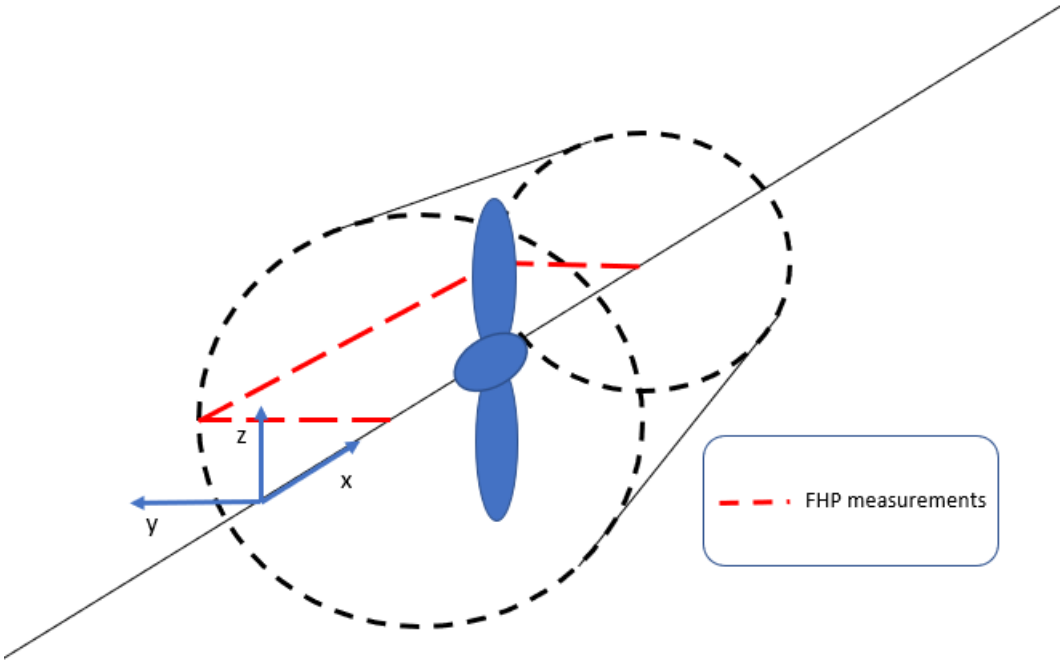

Figure 5.8: Control surface around propulsor. The five-hole probe measurements are only measured in a line around the control surface assuming axisymmetry

Subsequently, a strut is added in front of the propulsor in order to ensure that during the BLI or WI configurations the strut connected to the body does not influence the flow ingested by the propulsor, as depicted in Figure 5.3. If the influence of the strut is non-negligible then corrections should be applied in such cases. These corrections are interesting for wind tunnel providers such as DNW. Balance measurements and five-hole probe measurements are repeated in the same manner as with the isolated propulsor case.

The integrated systems are divided in two cases a BLI configuration and a WI configuration, see Figures 5.4 and 5.5. In the BLI configuration the propulsor is as close as possible to the body and in the WI configuration the propulsor is at a position where there is no more pressure interaction with the body. In these configurations, balance measurements are performed such that the thrust of the propulsor equals the drag of the body. The electric power required is measured at this condition, which then is used for computing the power savings. Then, five-hole probe measurements are carried around the control surface maintaining the unaccelerated condition, repeating the same procedure as for the isolated propulsor case. Then, the power savings coefficient can also be computed from the mechanical flow power and the propulsive efficiency as well.

2 Wind tunnel facility: Low-Speed Tunnel (LST)

The main objective of a wind tunnel is to simulate particular aspects of air flowing around an object or vehicle. Wind tunnel testing started in the late 19th Century and still is relevant today, even with the rise of Computational Fluid Dynamics (CFD). However, it is impossible to simulate all aspects of the aerodynamics of a vehicle simultaneously, typically the Reynolds number and/or Mach number are matched in order to investigate relevant effects. Wind tunnels can be categorized as open or closed circuit. An open wind tunnel accelerates the stagnant air from the environment and is exhausted out the back to the surroundings. These type of wind tunnels are inexpensive to build, but they are energetically inefficient since the air has to be continuously accelerated. Furthermore the quality of the flow is affected by any disturbances in the stagnant upstream flow. On the other hand, closed return wind tunnels let the flow circulate avoiding continuously accelerating the air, being more energy efficient than an open return wind tunnel. The air exhausted is returned to the front of the tunnel via a closed duct returning to the front of the wind tunnel, Figure 5.9 shows a schematic of a closed-circuit tunnel. This type of tunnel has larger construction costs, but can provide better flow quality overall. The tunnels can also be categorized depending on the flow regime subsonic ($M < 0.3$), transonic($M = 1$), supersonic($M > 1$) and hypersonic($M >> 1$).

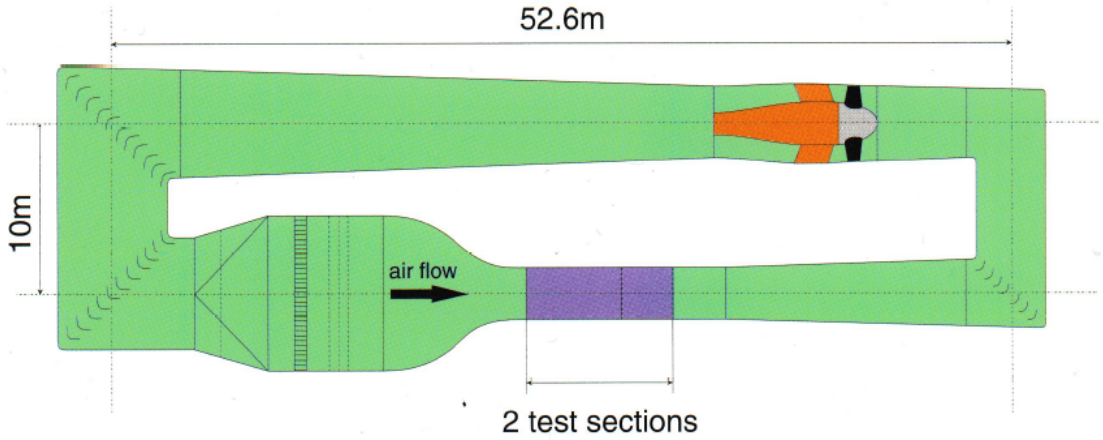

Figure 5.9: Schematic overview of the Low-Speed wind tunnel (LST-DNW)

The wind tunnel tests will be carried in the Low-Speed Tunnel (LST) operated by DNW, the German-Dutch Wind tunnels. DNW operates the wind tunnels of the German Aerospace Centre (DLR) and the Dutch National Aerospace Centre (NLR). The DNW-LST is located near Marknesse in the Netherlands where also the largest European low-speed wind tunnel is located. This is an industrial closed-type wind tunnel where tests are carried at atmospheric conditions and low-speed domain. The test section of this wind tunnel is 3.0 m x 2.25 m with turntables in top and bottom wall for 2D testing or 3.0 m x 2.25 m

with overhead balance for 3D testing. The operating range of this wind tunnel is from $0 \leq V_\infty \leq 80[m/s]$. The settling chamber has a honeycomb-type flow rectifier and three fine-mesh screens. After the settling chamber there is a 1:9 contraction ratio. The models can be supported with a six component balance or there is even sting support for internal balances. The wind tunnel is presented in Figure 5.10. The reference instrumentation consists of 4 total pressure tubes in each corner of the settling chamber including 4 temperature probes. In each corner of the contraction there are 4 static pressure tubes.
During the test campaign DNW's experienced wind tunnel operators and technicians worked on the construction of the set-up and testing. Since DNW-LST is a commercial industrial wind tunnel where clients test their models meant that there was limited testing time. This limited testing time played a role in the test campaign.

Figure 5.10: Aerial view of the DNW Low-Speed wind Tunnel (LST-DNW)

3 Wind tunnel model

The wind tunnel model is essentially divided in two different parts: a fuselage (or body) and a propulsor. The design of these two parts have certain design requirements that have to be met in order to have a functioning set-up. The process of designing the model is presented in Section 3.1. Then, a description of the isolated body is presented in Section 3.2, then the isolated propulsor in Section 3.3 and the isolated propulsor including the upstream strut in Section 3.4. Finally the integrated configurations (BLI and WI) are described in Section 3.5.

3.1 Model design

In this section a description of the design procedure and criteria of the model is explained. One of the goals of this research is to determine the power savings coefficient and propulsive efficiency, thus two different models or configurations are needed: a non-BLI configuration and a BLI configuration. The non-BLI configuration is used as a reference for comparison with the BLI configuration. In this manner the difference in performance between these two systems can be compared.
In literature there have been different ways of designing such systems e.g. the D8 "double bubble" has two different configurations a podded and an integrated system. These two models share the same physical components, except for the removable aft 20% of the fuselage but keeping the attached vertical tails and the horizontal tail. However, to design such a complete aircraft in the time frame of this thesis this is not possible. Therefore, a similar approach to Hartuç (2015) and Sabo and Drela (2015) was decided, where a body is in front of the propulsor and the propulsor's relative position can be changed.
Since the main goal is to investigate the effects of BLI, the body is designed keeping in mind that its boundary layer will be ingested by the propulsor. The analysis can be simplified if an axi-symmetrical body is chosen since it would produce an axi-symmetrical wake. Once the body geometry is determined its drag and wake diameter can be estimated. The body drag and wake diameter are used as inputs for the design of the propulsor. The ideal case of a wake-filling propulsor was presented by L. H. Smith (1993), where the propulsor diameter is the same size as the body wake diameter. Therefore, following the

ideal case, the propulsor size is determined by the body wake in order to have the highest power savings. However, the propulsor should also be able to produce a thrust equivalent to the body drag to simulate cruise condition, a zero net streamwise force. The motor and power supply have to be chosen according to the thrust required and size of the propulsor. Special attention is given to the RPM, torque, voltage and current required. The diagram in Figure 5.11 shows schematically the iterative steps taken when designing the model. The wind tunnel model, body and propulsor, has been constructed and designed by DNW.

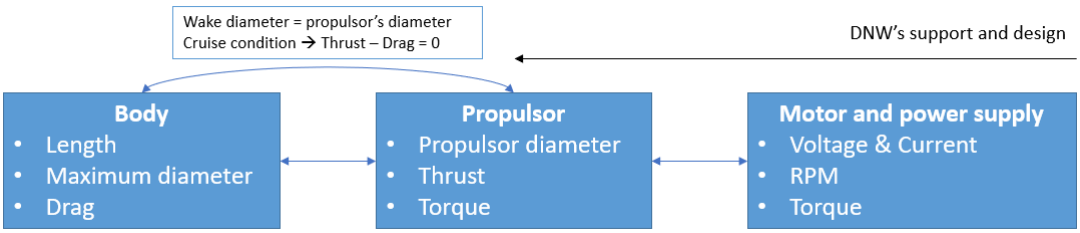

Figure 5.11: Design diagram

Different bodies were compared in terms of their size, drag and wake diameter for several Mach numbers. The bodies compared are all axi-symmetric in order to simplify the problem. The body used in the LST wind tunnel resembles an aircraft fuselage and is positioned over a strut. The fuselage is an axi-symmetrical body with a total length $L = 1.5m$ and a maximum diameter $d_{max} = 0.23m$. The characteristics of the body can be found in Table 5.2. The body is divided in three parts: a forebody, a midbody and an afterbody. The coordinates for these parts are given from the model nose:
The forebody is defined as a modified ellipsoid:

$$z = 0.125\sqrt{1 - [\frac{0.55 - x}{0.55}]^2} \qquad 0 \leq x \leq 0.55[m] \tag{5.1}$$

The midbody remains cylindrical:

$$z = 0.125 \qquad 0.55 \leq x \leq 0.75[m] \tag{5.2}$$

Finally the afterbody is an ogive shape tail:

$$z = 0.125[1 - [\frac{0.75 - x}{0.75}]^3] \qquad 0.75 \leq x \leq 1.5[m] \tag{5.3}$$

The strut and body connection was designed and manufactured by DNW. Figure 5.12 shows the designed body including the strut in a software developed by Dassault systemes named computer-aided three-dimensional interactive application (CATIA). Figure 5.13 shows the structure inside of the model. The load cell is depicted as a green rectangle and measures the difference between the metric and non-metric world. This means that the balance measures the body drag directly with no influence from the strut drag. The yellow metal thread connects the leading edge and trailing edge of the body and can be tightened compressing all body parts and keeping them together.

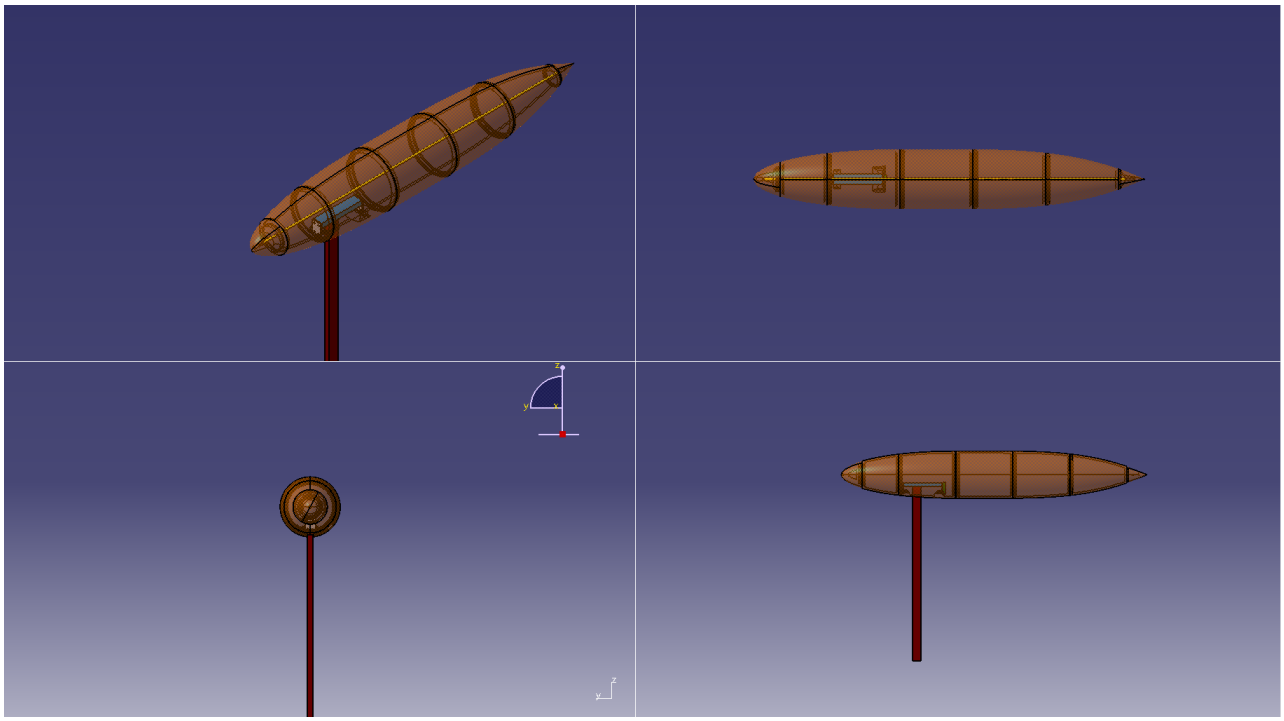

Figure 5.12: Final design of fuselage and strut using CATIA

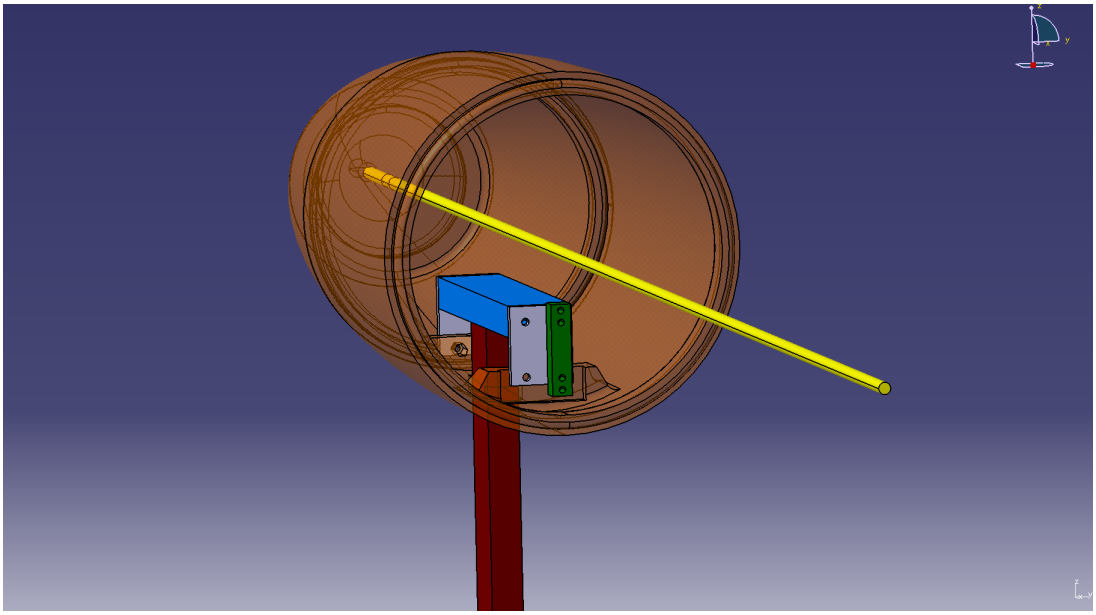

Figure 5.13: Interface between body, strut and load cell

The drag of the body is computed using the method given in the report ESDU 78019 (ESDU, 1978). In this report the profile drag is given for axi-symmetrical bodies at zero incidence at sub-critical Mach numbers with complete subsonic flow. In order to apply this method certain parameters have to be defined:

- Maximum diameter of the body (D_{max})
- Total length of the body (L)
- Length of the forebody (l_f)
- Volume coefficient of the forebody (C_{V_f})

- Total volume coefficient (C_V)
- Total surface coefficient (C_S)
- Transition point (X_{tr})
- Reynolds number (Re)
- Mach number (M)

The geometrical characteristics of the body can be found in the report ESDU 77028 (ESDU, 1977). The range of bodies that can be tested with this method for which it provides a good agreement with experimental and theoretical data is summarized in Table 5.1. The estimated drag of the body is 6.5 $[N]$ with a wake diameter of $d_{wake} = 0.131$ $[m]$

Table 5.1: Input ranges for which good results can be expected

l_f/L	ρ_0	C_{Vf}	l_m/L	l_a/L	A	C_{Va}	C_V	C_S
0.1 to 0.5	0 to infty	0.56 to 0.86	0 to 0.6	0.25 to 0.6	0 to 2	0.37 to 0.71	0.50 to 0.85	0.63 to 0.93

The boundary layer grows along the axi-symmetrical body upon reaching the pointed end of the body. The boundary layer then concentrates into a circle with an approximate diameter d_{wake}: (Sighard F. Hoerner, 1958)

$$d_{wake} = \sqrt{3\delta_0 d_{max}} \tag{5.4}$$

Where d_{max} is the maximum diameter of the body and δ_0 is the basic boundary layer thickness. The total boundary layer thickness in a turbulent flow is given by the following equation:

$$\delta_0 = \frac{0.154x}{R_x^{1/7}} \tag{5.5}$$

where x is the length in meters of the body and R_x is the Reynolds number $R_x = \frac{vx}{\nu}$.

Table 5.2: General characteristics of the body under consideration

L [m]	d_{max} [m]	l_a[m]	l_f [m]	l_m [m]	C_{Vf}	C_V	C_S	X_{tr} [m]	Flow vel. [m/s]	Drag [N]	Re	d_{wake} [m]	M
1.5	0.23	0.55	0.75	0.2	0.6535	0.6939	0.805	0.2	60	6.5	6.12E+06	0.131	0.176

Another point of interest is minimizing the body-strut interaction. This interaction is minimized when the strut is placed where there is *zero pressure gradient*.(L.L.M. Veldhuis, 1988). The pressure distribution for the forebody and afterbody can be obtained from (ESDU, 1982) as shown in Figure 5.14. From this figure one can observe that for the lowest Mach number 0.4, the pressure gradient quickly becomes zero. For lower Mach numbers it is assumed that even a flatter pressure distribution is obtained. The position of the strut is decided to be set at one fourth of the total length from the body nose $0.25L = 0.375$ $[m]$.

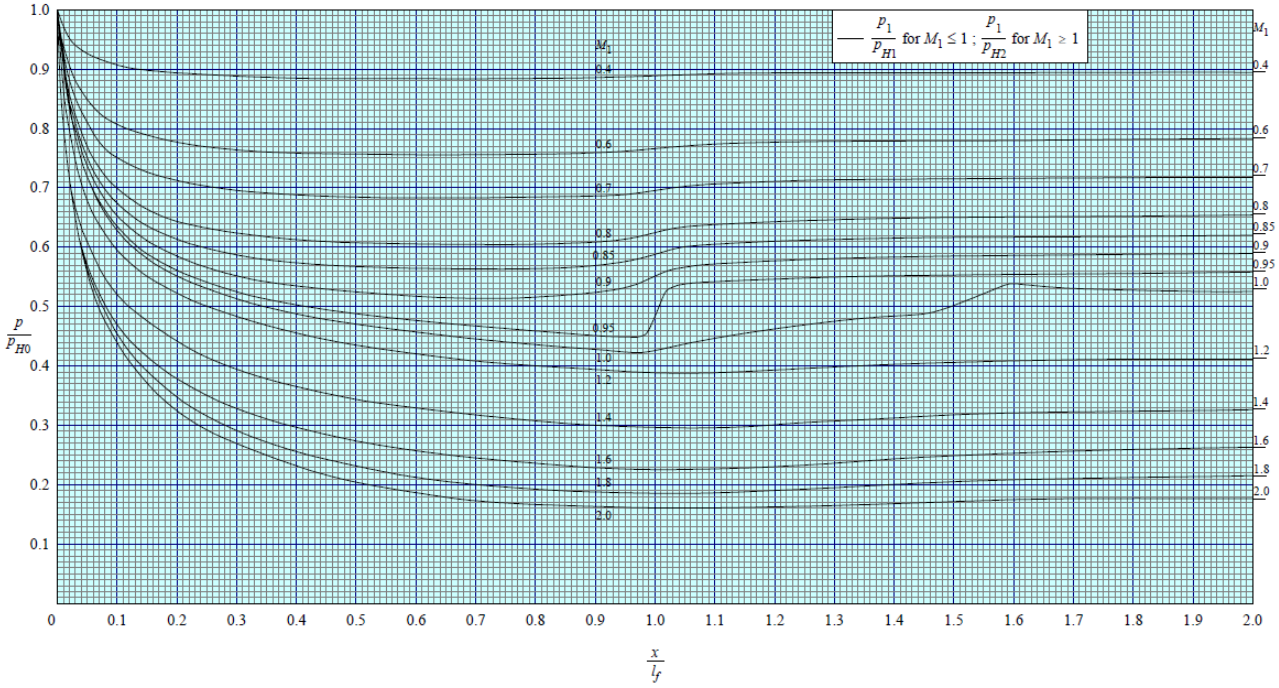

Figure 5.14: Pressure distribution of the forebody for a $\frac{l_f}{D} = 2$ (ESDU, 1982)

On a different note, the propulsor design was dependent on the wake diameter and body drag. The estimated body wake diameter is used for choosing the size of the propeller blades and the estimated body drag is used as a reference for the required thrust. In this research due to time constraints it is not possible to fully design a propulsor, thus commercially available parts are purchased. The propulsor (elements) are bought directly from a store. These commercially available propellers are not designed for BLI or WI conditions, therefore their performance cannot be predicted.
The first step in the design process is to decide what size and type of propeller blades are chosen. Propeller blades manufacturers usually only provide the thrust for static conditions, meaning that the thrust at the unaccelerated condition $M = 0.176$ is unknown. As a result several propeller blades around the size of the body wake were ordered, including a ducted fan. There are benefits and disadvantages when using an open rotor or a ducted fan. An open rotor is less expensive, they come in variable sizes but have large tip losses. On the other hand a ducted fan has less tip losses, produces less noise and produces high thrust. However, the size of the ducted fans commercially available is limited and the ducted fan can stall for off-design conditions. Furthermore, the lip or casing of a ducted fan can be considered as a lifting surface. When lifting surfaces are in a wind tunnel, corrections for the flow parameters and coefficients are necessary (Ewald, 1998). Due to the tight schedule, it was decided to proceed with only testing the ducted fan because it can certainly provide the required thrust even at $M = 0.176$.
The second step in the design process is deciding a suitable electric motor compatible with the propeller blades. The electric motor has to handle the required RPM and torque derived from the required thrust. There are several commercially available electric motors from companies such as Maxon motors, Hacker motors etc. The required torque can be retrieved from the performance data sheets of the propeller. To investigate the effects of boundary layer ingestion, pressure scans and PIV at the inlet and outlet planes of the propulsor are necessary. During the design process it was considered to have a long shaft between the motor casing and the fan itself in order to provide good optical access for PIV and for pressure measurements. Ultimately, due to the high RPM and torque requirements it was not possible to include such a shaft.
The motor has to be connected to a compatible electronic speed controller (ESC). This controller is an electronic circuit that controls and regulates the speed of the electric motor. The next step in the design process is the casing around the motor, ESC and load cell. DNW specially designed a casing for the motor, ESC and fan. Figure 5.15 shows the designed casing for the propulsor. One can observe that the green coloured casing has cooling ribs designed for cooling down the motor. The ESC is located at the end of the casing in the jet of the propulsor. It is necessary for the ESC to have cooling which is provided

by the jet coming from the the propulsor. The fully built model is shown in Figure 5.18. The load cell, indicated as a blue rectangle is connecting the casing of the propulsor with the strut. This means that the load cell will measure thrust of the propulsor, excluding the strut drag but including the drag of the casing. This is disadvantageous since the net thrust is preferred to be measured rather than the gross thrust.

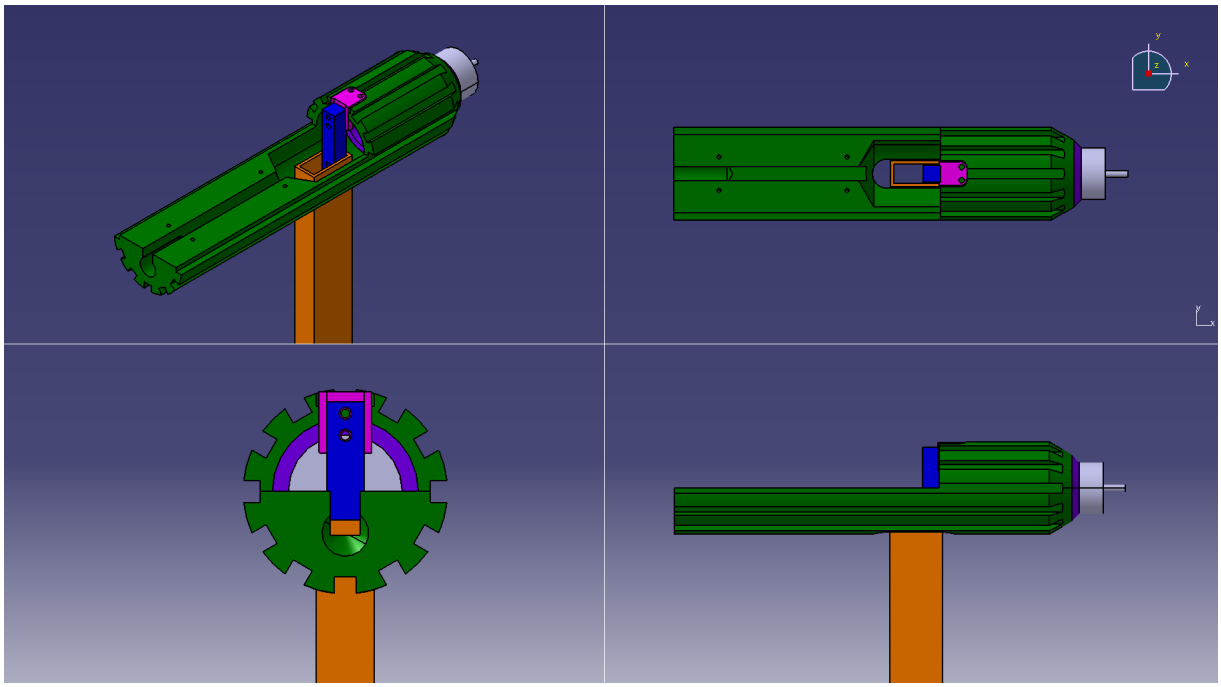

Figure 5.15: Housing of the propulsor including strut

3.2 Isolated body

In this section the final design of the fuselage is presented. The fuselage or body consists of several parts. The parts of the body were printed using a 3D printer (Ultimaker 3 and 5), Figure 5.16 shows the side perspective of the body mounted on its strut. The material used for 3D printing is polylactic acid (PLA). These parts were assembled by DNW and special attention was given to the connections between parts. The permissible limit of variation, or tolerances, for the 3D printing parts made it difficult to fit them together. Therefore sanding was required at the connection points between parts. The 3D printed surface of the body is rough, therefore transition from a laminar boundary layer to a turbulent boundary layer is expected to occur, avoiding boundary layer separation. Moreover, there is no need for a zig-zag tape due to this high surface roughness.

Figure 5.16: Side view of body mounted on the strut and rails

The inside of the body is visible in Figure 5.17, where the load cell, its cabling and the strut can be observed. During the assembly it is important to correctly align the body with the tunnel before calibrating the load cell. The alignment was carried using a laser alignment tool. Furthermore, it can be observed that there is a clear separation between the body strut and the body itself making the division between the metric and non-metric parts. The load cell calibration is shown in Appendix B.

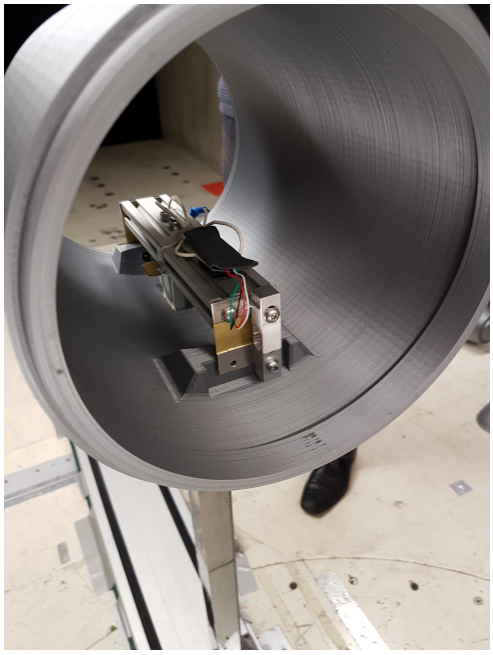

Figure 5.17: Inner structure of the fuselage

3.3 Isolated propulsor

The final design of the propulsor is presented in this section. The propulsor was constructed and designed by DNW. Because of the time constraints, it was decided to order commercially available parts instead of fully designing and manufacturing the propulsor. Figure 5.18 shows the ducted fan including the strut and casing. The main elements of the propulsor are:

- Stream-Fan 120/700
- Motor E50-M 3D
- ESC: MasterMezon 135 opto
- Casing and strut constructed and designed by DNW

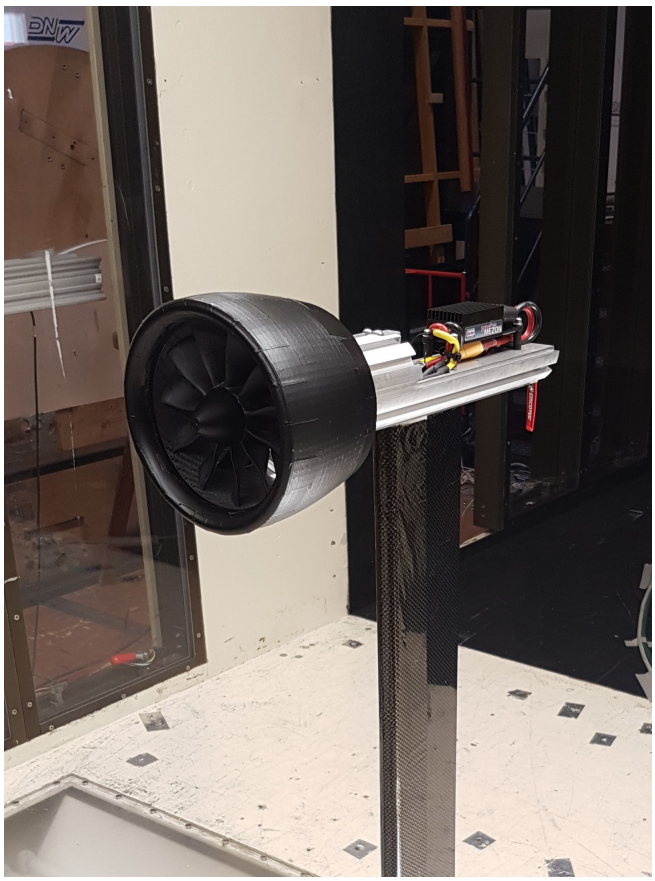

Figure 5.18: Electric ducted fan over the strut

The ducted fan is a Stream-Fan 120/700 from Hacker Motors. During the first tests with the ducted fan, large vibrations were observed when the tunnel velocity was above $40m/s$ at zero RPM. One of the possible causes for these vibrations was the inlet lip design. The inlet lip was assumed to be the cause of vortex shedding which in turn could cause the onset of mechanical vibrations over the whole system. Thus, the inlet lip was re-designed by enclosing the ducted fan. The final design with the additional designed cover is shown in Figure 5.19.

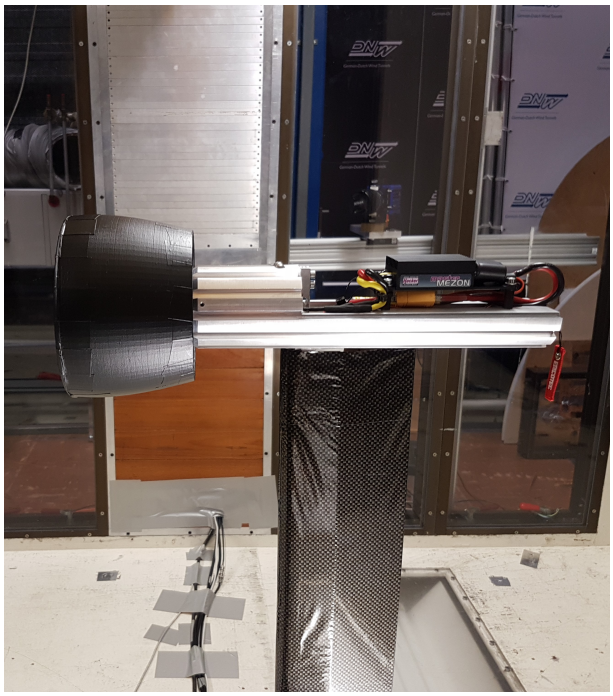

Figure 5.19: Side perspective of propulsor

The motor chosen is a E50-M 3D from Hacker motors shown in Figure 5.20a. This motor is capable of providing up to 41670RPM. The motor is connected to the electronic speed controller, the MasterMezon 135 opto presented in Figure 5.20b. An additional safety power switch is included at the back of the propulsor casing as shown in Figure 5.21b. If the safety switch is removed then the propulsor receives no power.
The load cell connecting the strut and the casing can be seen in Figure 5.21a. There is a small gap present between the motor casing and strut, separating the metric and non-metric part.

(a) Motor E50-M 3D (*Hacker Brushless motors*, 2019)

(b) MasterMezon 135 opto (*Hacker Brushless motors*, 2019)

Figure 5.20: Motor and high speed controller

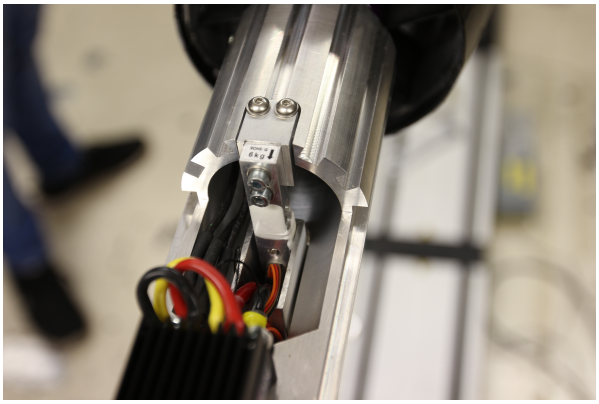

(a) View of the load cell and gap between the metric and non-metric world

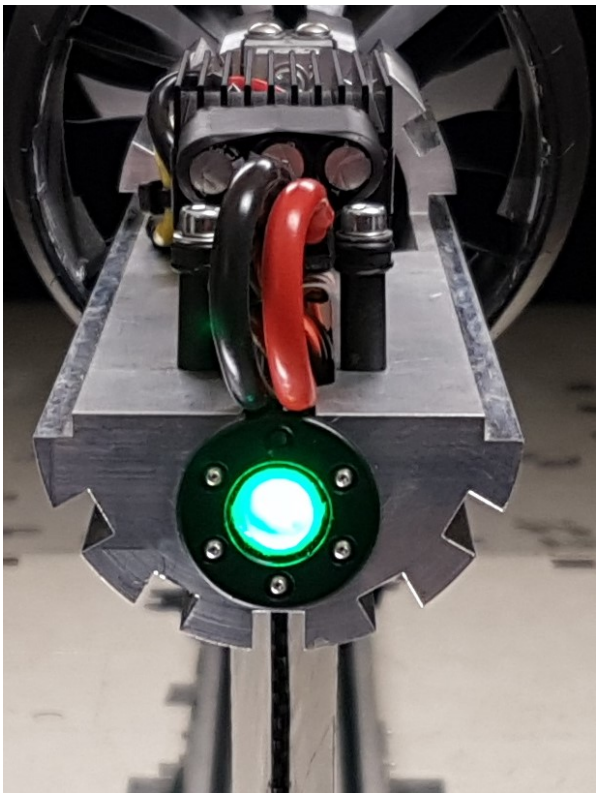

(b) Safety switch

Figure 5.21: Position of the load cell and safety switch on the propulsor

3.4 Isolated propulsor with upstream strut

The main goal of having the strut upstream, exactly at the position where it would be if the body is there, is to confirm whether corrections are needed to be applied due to the strut-wake interference. The same strut used with the fuselage is used in this case but an aerodynamically shaped hat is added on top of the strut. The propulsor with the upstream strut can be seen in Figure 5.22a, and a top view of the upstream strut can be seen in Figure 5.22b.

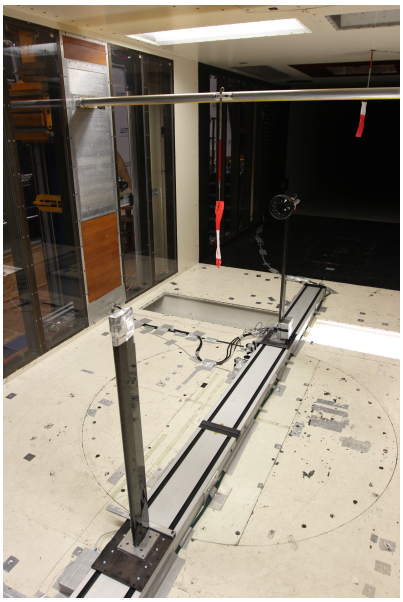

(a) Isolated propulsor with upstream strut

(b) Top view of the upstream strut

Figure 5.22: Isolated propulsor with upstream strut

3.5 BLI and WI configuration

The integrated configuration consisting of the body and propulsor, specifically the BLI configuration is depicted in Figure 5.23. The closest distance between the propulsor's hub and the trailing edge of the fuselage is of $7.8cm$, where the distance between the FHP's tip and the trailing edge is $1.5cm$ and the distance between the FHP's tip and the propulsor's hub is $6.3cm$ as represented in Figure 5.24. An extra measurement is also carried at relative distance of $10.8cm$, the distance between the trailing edge of the body and the five-hole probe was kept constant while the propulsor has moved back by $3cm$. One can also observe in Figure 5.23 the yellow wing which carries the five-hole probe in the back.

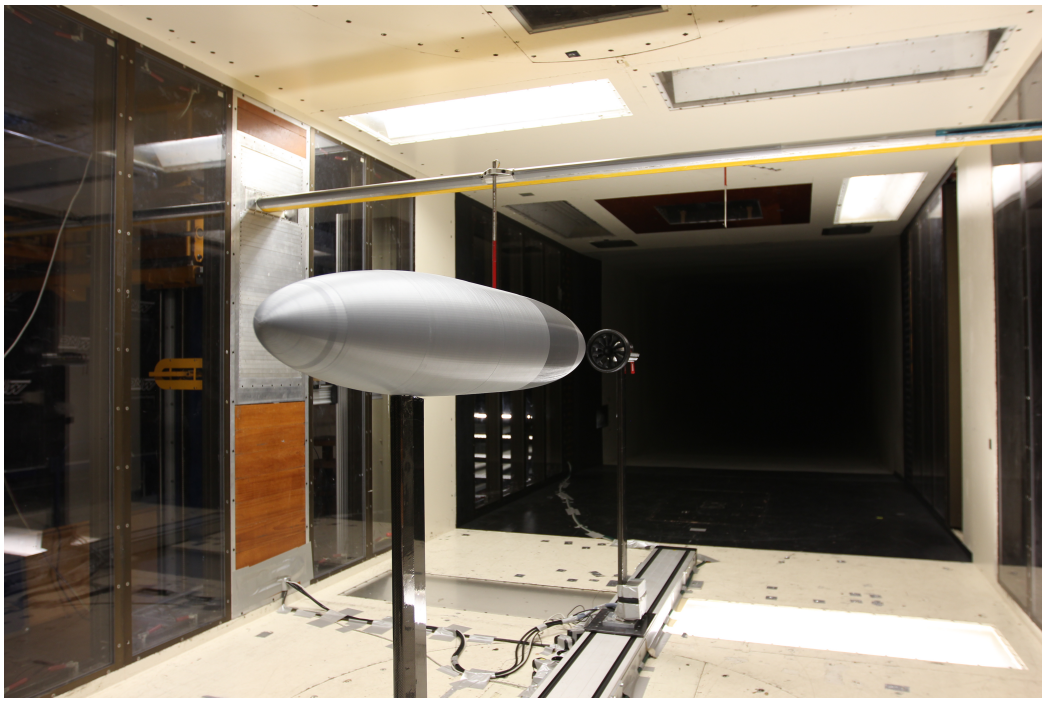

Figure 5.23: Integrated system: BLI configuration

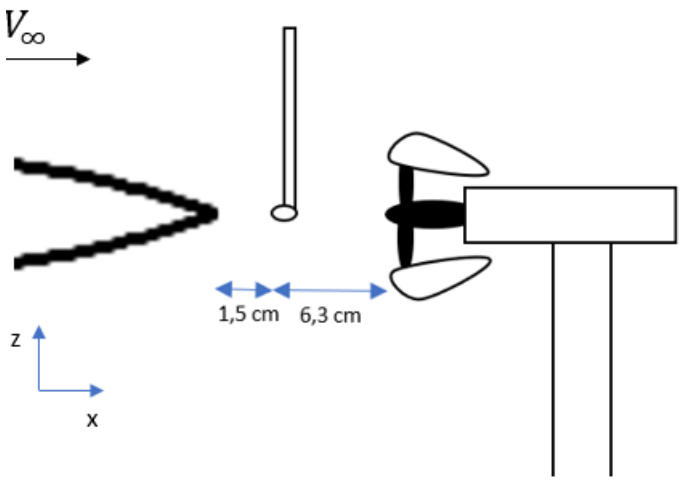

Figure 5.24: Distance between the trailing edge of the fuselage and the FHP (1.5 cm) and the distance between the FHP and the propulsor's hub (6.3 cm)

The WI position was found by measuring the static pressure behind the isolated body until it recovers. In this way, there is no pressure interaction between the body and the propulsor. The results of this experiment are explained in Chapter 6 Section 1, where the distance between the propulsor's hub and the trailing edge of the body is 0.60 m. The two different integrated configurations: BLI and WI can be seen in Figure 5.25a and 5.25b. The distance between the five-hole probe and propulsor's hub is kept constant through out the experiment.

(a) BLI configuration (b) WI configuration

Figure 5.25: BLI and WI configurations

4 Instrumentation and data processing

The instrumentation depends on the quantities to be measured in order to answer the research questions. The final quantities needed are the mechanical flow power P_K given in equation 3.1, the jet dissipation Φ_{jet} given in equation 4.7, which in turn makes it possible for computing the propulsive efficiency η_p given in equation 4.8 and lastly the Power Savings Coefficient equation 3.7. The necessary quantities measured are summarized in Table 5.3.

Table 5.3: Measured quantities

Quantities	Description	Instrument
p_{t_∞}	Free-stream total pressure	WT instruments
P_∞	Free-stream static pressure	WT instruments
V_∞	Free-stream velocity	WT instruments
ρ_∞	air density	WT instruments
T_∞	Free-stream temperature	WT instruments
T_{t_∞}	Free-stream total temperature	WT instruments
M_∞	Mach number	WT instruments
P_t	Total pressure at control surface	Five-hole Probe
P_s	Static pressure at control surface	Five-hole Probe
V	Flow velocity (including angles) at control surface	Five-hole Probe
T_{prop}	Thrust of the propeller	Load cell
D_{body}	Body drag	Load cell
RPM	Revolutions per minute of the propulsor	Jeti kontroler Master MEZON 135 OPTO MM-135-O
x_{FHP},y_{FHP}, z_{FHP}	Position of the five-hole probe	WT instruments
x_{body}	Position of the body	Rail system
$x_{propulsor}$	Position of the propulsor	Rail system
P_E	Electrical power input	Derived from eq.
J	Advance Ratio	Derived from eq.
ρ	Density at control surface	Derived from eq.
T	Temperature at control surface	Derived from eq.
M	Mach number at control surface	Derived from eq.
q_∞	Free-stream dynamic pressure	Derived from eq.

The total pressure and total temperatures are measured at the beginning of the contraction with four total pressure probes and four temperature probes at each corner. The static pressure is also measured with four static pressure probes are installed at the end of the contraction in each corner. The temperature is also measured before the flow straightener with two thermocouples in the center. The density of free-stream is computed using the ideal gas law and is corrected for humidity. The probe traverse wing that holds the five-hole probe is capable of measuring the position and is transmitted to the control room.
The control surface measured around the propulsor is depicted in Figure 5.26, where the top view of the propulsor is shown and the control surface is marked by a dotted line. At the control surface the quantities needed are the total/static pressures and the flow velocity including its angles. Therefore, a five-hole probe was used since it can provide all these quantities. Three different planes are defined: inlet, side and outlet planes presented in Figure 5.26. At the inlet of the propulsor two cases were measured one at a distance of 6.3 cm from the propulsor's hub and another one at 9.3 cm of the hub. Due to safety concerns it was not possible to get closer to the inlet of the propulsor. In addition, it was not possible to measure all the outlet plane up to the motor casing due to safety concerns. These missing points are then extrapolated. The problem of using a five-hole probe is the flow distortion it produces, also noticeable changes in load cell measurements are found when the five-hole probe moves around the control surface. Initially PIV measurements were also aimed to be performed since it is a non-intrusive method of studying the flow field, unfortunately, the laser did not work properly. In Appendix C a short description of the PIV set-up is shown. Again, only one line is measured around the control surface since the assumption is that the flow is axisymmetric.
The electric power (PE) is obtained by measuring the voltage and current using the Jeti controller Master Mezon 135 Opto located near the motor. A second analogue current measurement is done by measuring the voltage drop over the minus 52V line 75mm2 copper from the power supply to the Jeti controller. This second current measurement provides a more accurate measurement compared to the result from the Jeti controller. The Jeti controller rounded the current to the nearest integer, while in this second method 2 extra decimals are obtained. Furthermore, the temperature of the tunnel varied (more than 30 degrees Celsius) therefore temperature corrections are necessary in order to find the proper electric power. This is explained more in detail in Chapter 6 section 2.

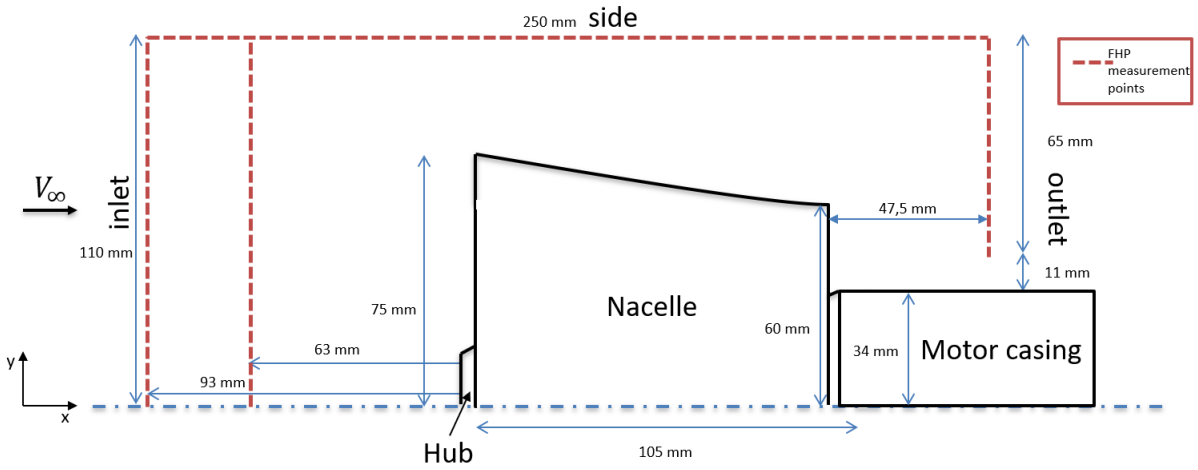

Figure 5.26: Top view of the ducted fan showing the points where the five-hole probe measures and three planes are defined: inlet, side and outlet planes. Note at the outlet plane it was not possible to measure up to the motor casing, the missing points are extrapolated

Without the inclusion of the PIV measurements, the processing of the data is fairly straight forward. DNW processed the core parameters with their own system applying corrections when deemed necessary. These parameters are then processed using MATLAB to obtain the power terms and propulsive efficiency.

Chapter 6

Results

The results are summarized in this chapter. Firstly, the results of the isolated body configuration are shown in section 1, then the results of the isolated propulsor (also including the upstream strut) are detailed in section 2. Lastly, the BLI and WI configuration results are presented in section 3.

1 Isolated body configuration

The first configuration tested during the test campaign is the isolated body, in order to obtain its drag at the chosen Mach number $M = 0.176$. Then, the drag at this condition is used as an input for the thrust of the isolated propulsor case.
First, the tunnel wind speed was increased from $0[m/s]$ up to $65[m/s]$ in steps of $5[m/s]$ and then decreased to zero in coarser steps. Figure 6.1a shows the drag coefficient against Reynolds number and 6.1b the drag against flow velocity. Carefully examining Figure 6.1b one can observe a quadratic behavior of the body drag against flow velocity. The theoretical definition of drag seen in Equation 6.1 confirms this behaviour, since the drag is proportional to the square of flow velocity.

$$D = \frac{1}{2}\rho V^2 S_{ref} C_D \tag{6.1}$$

Where ρ is the air density, V is the flow velocity, S_{ref} is the reference surface area and C_D is the drag coefficient. Figure 6.1a presents the drag coefficient against Reynolds number including the uncertainty of the measurements. At Reynolds numbers lower than $3.8 \cdot 10^6$ a difference can be seen in drag coefficient when the Reynolds number (or flow velocity) was increased or decreased. One of the possible reasons of such difference is the increase in uncertainty found at low Reynolds numbers. Furthermore, another cause of this difference in drag coefficient is due to a different transition location from laminar to turbulent flow. The transition location is influenced by several factors: Reynolds number, pressure gradient, sound, surface vibrations, surface heating/cooling, surface roughness etc. The boundary layer starts being laminar at low Reynolds numbers and with increasing Reynolds number this steady laminar flow becomes unstable. Then, unsteady Tollmien-Schlichting waves appear and grow inside of the boundary layer (Schlichting & Gersten, 2016). These waves break down into turbulence (transition) which leads to drastic changes in the boundary layer behaviour. It is worth to note that any type of instability could force the flow to become turbulent. There are methods such as transition strips which force the flow to become turbulent. The conditions are different for the case in which the starting point is a high Reynolds number and the flow is already turbulent. When decreasing the Reynolds number, the transition location from turbulent to laminar is different due to the flow already being turbulent and unstable. Therefore, a smaller Re is needed for the flow to become laminar again.

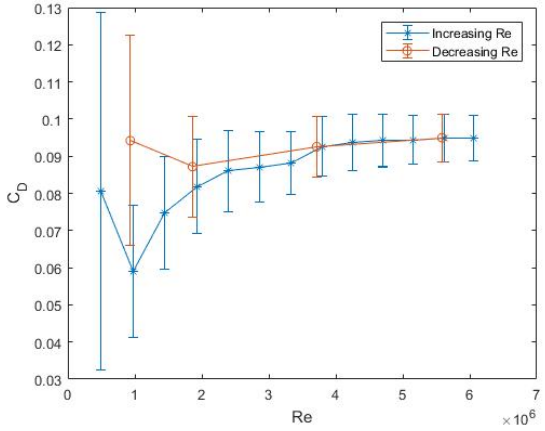

(a) Body drag coefficient against Reynolds number

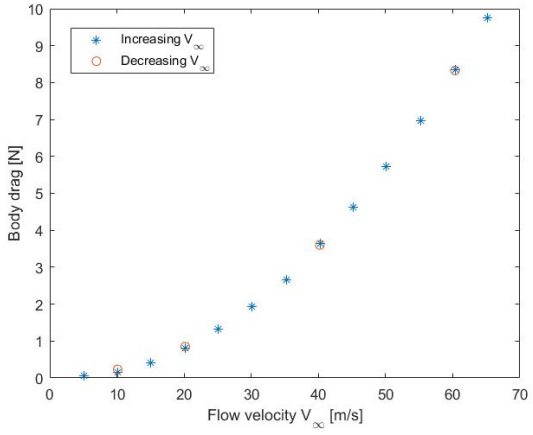

(b) Body load cell measurements showing the body drag against wind tunnel flow velocity

Figure 6.1: Isolated body configuration load cell results

The tunnel free-stream Mach number is set at a chosen condition $M = 0.176$ and the drag measured is $8.1[N]$. The results of the measurements and the general data of the fuselage are summarized in Table 6.1.

Table 6.1: Isolated body data

L [m]	Maximum diameter [m]	Mach number	Body drag [N]	Wake radius [m]
1.5	0.23	0.176	8.1	0.08

At the non-accelerated condition the body wake was measured with a five-hole probe. Two different measurements were performed:

1. Measurement of the body wake shape at a distance of 15 mm from the trailing edge. See Figures 6.2 and 6.3.
2. Measurement behind the trailing edge on how the wake develops and choose the position at which the static pressure recovers. See Figure 6.4a.

Figure 6.2 and 6.3 show that the flow velocities are smaller in the wake of the body that those at free-stream. The velocity in the wake can be represented as a Gaussian function. (Schlichting & Gersten, 2016) These losses in the velocities of the wake develop into a loss of momentum which is due to the drag of the fuselage. From Figure 6.2 the wake radius is approximately $0.08m$. This value seems to fall within the expect range of values, since the estimated wake radius is $0.065m$.
The axisymmetry of the flow can be investigated from Figure 6.3b where right, left, up and down are the directions where the five hole-probe were measured. The directions can be better understood from Figure 6.3a and Figure 5.6. From Figure 6.3b can be concluded that the largest difference can only be found when analyzing the "down" curve. This curve does not reach free-stream condition compared to the other directions due to the wake of the body's strut. The flow velocity used as a reference is the furthest away point measured from the center of the body with the five-hole probe.

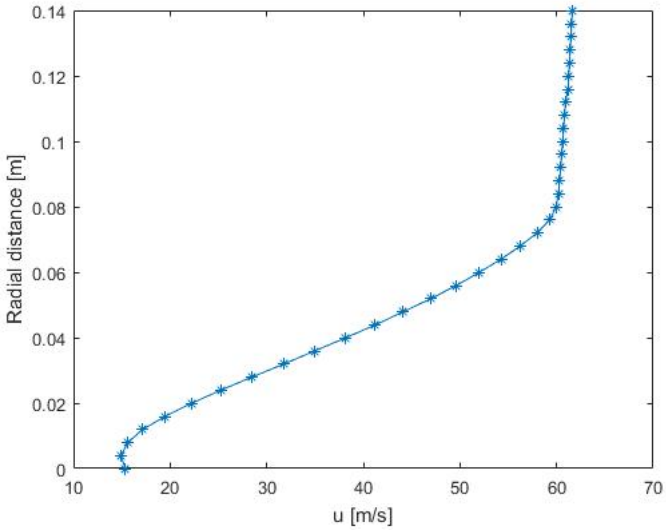

Figure 6.2: Wake flow velocity profile at the TE of the body at M=0.176

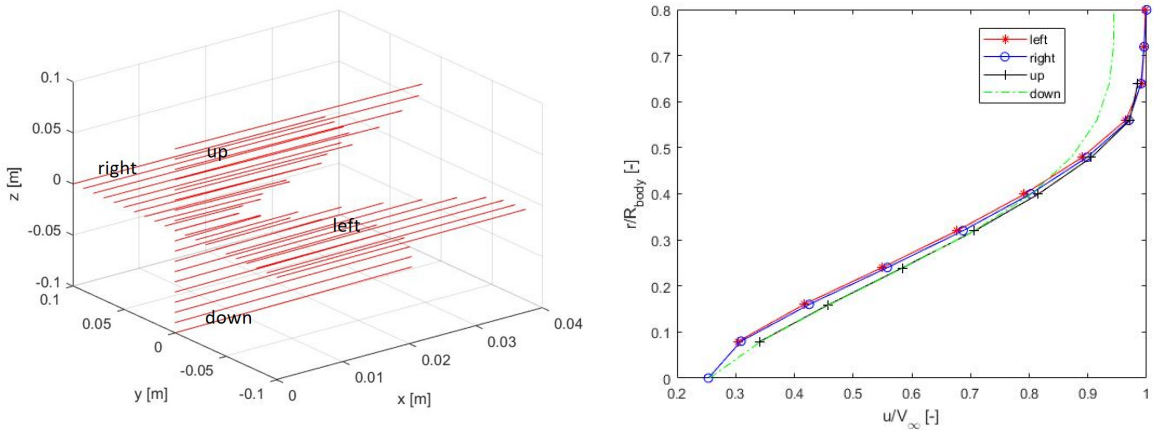

(a) 3-D representation of the velocity vector with four distinct directions

(b) "Down" velocity smaller at free-stream due to strut wake

Figure 6.3: Isolated body configuration: FHP measurements at the trailing edge of the body at M=0.176

The static pressure behind the body was measured using the five-hole probe, instead of moving the probe downstream, the body was moved upstream. The reason for this is that the probe traverse had limited range in the streamwise direction and it was possible to move the body using the rail system. Figure 6.4a shows the variation of static pressure against the body trailing edge position in tunnel coordinates, the body moves from $0.7m$ to $0.1m$ approximately. It can be observed that the pressure recovers to free-stream, thus defining the wake ingestion position, at a distance between the trailing edge and the five-hole probe of $0.6m$. This position is chosen such that there is no pressure field interference between the body and the propulsor. The spread of the wake increases with distance from the body and the differences between wake velocity and that of free-stream become smaller.
Furthermore, during these tests there were also balance measurements. Figure 6.4b shows the drag of the body decreasing when shifting the body upstream. In order to understand the cause of this difference in body drag several hypotheses were tested. Firstly, it was checked whether the body was misaligned when moving upstream. In the most upstream position the body alignment was checked using a laser alignment tool. The laser did not show any misalignment. A second hypothesis is a hysteresis effect on the load cell since the measurements were taken one after another. Therefore, load cell measurements were conducted starting from with the body at the most upstream position using the same weights used during the load cell calibration, showing the correct measurement. Moreover, the measurements were

repeated but similar results are found.

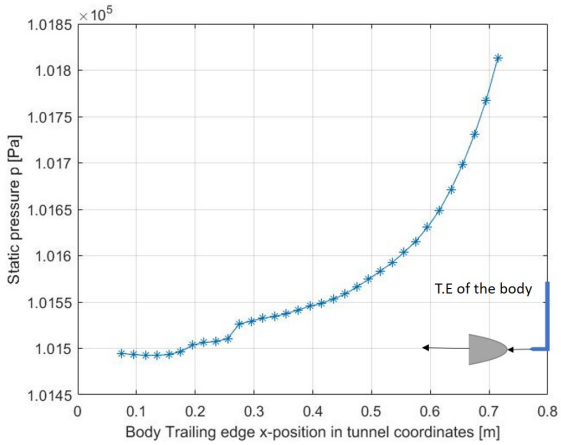

(a) Static pressure recovery behind the trailing edge (T.E) of the body measured with a five-hole probe

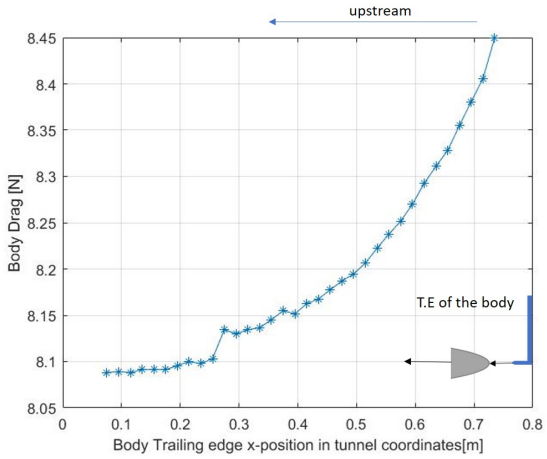

(b) Load cell measurement results: body drag variation due to the body moving upstream

Figure 6.4: Measurement of the static pressure behind the isolated body by translating the body upstream (starting from 0.7 m moving to 0.1 m), while the five-hole probe stays in the same position. Reduction in body drag is observed when translating the body upstream.

If the pressure and drag are non-dimensionalized into the pressure and drag coefficient, the results are shown in Figure 6.5a and 6.5b. The drag coefficient is supposed to be constant but a decrease in drag coefficient is seen in Figure 6.5b. The observable jump in drag coefficient is due to stopping the wind tunnel and re-starting it again. This jump is not observed when repeating the measurements as depicted in Figure 6.6. Therefore, the act of re-starting the wind tunnel did affect on the load cell measurements. The load cell readings could be influenced by the past measurements, having a hysteresis effect.
Furthermore the pressure coefficient does not recover to free-stream values. In an empty tunnel at $M = 0.176$, the five-hole probe measures a different static pressure compared to the free-stream case $P - P_\infty = 82[Pa]$. If this difference is added as a correction, Figure 6.5a shows that the pressure coefficient closely falls around 0, thus recovering to free-stream condition.

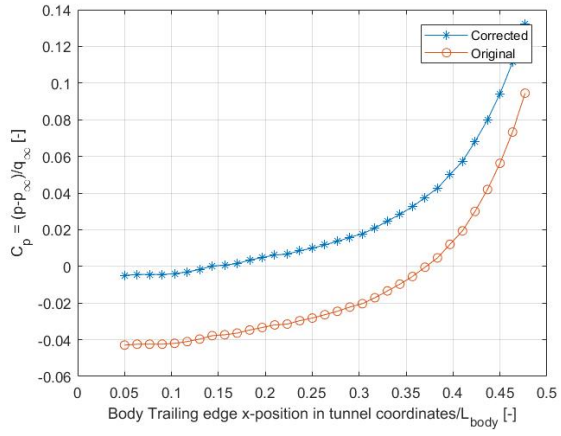

(a) Pressure coefficient recovery behind the T.E. of the body. Correction to the pressure measured by the five-hole probe is required

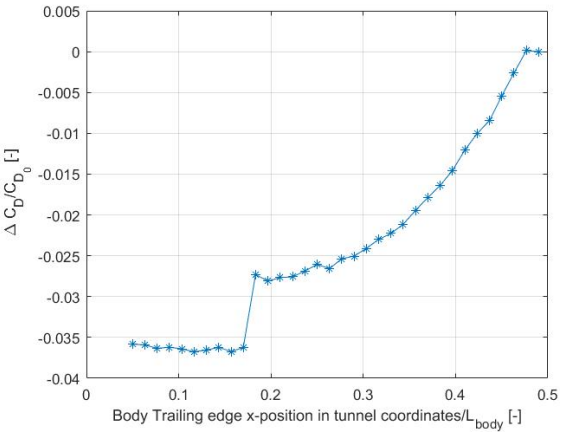

(b) Drag coefficient variation due to load cell measurements fluctuation when body is translating upstream

Figure 6.5: Five-hole probe measurements behind the fuselage

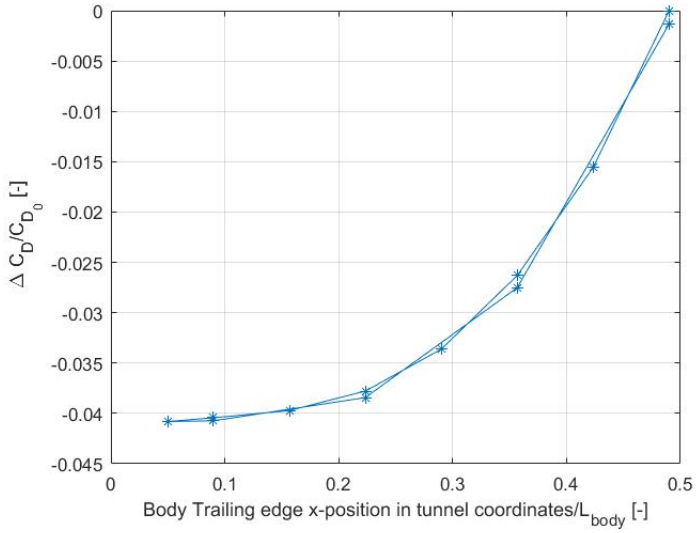

Figure 6.6: Extra run: Repeated balance measurements of the isolated body when translating upstream and downstream

Another possible explanation for the change in load cell measurements is the pressure gradient inside the test section shown in Figure 6.7. The trailing edge of the body was initially positioned around $x_{tunnel} = 0.8[m]$ and it was shifted almost $0.7[m]$ upstream to $x_{tunnel} = 0.1[m]$. The leading edge of the body reaches $x_{tunnel} = -1.4[m]$ in the most upstream position. In the top side of the figure one can observe the body position for both the most upstream position and downstream position. Shifting the body upstream means that there is a propulsive effect acting on the fuselage (the pressure on the trailing edge is higher than on the leading edge). If the pressure gradient is varying over the position, this effect influences the load cell measurements. Since the exact pressure data was not available no corrections to the measured data have been applied.

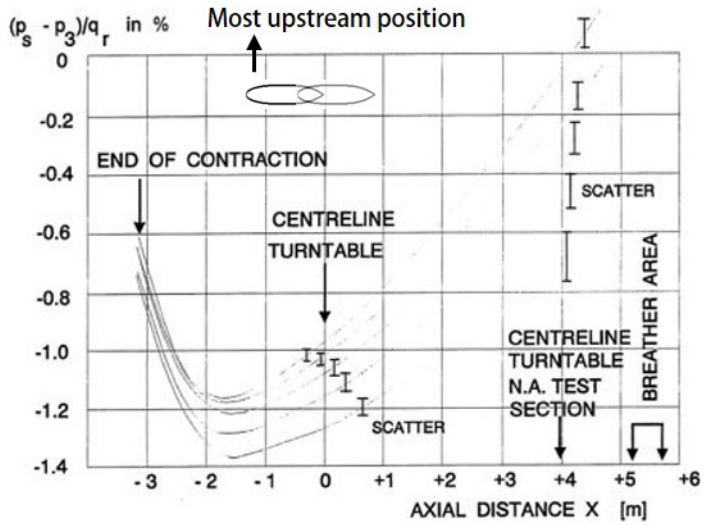

Figure 6.7: Axial static pressure variation along the streamwise direction in the wind tunnel test section (*DNW internal report*, n.d.)

An unlikely explanation for this behaviour is the interaction between the five-hole probe, the traverse wing and the body. When the drag of the isolated body without any influence of the five-hole probe is measured the drag found is $8.1[N]$. For the experiment where the body moves upstream, the drag of the body returns to $8.1[N]$ when it is at its most upstream position. This could be due to the diminishing interaction. The influence of the five-hole probe with the balance readings can also be seen for the other

configurations. The results for these are shown in the following sections. However, from a physical perspective when the five-hole probe is directly behind the body, the static pressure behind the body should increase, thus leading to a decrease in drag.

2 Isolated propulsor

The first test with the isolated propulsor is the balance measurements for a range of RPM and flow velocities. The flow velocities tested were 0, 20, 40 and $60m/s$. At each flow velocity the RPM was increased and then decreased up to a high enough thrust measured. Since the drag of the body is $8.1N$ at the unaccelerated condition and at $M = 0.176$ it was not necessary to obtain thrusts higher than $20N$. The reason for these tests is to understand the capabilities of the propulsor, since the capabilities at different flow velocities were unknown (only the static performance is known from the manufacturer). Figure 6.8a shows the balance readings (thrust of the propulsor) against RPM for different flow velocities. When testing at $40[m/s]$ or higher flow speeds the propulsor would start shaking, probably due to the vortex shedding of the casing. Therefore as a safety precaution the propulsor would be set at a high RPM before turning on the wind tunnel. That is the reason why in Figure 6.8a at $60m/s$ measurements with low RPM are not observed. The thrust can also be non-dimensionalized as the thrust coefficient, defined in equation 6.2:

$$C_T = \frac{T_{prop}}{\frac{1}{2}\rho_\infty V_\infty^2 S_{ref}} \tag{6.2}$$

Where T_{prop} is the propulsor's thrust, ρ_∞ is the free-stream air density, V_∞ is the free-stream flow velocity and S_{ref} is the model's reference area. Another important parameter is the advance ratio J defined as:

$$J = \frac{V_\infty}{nD_{prop}} \tag{6.3}$$

Where n is defined as the revolutions per second and D_{prop} as the propulsor's diameter. The thrust coefficient can then be plotted against the advance ratio as depicted in Figure 6.8b. One can observe that the propulsor's thrust coefficient (C_T) decreases with increasing advance ratio and the differences between the flow velocities are relatively small.

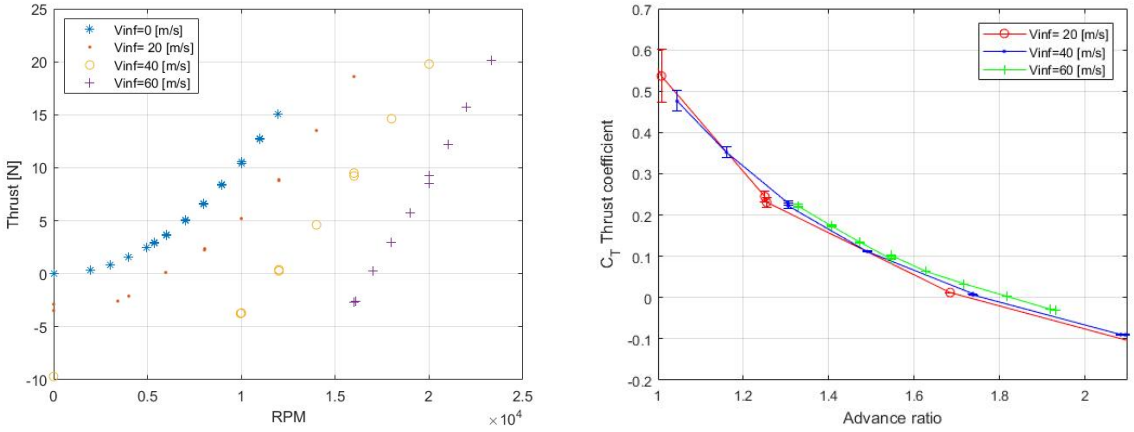

(a) Propulsor's thrust measured with a load cell varying against RPM for different flow velocities

(b) Propulsor's thrust coefficient (C_T) variation against advance ratio (J)

Figure 6.8: Variation of thrust and thrust coefficient for the isolated propulsor configuration

The electric power P_E measured for the isolated propulsor configuration for a varying range of RPM is depicted in Figures 6.9a and 6.9b. In these figures one can observe the increase of electric power with increasing RPM. During the test campaign the temperature of the tunnel varied significantly, from 20 degrees up to 50 degrees. The resistance of the cabling is temperature dependent, thus with these large variations of temperature the electric power measured has to be corrected. The electric power can be

corrected by correcting first the current measured. The conductors resistance R can be corrected using the following relation:

$$R = R_{ref}(1 + \alpha(T - T_{ref})) \tag{6.4}$$

Where $R_{ref} = 4\Omega$ is the reference resistance of copper at 20 degrees Celsius, α is the temperature coefficient of resistivity at 20 degrees (for copper $\alpha = 0.0039[1/K]$) and T_{ref} is the reference temperature $T_{ref} = 298.158K$.
This correction is applied to the power measured, the differences between the corrected and uncorrected electrical power can be observed in Figure 6.9a. When corrected, less power is measured for the same RPM. Furthermore the electric power can be non-dimensionalized (see equation 3.3) and can be plotted against the advance ratio as shown in Figure 6.10. Since the electrical power coefficient is inversely dependent on the cube of the flow velocity (see equation 3.3) and the advance ratio depends on the flow velocity, the electric power coefficient decreases with increasing advance ratio. Furthermore, it can be observed that at $V_\infty = 20\frac{m}{s}$ the power coefficient is higher than at the other two flow velocities. The most probable cause for this difference is that the input electric power to the propulsor is measured instead of the shaft power. The conversion of electric power to shaft power can be inefficient at low flow speeds, thus there may be a certain threshold that has to be overcome for it to deliver the same shaft power. The input electric power does not interact with the flow, on the other hand the thrust is dependent on the flow conditions thus in Figure 6.8b no difference is observed at $V_\infty = 20\frac{m}{s}$.

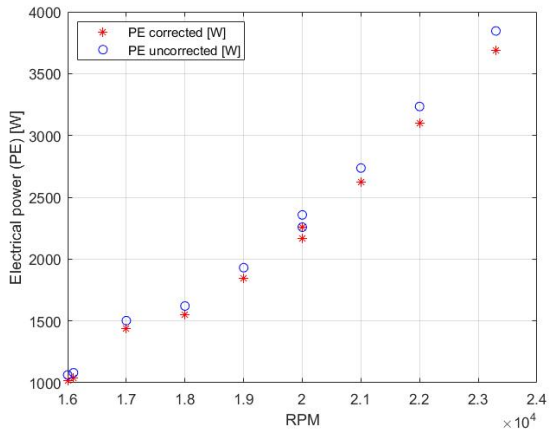

(a) The electrical power measured has to be corrected due to large fluctuations of temperature in the test section. The power presented is at $M = 0.176$

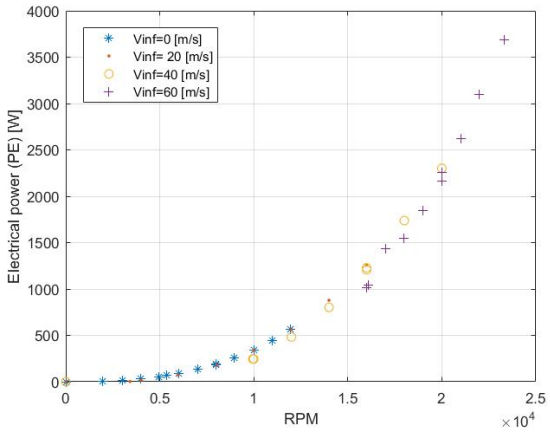

(b) Electrical power for different wind tunnel flow velocities

Figure 6.9: Electrical power measured against RPM for the isolated propulsor configuration

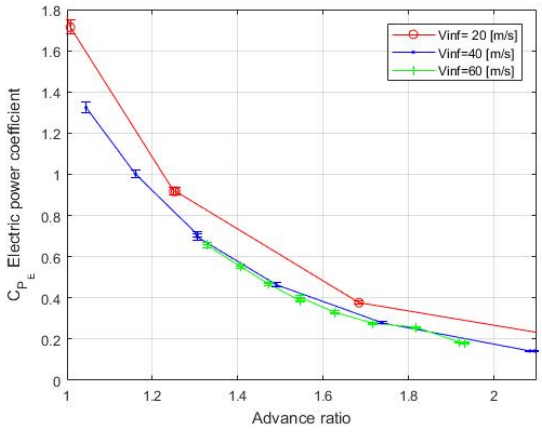

Figure 6.10: Electric power coefficient variation against the advance ratio for the isolated propulsor configuration

Five-hole probe measurements

The FHP measurements were carried at the unaccelerated condition and at $M = 0.176$. Before starting the measurements of the FHP around the control surface, the thrust of the propulsor is set to $8.1[N]$ with the FHP positioned far away from the configuration in order to avoid any interference from the FHP with the flow. Once the thrust is set to $8.1N$ the FHP measurements begin. Figure 6.11 shows the flow velocity vectors measured at the inlet, side and outlet planes defined in Chapter 5 section 4 in Figure 5.26. At the inlet of the propulsor the flow velocity is close to the free-stream values since the propulsor is ingesting free-stream velocity. At the side plane, the flow velocity vector is influenced by the nacelle of the propulsor thus causing the flow to gain an angle. At the outlet plane, the flow velocity remains close to free-stream outside of the jet of the propulsor where the flow velocity increases. In addition, the wake of the nacelle can be observed around $y = 0.07m$.

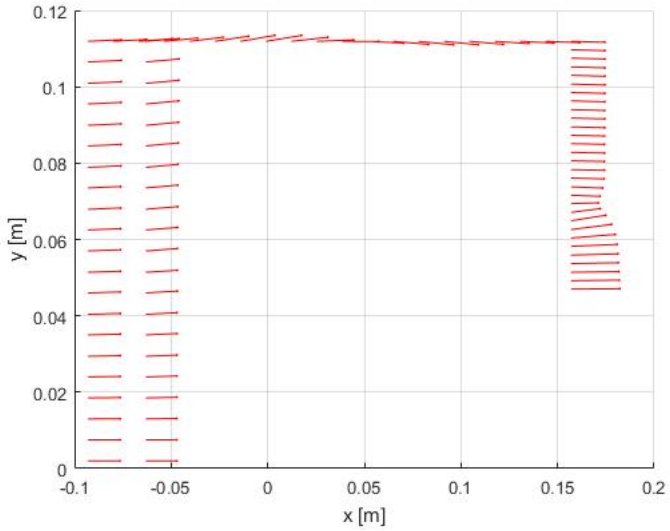

Figure 6.11: Flow velocity measured around the propulsor with the FHP. On the left hand side uniform flow is observed. On the right hand side the jet flow velocity is observed for $y \leq 0.06$ [m]

The axial flow velocity at the inlet, side and outlet planes are depicted in Figures 6.12a, 6.12b and 6.13a. The propulsor radius $R_{prop} = 0.06[m]$ is used as a reference in order to non-dimensionalize the distance for the inlet and outlet planes. For the side plane (Figure 6.12b) the distance is non-dimensionalized by the total length the FHP translates in the streamwise direction: $|X| = 250mm$ (see Figure 5.26). At the

inlet the flow velocity is lower near the hub and larger further away from the hub. The reason for this is that the hub itself stagnates the flow in front of it. On the other hand at the side plane there is a slight variation of axial flow velocity due to the fan casing flow blockage.

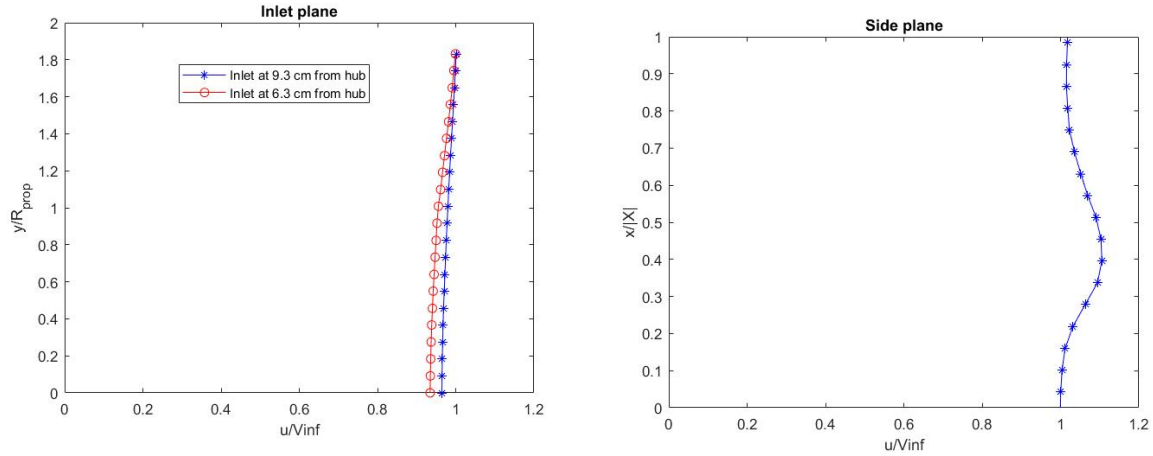

(a) Axial flow velocity u at inlet plane for both distances (9.3 cm and 6.3cm). The flow flow stagnates at the hub, the effects are larger for the closer plane (6.3 cm)

(b) Axial flow velocity variation at the side plane caused by the nacelle of the propulsor

Figure 6.12: Isolated propulsor configuration: flow velocity variation at inlet and side planes

Figure 6.13a shows the measured flow velocity at the outlet plane including extrapolated data. From Figure 5.26 it can be seen that at the outlet plane the last $11mm$ are not measured. These missing measurements are extrapolated assuming that the velocity and pressures remain constant. The reason for assuming these values as constant is due to the small boundary layer of the motor casing and that there is no theoretical model or CFD available to estimate the values. The boundary layer thickness of the motor casing has been approximated by the thickness of a turbulent boundary layer over a flat plate:

$$\delta_{plate} = \frac{0.37x}{Re^{1/5}} \tag{6.5}$$

The results of this equation shows a boundary layer thickness of approximately $1.5mm$. Since the boundary layer is small the parameters such as flow velocity and pressure are assumed constant.
This extrapolated data is quite important when computing the power terms from the power balance method as it will be shown later in this section. In Figure 6.12b one can observe the wake of the nacelle around $\frac{y}{R_{prop}}$ approximately 1 and 1.2, since the flow velocity decreases. Below $\frac{y}{R_{prop}} = 1$ the velocity increases rapidly since the jet of the propulsor is measured. The total pressure depicted in Figure 6.13b at the outlet plane also shows similar behaviour as with the axial flow velocity.

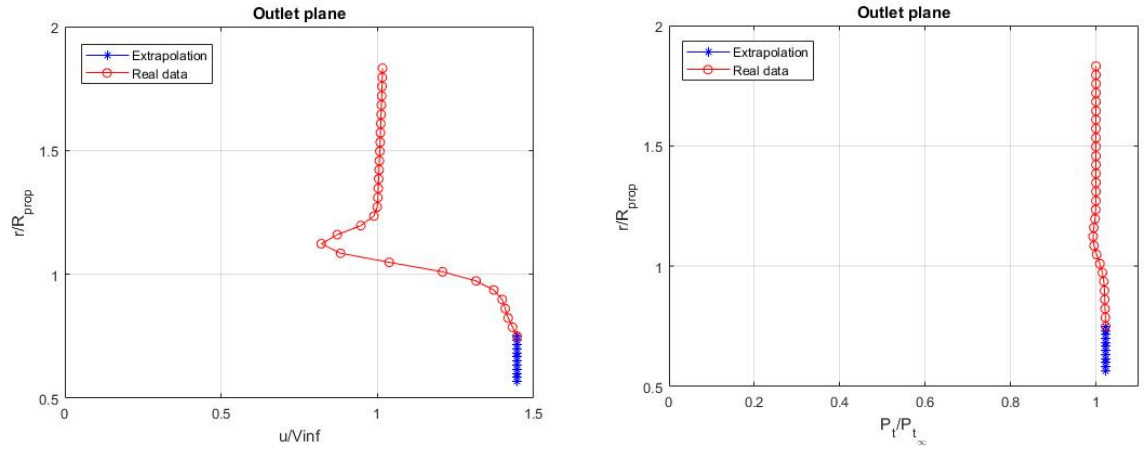

(a) Flow velocity at the outlet propulsor plane including the extrapolated data up to the motor casing

(b) Total pressure ($\frac{p_t}{p_{t_\infty}}$) at the propulsor outlet plane including the extrapolated data up to the motor casing

Figure 6.13: Isolated propulsor configuration: outlet plane axial flow velocity and total pressure

Extra measurements were carried at the inlet of the propulsor in order to check the axisymmetry of the flow, similarly to the measurements behind the TE of the body shown in Figure 5.6. Figures 6.14a and 6.14b show these measurements and they all follow the same behaviour as expected. The measurements for the top side were stopped at a smaller distance than the others because the wing that carries the five hole probe could not move further upwards. Again, the flow is stagnating at the propulsor's hub and increasing in velocity further away from it.

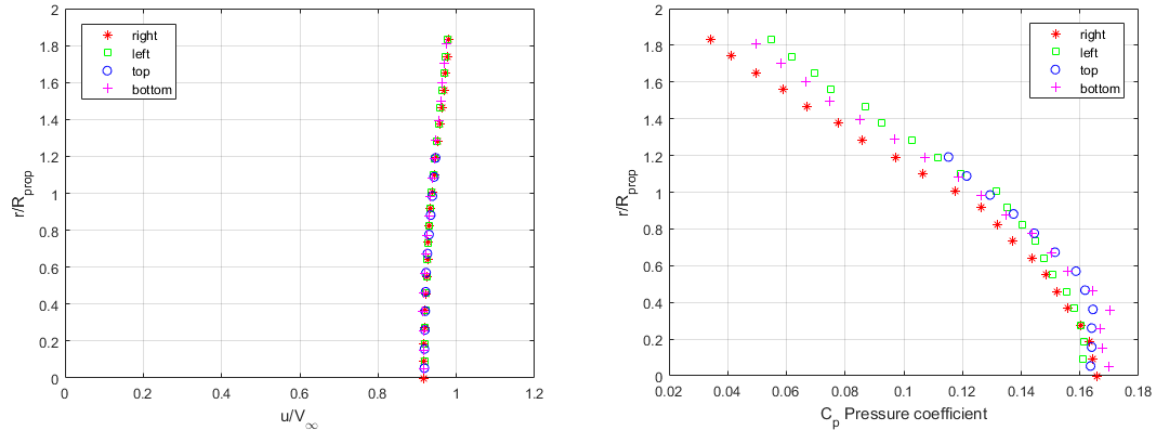

(a) Flow velocity variation at propulsor's inlet

(b) Pressure coefficient variation at propulsor's inlet

Figure 6.14: Comparison of inlet measurements at 6.3 cm from the propulsor's hub in order to check axisymmetry

When measuring with the five-hole probe around the control surface, the balance readings were affected by its presence. Figure 6.15 shows the variation of around 4.5 % in load cell measurements at the outlet plane when the five-hole probe translates in the radial direction. The thrust starts to decrease when it is in the jet of the propulsor ($r/R \leq 1$). A plausible cause for this variation is that the five-hole probe could trigger flow separation, thus increasing the drag and reducing the thrust measured.

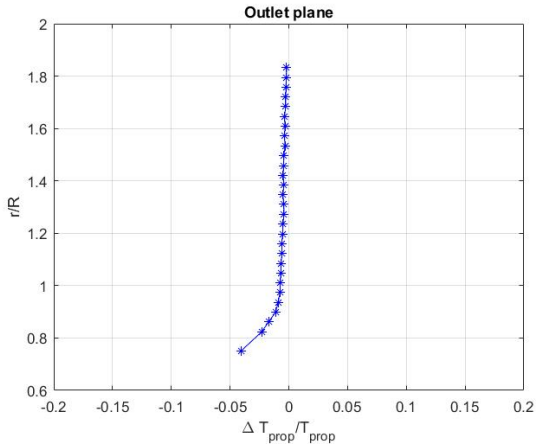

Figure 6.15: Load cell measurements of the propulsor when the FHP is traversing the outlet plane

The power terms from the power balance method of the isolated propulsor are computed and summarized in Table 6.2. These terms are computed assuming that the flow is axisymmetric. Therefore, the surface integrals can be expressed as shown in equation 6.6:

$$\iint dS = \int_0^{radius} 2\pi y dy \tag{6.6}$$

The table is divided in 2 cases: the isolated propulsor where the inlet plane is measured at 9.3 or 6.3 cm from the hub. The net streamwise force in this case is the thrust measured $8.1N$ which in turn is equal to the body drag at $M = 0.176$. The mechanical flow power at the inlet plane slightly differs comparing the two cases and is relatively small compared to the outlet plane which is at the jet of the propulsor. The side plane does not add any meaningful mechanical flow power to the total sum as expected. However if the propulsor was an open rotor then it may be non-negligible.

Table 6.2: Isolated propulsor power terms

Configuration	**Isolated prop (9.3 cm)**	**Isolated prop (6.3 cm)**
P_E [W]	2070	2070
C_{P_E}	0.3702	0.3702
C_{P_K}	0.2694	0.2749
$C_{\Phi_{jet}}$	0.0466	0.0466
F_x [N]	8.1	8.1
C_{P_K} inlet	0.015	0.016
C_{P_K} side	-1.45E-05	-1.20E-05
C_{P_K} outlet	0.2535	0.2535

The propulsive efficiency and overall efficiencies are shown in Table 6.3. The propulsive efficiency (η_p) is around 83% and the three centimeters difference between inlet planes is negligible. The overall efficiency (η_o) found is between 73% and 74% for the isolated propulsor case.

Table 6.3: Isolated propulsor: total and propulsive efficiency

Configuration	η_p	η_o
Isolated prop (9.3 cm)	0.83	0.73
Isolated prop (6.3 cm)	0.83	0.74

2.1 Isolated propulsor with upstream strut

The isolated propulsor including the upstream strut was tested with the same procedure used with the isolated propulsor configuration. Firstly, the RPM is varied at $M = 0.176$ and the propulsive force

generated by the propulsor is measured with the load cell. From these measurements the thrust and power coefficients can be computed against the advance ratio. Figure 6.16 shows that there are no large variations of thrust coefficient nor power coefficient between the isolated propulsor and the isolated propulsor including the upstream strut.

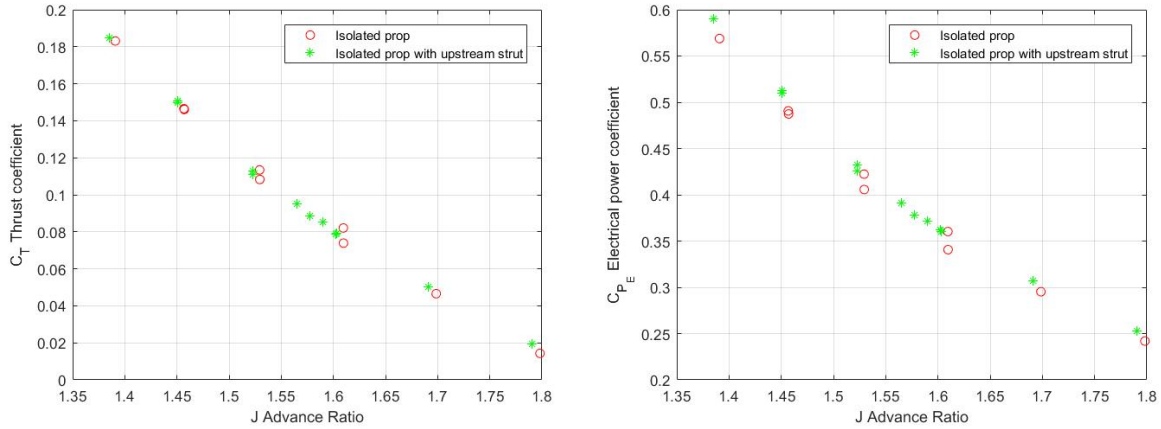

(a) Thrust coefficient comparison between the isolated propulsor and the isolated propulsor with upstream strut configurations

(b) Electrical power coefficient comparison between the isolated propulsor and the isolated propulsor with upstream strut configurations

Figure 6.16: Thrust variation due to the presence of the five-hole probe at outlet plane

Five-hole probe measurements

The five-hole probe measurements were carried at the unaccelerated condition and $M = 0.176$. Unlike the isolated propulsor case, these measurements were performed twice but on opposite ends, they are a "mirror" from each other. They are named "left" (port side) and "right" (starboard) following the naming convention of Figure 5.6. Therefore, one expects that these measurements are the same for both planes since they should be symmetric. The mirror measurements were performed at the inlet, side and outlet planes. Insignificant differences between left and right measurements can be observed with the flow velocity measurements at the inlet and side planes, shown in Figures 6.17a and 6.17b. At the inlet plane, the top and bottom were also measured to check axisymmetry of the flow. Figure 6.17a shows a lower flow velocity measured for the bottom side at $\frac{r}{R_{prop}} \leq 1.2$ caused by the wake of the upstream strut.

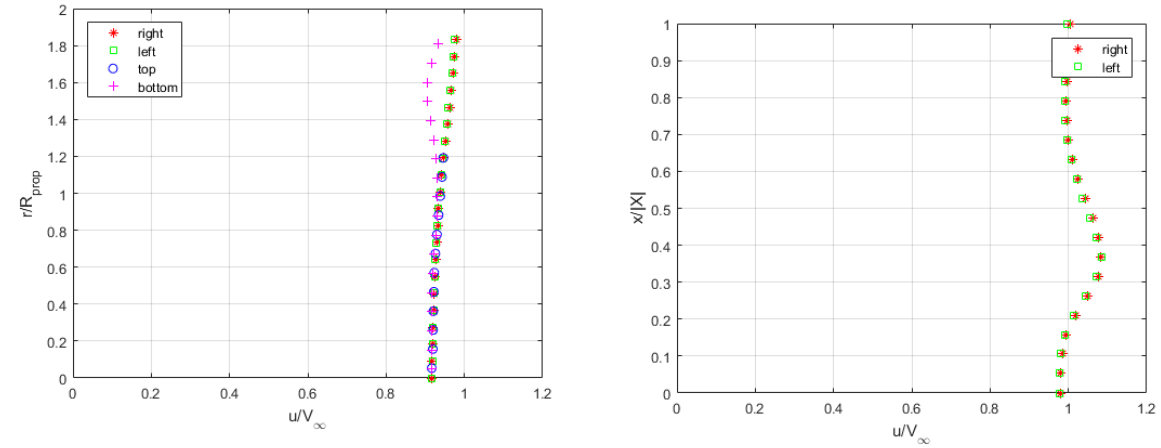

(a) Inlet plane flow velocity measured at 6.3 cm from the propulsor's hub

(b) Side plane flow velocity

Figure 6.17: Inlet and side planes flow velocity of propulsor with upstream strut

Large differences (up to 24%) between the starboard and port side are found at the outlet plane flow velocity presented in Figure 6.18. Furthermore, another important term to investigate is the total pressure difference with respect to free-stream $P_t - P_{t_\infty}$ since it is relevant to the computation of the mechanical flow power, see equation 3.1. Figure 6.19 shows the total pressure difference at the outlet plane, these differences are smaller than 1%. The largest differences in flow parameters between left and right are observed at the outlet plane. These differences at the outlet plane change significantly the outlet power terms such as C_{P_K} outlet and Φ_{jet} as can be observed in Table 6.4. The plausible causes for these differences at the outlet plane can be:

- The flow is not axisymmetric due to the stators of the ducted fan not perfectly recovering the swirl of the flow. Also, the slipstream of the propulsor could be impinged on the strut magnifying the differences between both sides.
- The total pressure is measured using the center hole of the FHP directly instead of deriving it. However, the total pressure is only sensitive to flow angles larger than 45° (E.M. Houtman & Banning, 1989), in this case relatively small angles are observed, see Figure 6.20. The angle of attack α and angle of side-slip are defined in Figure 6.21. The angle of attack α could also be represented as an azimuthal angle at 90 degrees varying around 5 degrees.
- The propulsor itself could be slightly misaligned with the free-stream flow. Similarly, the five-hole probe could also be slightly misaligned with the flow.

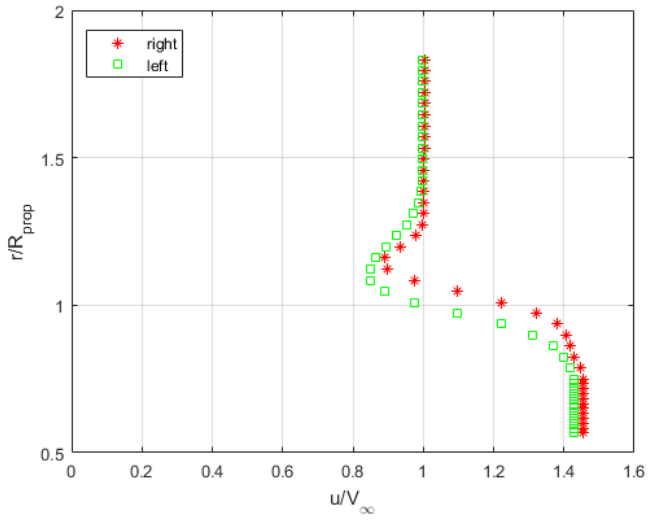

Figure 6.18: Variation of flow velocity at the outlet plane of propulsor with upstream strut

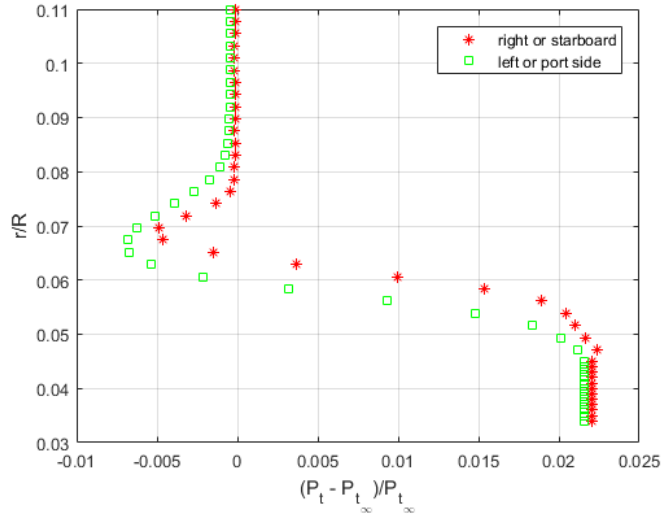

Figure 6.19: Isolated propulsor with upstream strut results: outlet plane total pressure difference measurements. Small differences in pressure found between left and right planes.

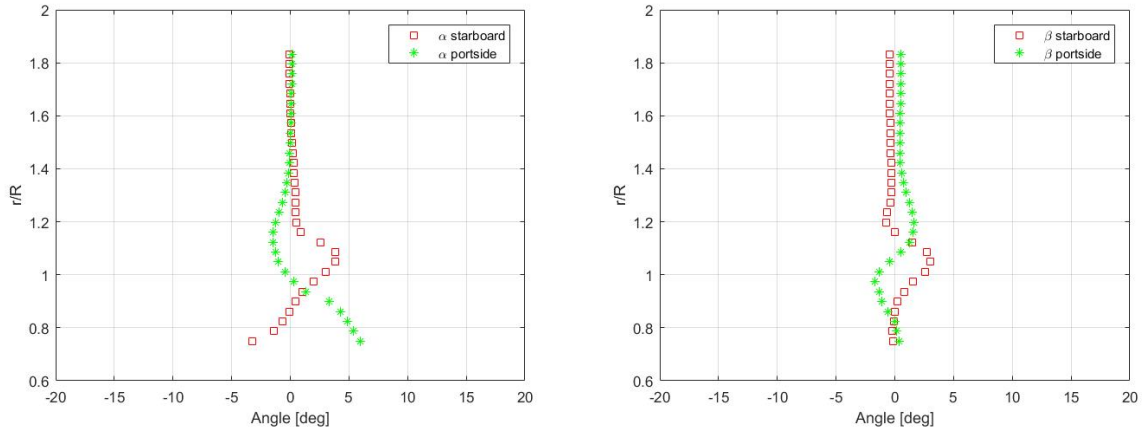

(a) Angle of attack α

(b) Angle of side slip β

Figure 6.20: Isolated propulsor with upstream strut results: Angle of attack α and side-slip β at the outlet plane

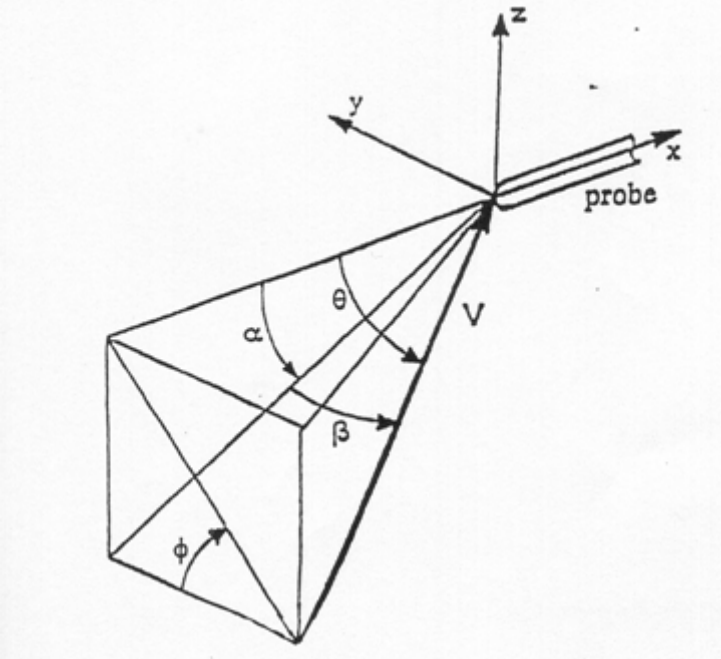

Figure 6.21: Five-hole probe angle definition

The results of the power analysis are shown in Table 6.4. In this table four different cases were analyzed since the inlet plane was measured at two different distances from the hub (6.3cm or 9.3cm) and measurements were carried out at the right side and left side of the propulsor.
The mechanical flow power C_{P_K} and jet dissipation (Φ_{jet}) show significant differences between left and right. These differences are due to the large velocity differences encountered at the outlet plane. Since the mechanical flow power and jet dissipation are required to compute the propulsive efficiency, the propulsive efficiency also shows these differences between left and right. The computed propulsive efficiency is 83% for the right (starboard) side as shown in Table 6.5, being the same for the isolated propulsor configuration and 77% if the left measurements are used for computations. When comparing the starboard side flow measurements, insignificant differences are found between the isolated propulsor configuration and the isolated propulsor with upstream strut configuration. The electric power stays consistent across all cases since it does not depend on left and right measurements.

Table 6.4: Isolated strut including upstream strut results: power terms

Configuration	**Propulsor + strut (6.3 cm) right**	**Propulsor + strut (6.3 cm) left**	**Propulsor + strut (9.3 cm) right**	**Propulsor + strut (9.3 cm) left**
P_E [W]	2133	2133	2135	2096
C_{P_E}	0.3631	0.3631	0.3585	0.3617
C_{P_K}	0.2507	0.1768	0.2471	0.1765
$C_{\Phi_{jet}}$	0.0424	0.0383	0.0431	0.0404
F_x [N]	8.12	8.12	8.08	8.12
C_{P_K} inlet	0.0086	0.0136	0.0021	3.67E-05
C_{P_K} side	8.10E-05	1.03E-04	1.23E-05	3.38E-05
C_{P_K} outlet	0.242	0.1631	0.25	0.1765

Table 6.5: Propulsive and overall efficiency for the isolated propulsor including upstream strut configuration

Configuration	η_p	η_o
Isolated prop + strut (6.3 cm) right	0.83	0.69
Isolated prop + strut (6.3 cm) left	0.78	0.49
Isolated prop + strut (9.3 cm) right	0.83	0.69
Isolated prop + strut (9.3 cm) left	0.77	0.49

3 Integrated system

In this section the results of the integrated systems (BLI and WI configurations) are presented. The first test is to study the performance of the propulsor in the boundary layer ingestion and wake ingestion configurations. At $M = 0.176$ the RPM of the propulsor is varied and the thrust and electric power are measured. The results are shown in Figure 6.22 where the electric power coefficient C_{P_E} (defined in equation 3.3) is plotted against the coefficient of net force C_x. In the isolated propulsor case where the body is not present, the net streamwise force is defined as difference between the thrust coefficient and the body drag coefficient: $C_x = \frac{T_{prop} - D_{body}}{q_\infty} = C_T - C_{D_{body}}$. The body drag coefficient is obtained from the previous isolated body measurements.
The electric power in the wake ingestion case is corrected since the drag of the body decreases when translating upstream, thus less power is required. Therefore, assuming a constant body drag coefficient, an equivalent electric power coefficient can be obtained by introducing an equivalent free-stream flow velocity. Figure 6.22 shows the corrected and uncorrected electrical power coefficient. In the next figures, only the corrected electric power coefficient is shown.
If the electric power consumed in the BLI and WI configurations is compared with the isolated propulsor configuration, less electric power for a given net force is required. A power savings of $29.0\% \pm 2.9\%$ is found for BLI configuration while a $24.3\% \pm 2.9\%$ is found for the WI configuration for the unaccelerated condition $C_x = 0$. It can also be seen that BLI and WI consume less electrical power for the entire C_x range. The results can be compared to similar experiments from literature where an axisymmetrical fuselage is placed in front of the propulsor:

- Carrier, Atinault, Grenon, and Verbecke (2013) performed a similar study of an axisymmetrical body with a propulsor behind it. They tested the propulsor at two distances from the trailing edge of the body: at 50 mm and 200 mm. At 50 mm the power savings is 22% and at 200 mm it is approximately 19%.
- Sabo and Drela (2015) found a power savings coefficient up to 29% and the power savings decreased when the propulsor is moved downstream away from the trailing edge of the fuselage.
- P. Lv, Ragni, Hartuc, Veldhuis, and Rao (2017) found power savings in the BLI configuration of $18 \pm 1.4\%$ and for the WI configuration $10 \pm 1.4\%$.

The results in literature shows significant variance, but overall a positive benefit is found.

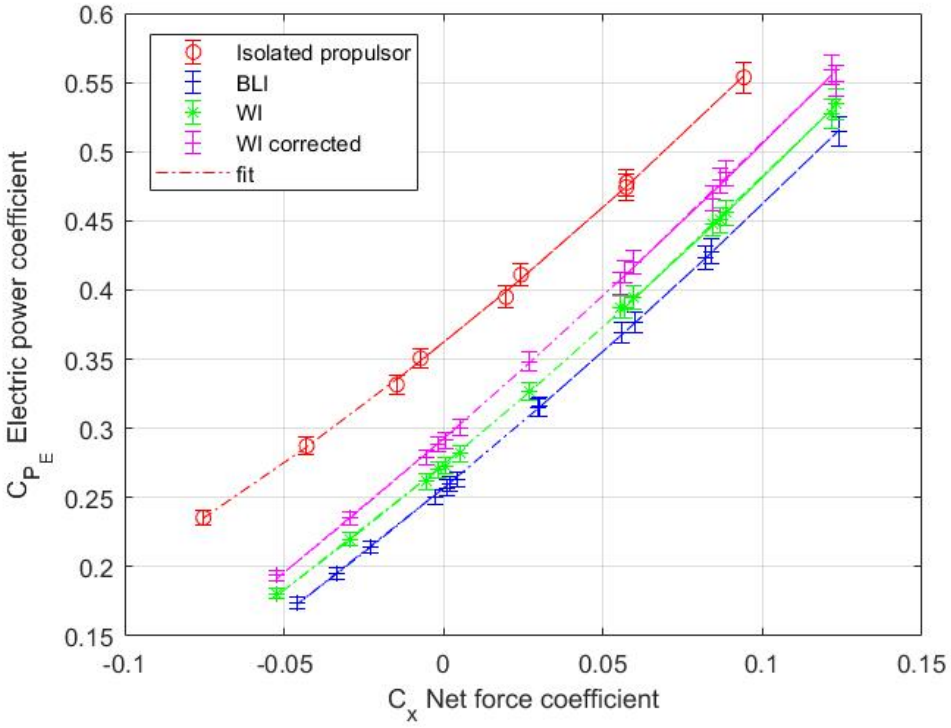

Figure 6.22: Results for the three different configurations (C_{P_E} vs C_x) at $M = 0.176$

The electrical power coefficient variation with advance ratio for all three configurations are shown in Figure 6.23a. Nevertheless, it is difficult to conclude anything since the error bars overlap between the curves. On the other hand, the thrust coefficient can also be plotted against the advance ratio, shown in Figure 6.23b. In this figure a larger thrust coefficient for a given advance ratio can be observed for the BLI and WI configuration compared to the isolated propulsor case. It is worth to note that the advance ratio is computed using the free-stream flow velocity.

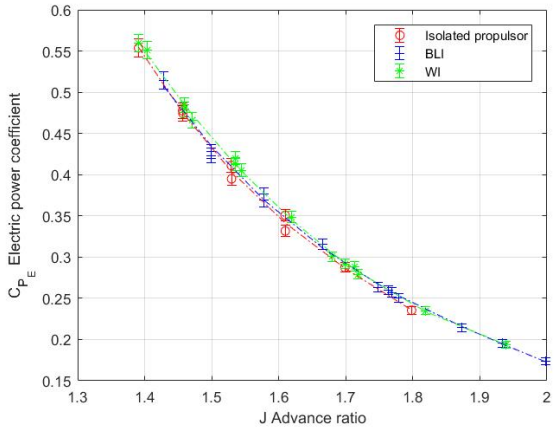

(a) Electrical power coefficient variation against advance ratio

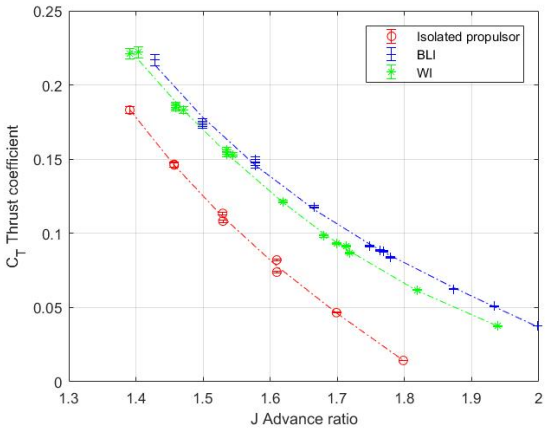

(b) Thrust coefficient variation against advance ratio

Figure 6.23: Thrust and power coefficient for all configurations at $M = 0.176$

Five-hole probe measurements

The flow velocity axisymmetry was inspected at the inlet of the propulsor in the BLI configuration, by measuring in all four directions similarly for the isolated body experiment (see Figure 5.6). The results of these measurements can be seen in Figure 6.24. In this figure the body wake can be observed, the velocity grows from the center of the propulsor towards the edges reaching free-stream values. Furthermore, the propulsor's hub also has an influence in the flow similarly to the isolated propulsor case (see Figure 6.12a). On the other hand, significant differences can be observed for the "bottom" measurements around $\frac{y}{R_{prop}} = 1.2$. The reason for these differences is the wake of the strut of the body. Since the differences become important from $\frac{y}{R_{prop}} = 1.2$, the body-strut wake is not ingested by the fan. Furthermore, for the flow velocity at the left or port side also shows differences possibly caused by a slight body or five-hole probe misalignment.

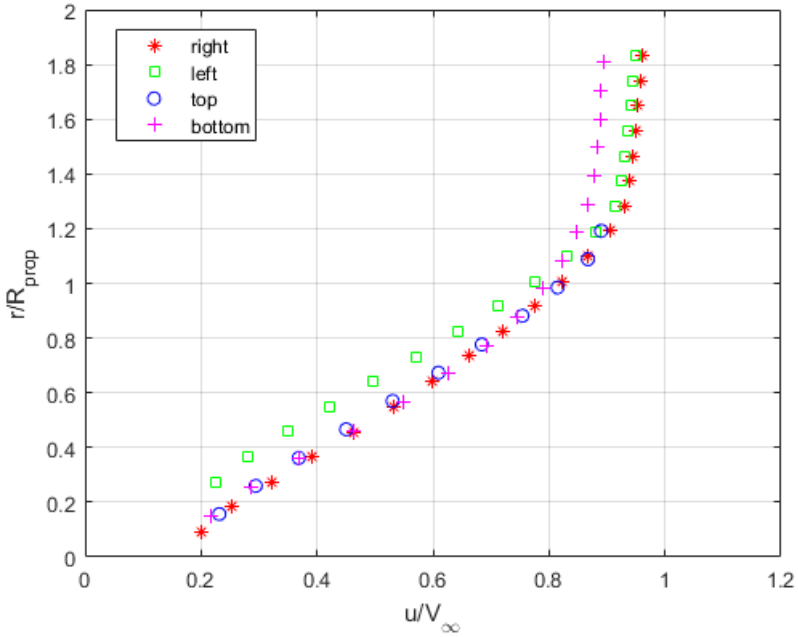

Figure 6.24: Inlet flow velocity for BLI system at a distance of 6.3 cm from the hub

The five-hole probe measurements were carried around the control surface in both the starboard and port side, in the same fashion as for the isolated propulsor with the upstream strut. The probe measurements were carried at the unaccelerated condition at $M = 0.176$. In order to set the thrust equal to the body drag, the five-hole probe was first shifted far away from the model such that there is the least interference possible. Once the unaccelerated condition is set, the five-hole probe measurements around the control surface begin.
The differences in flow velocity between starboard and port side at the inlet, side and outlet planes are shown in Figures 6.24, 6.25a and 6.25b.
The variation of the flow velocity at the side plane can be observed in Figure 6.25b and its variation is much lower relative to the inlet or outlet planes. To further clarify, $|X|$ is the distance the five-hole probe translates from the inlet plane to the outlet plane $X = 250mm$. The flow velocity at the side plane increases and then decreases due to the geometry of the propulsor's nacelle. The nacelle starts with a convex shape, thus velocity is accelerated. Then the flow velocity decelerated due to an adverse pressure gradient.
The largest differences in flow velocity between starboard (right) and port (left) sides are observed (up to 11%) at the outlet plane depicted in Figure 6.25a. Around $\frac{y}{R_{prop}} = 1$ the flow velocities sharply decrease due to the wake of the casing of the fan. Then, at $\frac{y}{R_{prop}} < 1$ the flow velocity increases due to measuring at the jet of the propulsor. There is a large flow velocity gradient, this means than any slight error or uncertainty in the measurements can lead to a significant difference in flow velocity. The reason of differences in flow velocity between the left and right planes are due to the aforementioned factors.

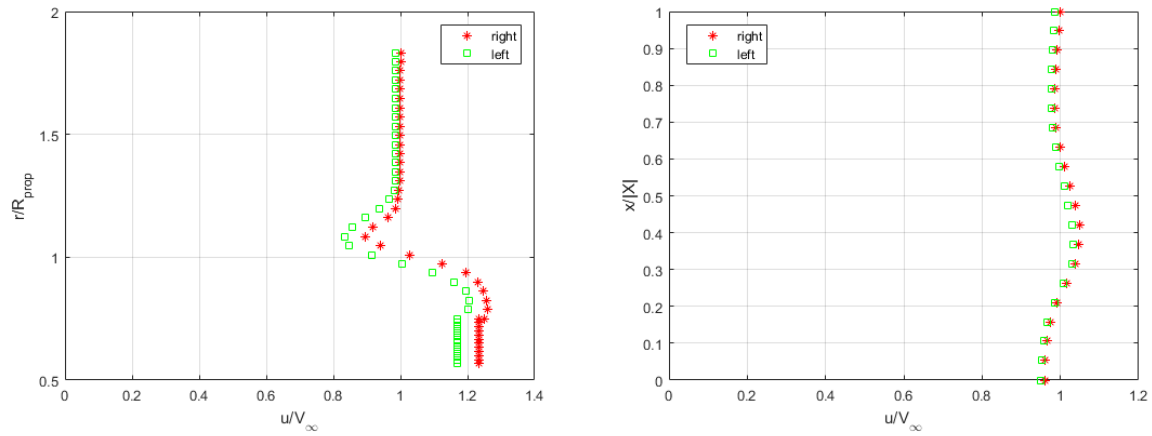

(a) Outlet plane flow velocity, up to 11.5% difference in flow velocity found between left and right planes

(b) Side plane flow velocity, no significant differences between left and right

Figure 6.25: Outlet and side planes flow velocity of BLI system

The difference of total pressure $P_t - P_{t_\infty}$ and flow velocity measured at the control surface are important terms when computing the mechanical flow power, see equation 3.1. When analyzing the outlet plane starboard/port-side differences in total and static pressure and flow velocity at the outlet plane can also be observed. Figure 6.26 shows the total pressure difference with respect to free-stream total pressure at the outlet plane. These differences between left and right measurements are in the other of less than 1%, adding uncertainty to the computed mechanical flow power and jet dissipation.
Since the total pressure was measured using the center hole of the five-hole instead of deriving it, possible uncertainties may arise. For flow angles lower than 45° the uncertainty in measured total pressure is negligible $|\frac{\Delta p_t}{\Delta p_{t_{infty}}}|_{max} = 0.004$ (E.M. Houtman & Banning, 1989). Figure 6.27 shows the angles of attack α and side-slip β at the outlet plane, the flow angles are clearly lower than 10°.

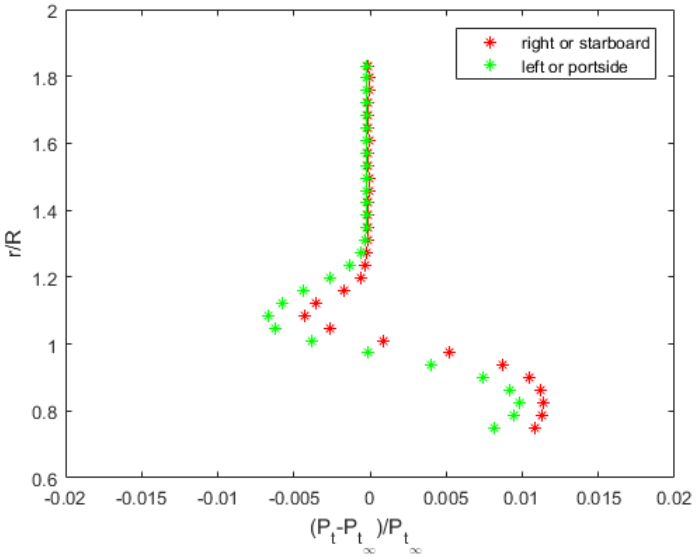

Figure 6.26: BLI results: Small differences in total pressure at the outlet plane between the left and right sides

Moreover Figure 6.27 shows that the angle of side-slip β is not zero for free-stream conditions(for $y > 0.6m$). This means that the probe is measuring a free-stream that is slightly skewed. Nevertheless, the most probable cause is that the probe itself is misaligned. This is not seen for the up and down alignment where the angle α remains zero for the free-stream flow. Furthermore, another contributor

to the differences between the port and starboard sides is that the stators do not recover the swirl produced by the propulsor completely. In addition, the slipstream flow could also be impinged on the strut magnifying the differences between both sides. For this reason the angle of attack α is asymmetric at the propulsor's jet ($r/R \leq 1$).

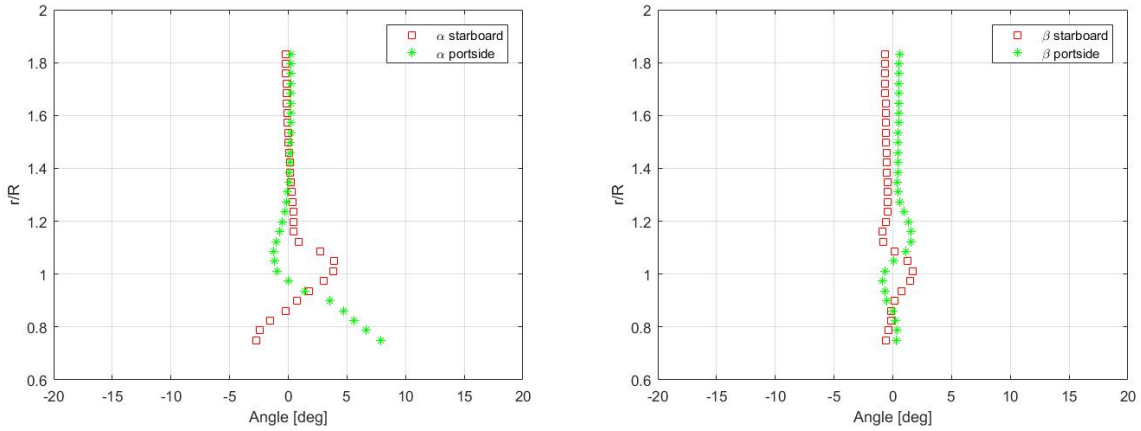

(a) Angle of attack α

(b) Angle of side slip β

Figure 6.27: BLI results: Angle of attack α and side-slip β at the outlet plane

The WI ingestion configuration is the configuration where there is no static pressure interference between the body and the propulsor. The propulsor is located $0.6m$ downstream from the body's trailing edge. In this configuration the flow velocity at the inlet plane of the propulsor(see Figure 6.28) is higher compared to the BLI configuration (Figure 6.24). The velocity is larger because the wake of the body is re-energized along the streamwise direction.

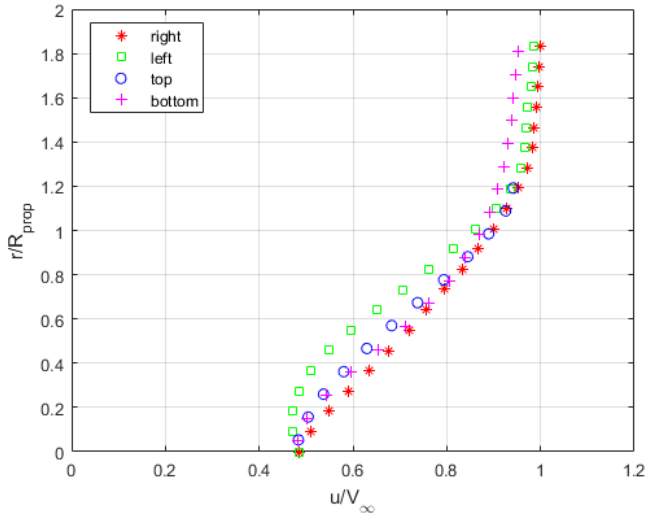

Figure 6.28: WI results: inlet plane flow velocity axisymmetry

For the wake ingestion configuration the difference in flow velocity also varies significantly specially at the outlet plane. Figure 6.29a shows the variation of flow at the outlet plane. Similarly to the isolated propulsor including upstream strut and the BLI configuration there is a difference between the left and the right planes. This causes large differences when integrating to obtain the power terms. In addition, the last measured point at the outlet before extrapolating (and assuming a constant value), shows a varying trend. Therefore, the assumption of maintaining a constant total pressure or flow velocity for the extrapolated part leads to higher uncertainty. Again, small differences are found for the total pressure as shown in Figure 6.29b.

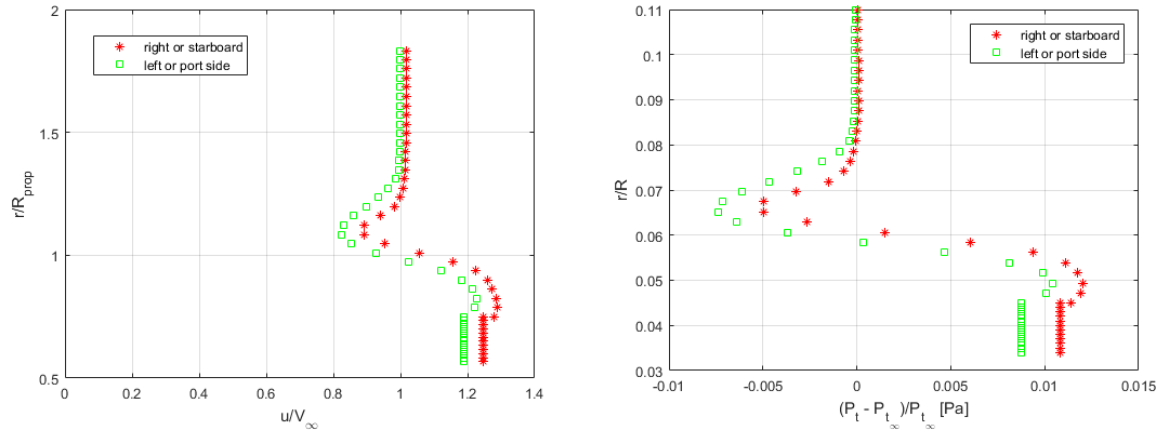

(a) Large differences in flow velocity between left and right

(b) Small differences in total pressure between left and right

Figure 6.29: WI results: flow velocity and total pressure at the outlet plane

All these flow measurements were performed at the unnacelerated condition (thrust = drag) and $M = 0.176$. From these measurements the power terms can be computed. Firstly, the mechanical flow power can be computed independently for each plane: inlet, side and outlet planes. In this way it is possible to determine the importance of each side and the relation with other terms such as propulsive efficiency. The power terms for both BLI and WI configurations are summarized in Table 6.6 (10.8 cm and 7.8 cm refer to the distance between the trailing edge of the body and the propulsor's hub).
The mechanical flow power, given by equation 3.1, is dependent on the total pressure difference and the axial flow velocity. Theoretically for the isolated propulsor case the difference of total pressure should equal zero $P_t - P_{t_\infty} = 0$ at the inlet, thus no mechanical flow power should be found at the inlet plane. On the other hand for the BLI and WI configurations a total pressure gradient exists, therefore the mechanical flow power C_{P_K} becomes a relevant term for these integrated systems. Figure 6.30 shows the total pressure gradient at the inlet plane for all configurations, the gradient is noticeable larger for BLI and WI configurations. Furthermore, Table 6.6 shows that C_{P_K} at the inlet has increased compared to the isolated propulsor case, see Table 6.2. For example, for the BLI configuration (where the distance between the trailing edge of the body and the propulsor's hub is 7.8 cm) $C_{P_K} = 0.0722$ and for the isolated propulsor $C_{P_K} = 0.015$ both measured at the right plane. Therefore, the wake becomes an extra power input term for the BLI and WI configurations. The mechanical flow power at the side plane is negligible for all configurations.
However, when computing the mechanical flow power large variations between the left and right planes are found. These discrepancies come from the variations of flow velocity, total and static pressures as shown previously in this section. The largest differences in C_{P_K} between left and right are found at the outlet.

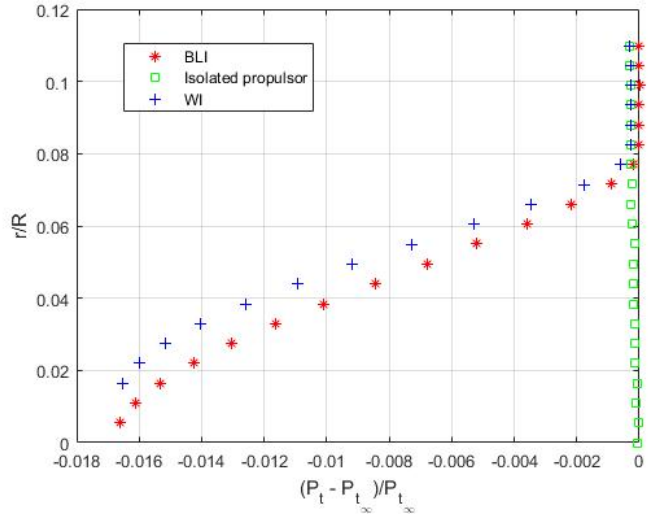

Figure 6.30: Inlet plane total pressure gradient comparison between the BLI, WI and isolated propulsor configurations.

Table 6.6 and Figure 6.31 show that the jet dissipation has decreased significantly as expected since the propulsor is filling the wake produced by the fuselage. For instance, for the BLI configuration the jet dissipation has decreased up to 78% or 73% (depending whether the left or right side is used). The jet dissipation is the sum of the axial ($\dot{E}_a$) and transverse ($\dot{E}_v$) kinetic energy dissipation rate and the wake pressure-defect ($\dot{E}_p$). The decomposition can be observed in Figure 6.31 (for the starboard side), where it can clearly be observed that the axial kinetic energy dissipation rate is the most dominant term. This term greatly reduces in the BLI and WI configurations compared to the isolated propulsor configuration. The transverse kinetic energy is small in all configurations and does not play an important role. The pressure term on the other hand is negative and relatively small for the isolated configuration, but it is relatively more important for the integrated configurations. It is noteworthy that at the outlet plane, the small area extrapolated to the casing of the motor is important when computing the power terms. For the port side the same pattern is observed, the jet dissipation is reduced for BLI and WI configurations. The electric power is measured each time for every configuration, thus it is possible to also compute the electric power coefficient and consequently the power savings coefficient. Since the body in the WI configuration experiences a lower drag, the electric power coefficient has been corrected by assuming a constant drag coefficient and computing an equivalent flow velocity. This flow velocity is used to compute an equivalent electric power coefficient.

Table 6.6: BLI and WI power terms

Configuration	**BLI (10.8 cm) right**	**BLI (7.8 cm) right**	**BLI (10.8 cm) left**	**BLI (7.8 cm) left**	**WI right**	**WI left**
P_E [W]	1459	1441	1449	1454	1444	1512
C_{P_E}	0.2484	0.2752	0.2422	0.237	0.2839	0.2907
C_{P_K}	0.1906	0.1415	0.1251	0.1178	0.1834	0.1288
$C_{\Phi_{jet}}$	0.0136	0.0105	0.0118	0.0099	0.014	0.0124
F_x [N]	0.03	0.05	0.00	0.07	-0.15	-0.06
C_x	0.000	0.000	0.000	0.000	0.001	0.000
C_{P_K} inlet	0.0945	0.0631	0.0818	0.0818	0.0766	0.0881
C_{P_K} side	1.16E-05	1.63E-05	-2.74E-05	1.68E-05	-2.01E-05	4.09E-05
C_{P_K} outlet	0.096	0.0783	0.0434	0.036	0.1068	0.0406

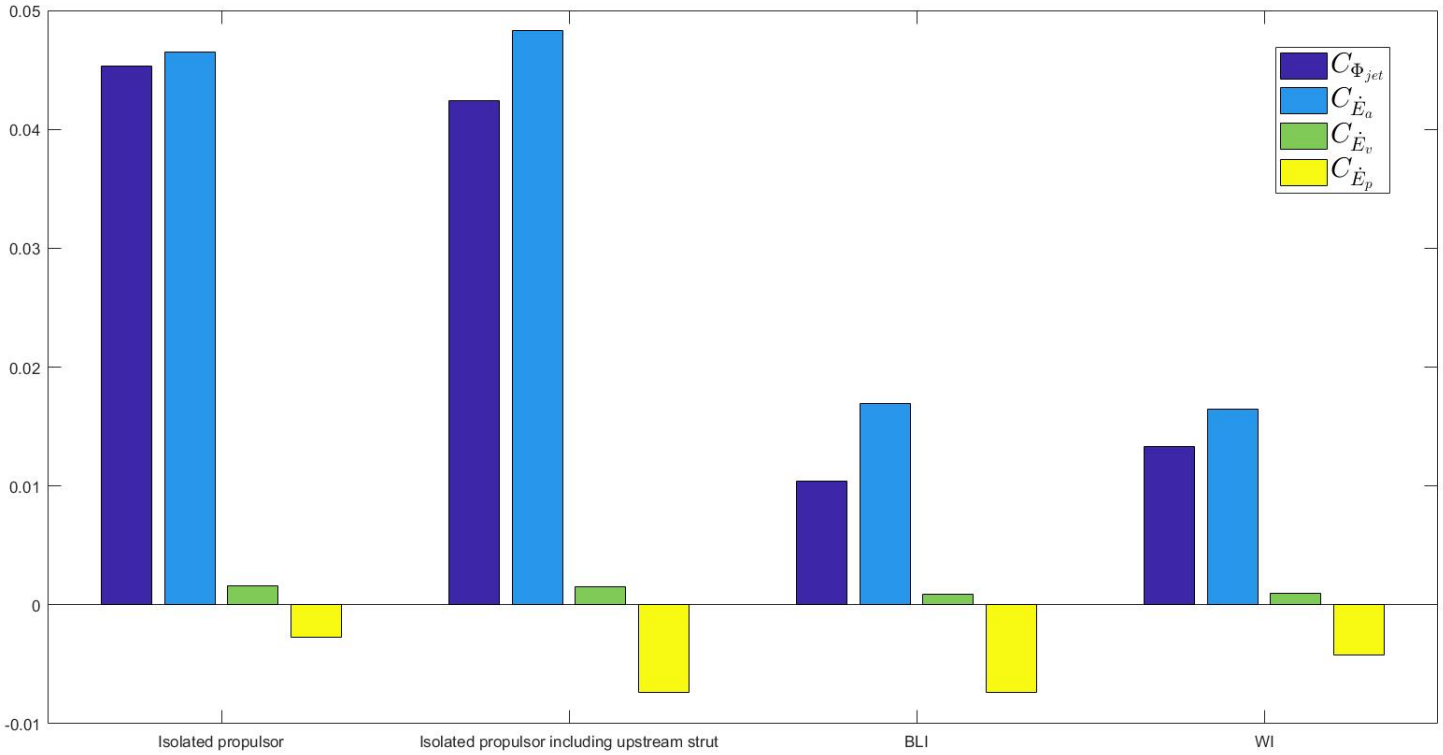

Figure 6.31: Jet dissipation decomposition (starboard side) for isolated propulsor, isolated propulsor including the upstream strut, BLI and WI configurations

From the electric power and mechanical flow power of the integrated system and the isolated propulsor configuration the power savings coefficient can be computed. The power savings coefficients are summarized in Table 6.7. An overall benefit is found, but it does vary quite significantly if computed with the mechanical flow power. The differences in power savings between left and right are quite significant. This shows how important it is to accurately measure each quantity.

Table 6.7: Power saving coefficient

Configuration	$PSC_{C_{P_K}}$	$PSC_{C_{P_E}}$
BLI (10.8 cm) right	29.25%	32.90%
BLI (7.8 cm) right	47.48%	25.66%
BLI (10.8 cm) left	53.56%	34.58%
BLI (7.8 cm) left	56.27%	35.98%
WI right	31.92%	23.31%
WI left	52.19%	21.47%

The propulsive efficiency increased 83% up to 93% and is insensitive to what plane or configuration is measured. The propulsive efficiency is high compared to the 78.9% efficiency found for the D8 double bubble aircraft (Hall et al., 2017). However, the D8 aircraft only ingested 40% of the boundary layer of the fuselage. The overall efficiency shows more variance due to the significant discrepancies in mechanical flow power and jet dissipation.

Table 6.8: Propulsive and overall efficiency of BLI and WI configuration

Configuration	η_p	η_o
BLI (10.8 cm) right	0.93	0.77
BLI (7.8 cm) right	0.93	0.51
BLI (10.8 cm) left	0.90	0.52
BLI (7.8 cm) left	0.91	0.50
WI right	0.92	0.65
WI left	0.90	0.44

Chapter 7

Uncertainty analysis

For any type of experimental study experimental observations always have errors or uncertainties. These observations are used to calculate a results, but have uncertainties associated with them thus the results will also have an error that depends on the error of the individual observations. In this section the propagation of uncertainty is analyzed.
Assume a variable γ that depends on N statistically-independent variables x_i:

$$\gamma = f(a, b, c...) \tag{7.1}$$

The error of the variable γ is the root-sum-square of the relative errors of each variable. Note that for the remainder of this section all observations are considered to be independent, meaning that they are uncorrelated.

$$\sigma_\gamma = \sqrt{(\frac{\partial \gamma}{\partial a})^2(\sigma_a)^2 + (\frac{\partial \gamma}{\partial b})^2(\sigma_b)^2 + (\frac{\partial \gamma}{\partial c})^2(\sigma_c)^2...} \tag{7.2}$$

Where σ_γ is the error of the variable γ, σ_{x_i} is the error of variable x_i and $\frac{\partial \gamma}{\partial x_i}$ is the sensitivity of γ with respect to the variable x_i.

To asses the uncertainty of the mechanical flow power, the errors of all measurements have to be propagated to the final metric. Therefore, the mechanical flow power can be re-written as a sum of each individual measurement:

$$P_K = \sum_i P_{K_i} = \sum_i (P_t - P_{t_\infty}) u 2\pi y \Delta y \tag{7.3}$$

The mechanical flow power depends on four different variables which are assumed to be independent from each other:

$$P_K = f(P_t, P_{t_\infty}, u, y) \tag{7.4}$$

The total uncertainty is the root-sum-square of each uncertainty:

$$\sigma_{P_K} = \sqrt{\sum_i \sigma^2_{P_{K_i}}} \tag{7.5}$$

Where each term is:

$$\sigma_{P_{K_i}} = \sqrt{(\frac{\partial P_K}{\partial P_t})^2(\sigma_{P_t})^2 + (\frac{\partial P_K}{\partial P_{t_\infty}})^2(\sigma_{P_{t_\infty}})^2 + (\frac{\partial P_K}{\partial u})^2(\sigma_u)^2 + (\frac{\partial P_K}{\partial y})^2(\sigma_y)^2} \tag{7.6}$$

In order to obtain the uncertainty of the mechanical flow power, the uncertainties of each of the variables must be known. The uncertainty for each variable is given by DNW. The uncertainty for the free-stream total and static pressure which is measured by pressure transducers is 1.35 Pa. The uncertainty of the tunnel temperature which is measured by temperature probes is $0.03K$.
The uncertainty for the quantities measured with the five-hole probe is also given by DNW and the uncertainty for the flow angles α and β is one degree and the flow velocity V has an uncertainty of $1.5m/s$. The uncertainty of the total and static pressure measured by the five-hole probe is assumed

to be the same as for the tunnel uncertainty (1.35 Pa), since DNW does not have the uncertainty for these quantities. The uncertainty for distance y is one millimeter. With this information it is possible to compute the uncertainty of the mechanical flow power. However, one factor not taken into account when computing the uncertainty is the error due to the extrapolation in the outlet plane. The uncertainty can also be written in a fractional manner $\frac{\sigma_{P_E}}{P_E}$ giving a percentage as a solution.
In a similar manner, the fractional uncertainty of other derived terms such as the jet dissipation, propulsive efficiency and electric power can be computed, as shown in Table 7.1.

Table 7.1: Fractional uncertainty in terms of % for the power terms and efficiency

Configuration	$\frac{\sigma_{P_E}}{P_E}$ (%)	$\frac{\sigma_{P_K}}{P_K}$(%)	$\frac{\sigma_{\Phi_{jet}}}{\Phi_{jet}}$ (%)	$\frac{\sigma\eta_p}{\eta_p}$(%)	$\frac{\sigma\eta_o}{\eta_o}$ (%)
Isolated prop (6.3 cm) right	2.03	0.70	2.70	0.58	2.15
Isolated prop (9.3 cm) right	2.03	0.68	3.29	0.71	2.14
Isolated prop + strut (6.3 cm) right	2.03	0.66	2.99	0.62	2.13
Isolated prop + strut (6.3 cm) left	2.03	0.86	3.33	0.97	2.20
Isolated prop + strut (9.3cm) right	2.04	0.67	2.86	0.62	2.15
Isolated prop + strut (9.3cm) left	2.04	0.85	2.72	0.85	2.21
BLI (7.8 cm) right	2.08	0.91	4.64	0.33	2.27
BLI (7.8 cm) left	2.09	1.56	4.77	0.51	2.61
BLI (10.8 cm) right	2.08	0.87	4.99	0.38	2.25
BLI (10.8 cm) left	2.09	1.28	4.83	0.54	2.45
WI right	2.08	0.82	5.35	0.44	2.24
WI left	2.08	1.24	4.97	0.54	2.42

Chapter 8

Conclusions

This experimental research investigates the benefits of boundary layer ingestion. Five different configurations are tested: free-stream propulsor, free-stream propulsor including the upstream strut, boundary layer ingestion (BLI) and wake ingestion (WI). An axisymmetrical body which resembles an aircraft fuselage is employed to study the effects of boundary layer ingestion. The flow terms used in the power balance method are measured using a five-hole probe, while the forces are measured using balance measurements. The main conclusions drawn from the analysis of this experimental research are:

- Five-hole probe is employed to investigate the flow power terms for a boundary layer ingesting system. The power balance method is applied to the flow velocity and pressures obtained from the five-hole probe.
- Boundary layer ingestion systems require less energy consumption compared to non-BLI systems. The benefit of BLI is due to the re-energizing of the slower moving BL and wake flow. From the experimental results it can be observed that there is a reduction of jet dissipation and an increase in mechanical flow power at the inlet plane. The jet dissipation has decreased up to 78% in the BLI configuration compared to the non-BLI case.
- The flow ingested by the propulsor in BLI configuration is not uniform. Therefore special attention is needed regarding the design of the inlet.
- The wake of the body-strut is not ingested by the propulsor, thus corrections are not necessary.
- BLI systems require $29\% \pm 2.9\%$ less power when using the electrical power as a reference compared to a non-BLI system, while WI requires $24\% \pm 2.9\%$. The power savings computed using the mechanical flow power shows more variance from 29.25% up to 56.27%. The reason for this variance comes from differences in flow parameters (specially flow velocity) found in both left/right planes. These differences are caused by an asymmetry of the flow. The stators do not recover the swirl and the slipstream impinges on the propulsor's strut. In addition, it is possible that there is a small misalignment of the five-hole probe, body or propulsor with respect to the tunnel. The power savings computed from the mechanical flow power are not reliable.
- The classical definition of propulsive efficiency is not valid for BLI or WI systems because it exceeds unity. Therefore several new definitions of propulsive efficiency were elaborated by different authors. The definition used in this thesis is given by Hall et al. (2017) and is general in nature. With this definition it can be observed that the propulsive efficiency increases by $8\% - 10\%$ for both BLI and WI configurations compared to the non-BLI configuration. The difference in propulsive efficiency between BLI and WI is minimal.

Chapter 9

Recommendations

The recommendations are differentiated into two subsections: technical and science recommendations. The technical recommendations describe the necessary steps for wind tunnel providers or research institutes to take into account when designing an experiment where the performance of BLI systems is desired to be measured. It also includes design re-considerations over the experiment carried at the LST. On the other hand, the science recommendations suggest future topics to expand knowledge about BLI.

Science recommendations:

- The flow measurements were carried with a five-hole probe. The interference of the five-hole probe with the flow should be investigated. For instance, a non-intrusive flow measurement technique such as PIV could be performed and compared to a e.g. a five-hole probe rake.
- The mechanical flow power has been investigated for a ducted fan. The mechanical flow power was only relevant at the inlet and outlet planes. However, in the case of an open rotor the side plane could be significant, therefore investigating the mechanical flow power for an open rotor should be considered. This could be an influencing factor when computing the performance of the propulsor.
- The power terms were assessed at the non-accelerated condition, other conditions should also be tested in order to observe the variation of propulsive efficiency and jet dissipation.

Technical recommendations

- If a customer would like to test their integrated systems with boundary layer ingestion, their prototypes will (probably) not be an axisymmetric fuselage with a propulsor behind it. The flow will not be axisymmetric, therefore the complete flow information at the inlet and outlet planes of the propulsor are needed. Also, as shown in this experiment the flow was asymmetric specially at the outlet plane. There are two measurement techniques suitable for these tests:
  - Particle image velocimetry it is a non-intrusive measurement techinque that can provide the complete flow field.
  - A five-hole probe rotating rake does provide all the necessary terms needed for computing the power terms. If more accurate pressure measurements are required it could be combined with a Pitot-static rake.
- Regarding this experiment, the design of the body should be reconsidered, specially the strut/body interface. The flexible plate bended twice during assembly due to the high torques applied to it. This also affects the alignment and it may affect the balance readings.
- Body only: At low wind-speeds the body drag coefficient shows a large variance with the data. This effect should be investigated further: it could be a structural problem (hysteresis) or even flow separation (unlikely).

- Reconsider the design of the propulsor. The load cell is not only measuring the thrust of the propulsor but also the drag of the casing. The propulsor's hub influences the flow in front of it, a smaller hub is recommended to diminish these effects. The motor casing should not be directly after the outlet of the propulsor, since it disturbs the flow and increases the difficulty of measuring the flow parameters (such as flow velocity and pressure).
- At the outlet plane the measurements close to the motor casing were extrapolated. Since this extrapolated area is important regarding the computation of the power terms and efficiencies, this area should be measured to decrease uncertainty.

Chapter 10

References

Anderson, J. D. (2016). *Introduction to flight* (8th Edition ed.). New York, NY: McGraw-Hill.

Carrier, G., Atinault, O., Grenon, R., & Verbecke, C. (2013, June). Numerical and Experimental Aerodynamic Investigations of Boundary Layer Ingestion for Improving Propulsion Efficiency of Future Air Transport. In *31st AIAA Applied Aerodynamics Conference.* San Diego, CA: American Institute of Aeronautics and Astronautics. Retrieved 2019-01-25, from http://arc.aiaa.org/doi/10.2514/6.2013-2406 doi: doi:10.2514/6.2013-2406

Committee on Propulsion and Energy Systems to Reduce Commercial Aviation Carbon Emissions, Aeronautics and Space Engineering Board, Division on Engineering and Physical Sciences, & National Academies of Sciences, Engineering, and Medicine. (2016). *Commercial Aircraft Propulsion and Energy Systems Research: Reducing Global Carbon Emissions.* Washington, D.C.: National Academies Press. Retrieved 2019-02-20, from http://www.nap.edu/catalog/23490 doi: doi:10.17226/23490

DNW internal report. (n.d.).

Douglass, M. (1970). *Propulsive Efficiency with Boundary Layer Ingestion* (Technical Report No. MDC J0860).

Drela, M. (2009, July). Power Balance in Aerodynamic Flows. *AIAA Journal*, *47*(7), 1761–1771. Retrieved 2019-01-25, from http://arc.aiaa.org/doi/10.2514/1.42409 doi: doi:10.2514/1.42409

E.M. Houtman, & Banning, W. (1989, April). *The calibration and measuring procedure of a five-hole hemispherical head probe in compressible flow* (Tech. Rep. No. LR-585). TU Delft.

ESDU. (1977, November). *Geometrical characteristics of typical bodies* (Tech. Rep. No. ESDU 77028).

ESDU. (1978, July). *Profile drag of axisymmetric bodies at zero incidence for subcritical Mach numbers* (Tech. Rep. No. ESDU 78019).

ESDU. (1982, June). *The pressure distribution at zero incidence over selected families of blunt axisymmetric forebodies* (Tech. Rep.).

Ewald, B. F. R. (Ed.). (1998). *Wind tunnel wall correction =: La correction des effets de paroi en soufflerie* (No. 336). Neuilly sur Seine: AGARD. (OCLC: 246199176)

Hacker Brushless motors. (2019). Retrieved 2019-10-22, from https://www.hacker-motor-shop.com/

Hall, D. K., Huang, A. C., Uranga, A., Greitzer, E. M., Drela, M., & Sato, S. (2017, September). Boundary Layer Ingestion Propulsion Benefit for Transport Aircraft. *Journal of Propulsion and Power*, *33*(5), 1118–1129. Retrieved 2019-01-29, from https://arc.aiaa.org/doi/10.2514/1.B36321 doi: doi:10.2514/1.B36321

Hardin, L., Tillman, G., Sharma, O., Berton, J., & Arend, D. (2012, July). Aircraft System Study of Boundary Layer Ingesting Propulsion. In *48th AIAA/ASME/SAE/ASEE Joint Propulsion Conference & Exhibit.* Atlanta, Georgia: American Institute of Aeronautics and Astronautics. Retrieved 2019-01-25, from http://arc.aiaa.org/doi/abs/10.2514/6.2012-3993 doi: doi:10.2514/6.2012-3993

Hartuç, T. (2015). *Boundary Layer Ingestion. Theoretical and Experimental Research* (Unpublished master's thesis). Delft University of Technology.

International Air Transport Association. (2018). *IATA Forecast Predicts 8.2 billion Air Travelers in 2037* (Tech. Rep.). Retrieved from https://www.iata.org/pressroom/pr/Pages/2018-10-24-02.aspx

Kawai, R. T., Friedman, D. M., & Serrano, L. (2006). Blended Wing Body (BWB) Boundary Layer

Ingestion (BLI) Inlet Configuration and System Studies. , 26. Retrieved from https://ntrs.nasa.gov/search.jsp?R=20070006754

Lieu, M. K. (2015). *Quantification of the Boundary Layer Ingestion Benefit for the D8-Series Aircraft Using a Pressure Rake System* (Master's thesis, Massachusetts Institute of Technology). Retrieved from http://hdl.handle.net/1721.1/97264

L.L.M. Veldhuis. (1988, April). *Support Interference Effects of a Ventral Sting on a Body of Revolution. A Brief Description of Phase 1* (Technical Report No. LSW 89-2). Delft University of Technology, Department of Aerospace Engineering.

Lv, L. (2019). *Theoretical and Experimental Investigation of Boundary Layer Ingestion for Aircraft Application* (PhD Thesis, Delft University of Technology). doi: doi:10.4233/uuid:6d8bd168-e057-4ee9-854c-32c84015e4c4

Lv, P., Ragni, D., Hartuc, T., Veldhuis, L., & Rao, A. G. (2017, April). Experimental Investigation of the Flow Mechanisms Associated with a Wake-Ingesting Propulsor. *AIAA Journal*, *55*(4), 1332–1342. Retrieved 2019-03-28, from https://arc.aiaa.org/doi/10.2514/1.J055292 doi: doi:10.2514/1.J055292

Lv, P., & Rao, A. G. (2013). Conceptual analysis of boundary layer ingestion towards aircraft propulsion integration. In (p. 16). Delft, The Netherlands. Retrieved from https://www.researchgate.net/publication/260433892_Conceptual_Analysis_of_Boundary_Layer_Ingestion_Towards_Aircraft_Propulsion_Integration

Lv, P., Rao, A. G., Ragni, D., & Veldhuis, L. (2016, September). Performance Analysis of Wake and Boundary-Layer Ingestion for Aircraft Design. *Journal of Aircraft*, *53*(5), 1517–1526. Retrieved 2019-01-25, from http://arc.aiaa.org/doi/10.2514/1.C033395 doi: doi:10.2514/1.C033395

McLemore, H. C. (1962). *Wind-tunnel tests of a 1/20-scale airship model with stern propellers* (Technical Report No. D-1026). NASA.

Plas, A. (2006). *Performance of a Boundary Layer Ingesting Propulsion System* (Unpublished master's thesis). Massachusetts Institute of Technology.

Plas, A., Crichton, D., Sargeant, M., Hynes, T., Greitzer, E., Hall, C., & Madani, V. (2007, January). Performance of a Boundary Layer Ingesting (BLI) Propulsion System. In *45th AIAA Aerospace Sciences Meeting and Exhibit*. Reno, Nevada: American Institute of Aeronautics and Astronautics. Retrieved 2019-01-25, from http://arc.aiaa.org/doi/10.2514/6.2007-450 doi: doi:10.2514/6.2007-450

Sabo, K. M., & Drela, M. (2015, January). Benefits of Boundary Layer Ingestion Propulsion. In *53rd AIAA Aerospace Sciences Meeting*. Kissimmee, Florida: American Institute of Aeronautics and Astronautics. Retrieved 2019-01-25, from http://arc.aiaa.org/doi/10.2514/6.2015-1667 doi: doi:10.2514/6.2015-1667

Sato, S. (2012). *The Power Balance Method For Aerodynamic Performance Assessment* (PhD Thesis). Massachusetts Institute of Technology.

Scarano, F. (2013). *Reader: Experimental Aerodynamics* (Vol. 1st). TU Delft.

Schlichting, H., & Gersten, K. (2016). *Boundary-layer theory*. New York, NY: Springer Berlin Heidelberg.

Sighard F. Hoerner. (1958). *Fluid-Dynamic Drag* (2nd ed.). Published by the author.

Siu, N. M. (2015). *Evaluation of Propulsor Aerodynamic Performance for Powered Aircraft Wind Tunnel Experiments* (Unpublished master's thesis). Massachusetts Institute of Technology.

Smith, A. (1947, February). The Jet Airplane Utilizing Boundary Layer Air for Propulsion. *Journal of the Aeronautical Sciences*, *14*(2), 97–109. Retrieved 2019-02-26, from https://doi.org/10.2514/8.1273 doi: doi:10.2514/8.1273

Smith, L. H. (1993, January). Wake ingestion propulsion benefit. *Journal of Propulsion and Power*, *9*(1), 74–82. Retrieved 2019-01-25, from http://arc.aiaa.org/doi/10.2514/3.11487 doi: doi:10.2514/3.11487

Uranga, A., Drela, M., Greitzer, E., Titchener, N., Lieu, M., Siu, N., ... Hannon, J. (2014, January). Preliminary Experimental Assessment of the Boundary Layer Ingestion Benefit for the D8 Aircraft. In *52nd Aerospace Sciences Meeting*. National Harbor, Maryland: American Institute of Aeronautics and Astronautics. Retrieved 2019-01-25, from http://arc.aiaa.org/doi/10.2514/6.2014-0906 doi: doi:10.2514/6.2014-0906

Uranga, A., Drela, M., Greitzer, E. M., Hall, D. K., Titchener, N. A., Lieu, M. K., ... Hannon, J. A. (2017, November). Boundary Layer Ingestion Benefit of the D8 Transport Aircraft. *AIAA Journal*, *55*(11), 3693–3708. Retrieved 2019-02-23, from https://arc.aiaa.org/doi/10.2514/1.J055755 doi: doi:10.2514/1.J055755

Uranga, A., Drela, M., Hall, D. K., & Greitzer, E. M. (2018, November). Analysis of the Aerodynamic Benefit from Boundary Layer Ingestion for Transport Aircraft. *AIAA Journal*, *56*(11),

4271–4281. Retrieved 2019-01-29, from https://arc.aiaa.org/doi/10.2514/1.J056781 doi: doi:10.2514/1.J056781

Van Dam, E. (2015). *Inlet Distortion Characterization of the Boundary Layer Ingesting D8 Aircraft. The NASA N+3 Project* (1 Master Thesis). Delft University of Technology.

Appendix A

Appendix

1 Technical Drawings

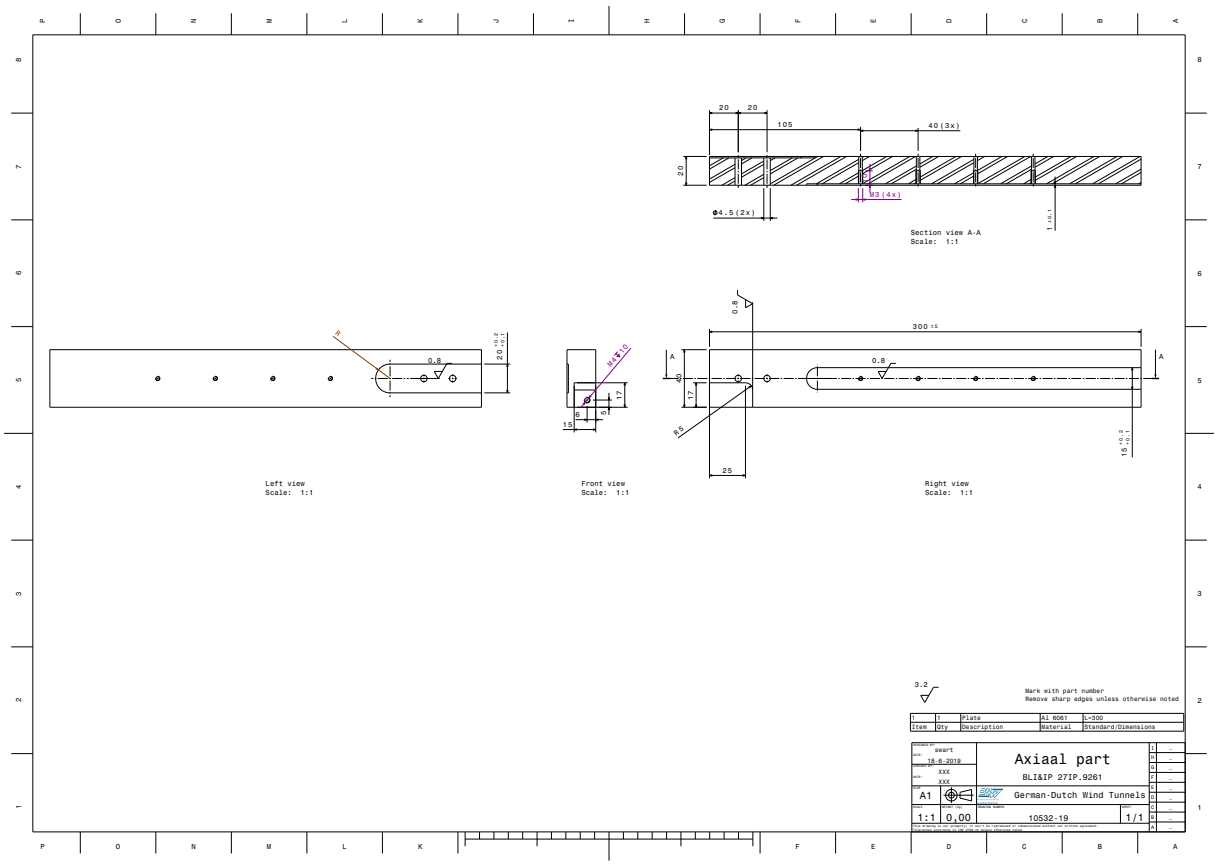

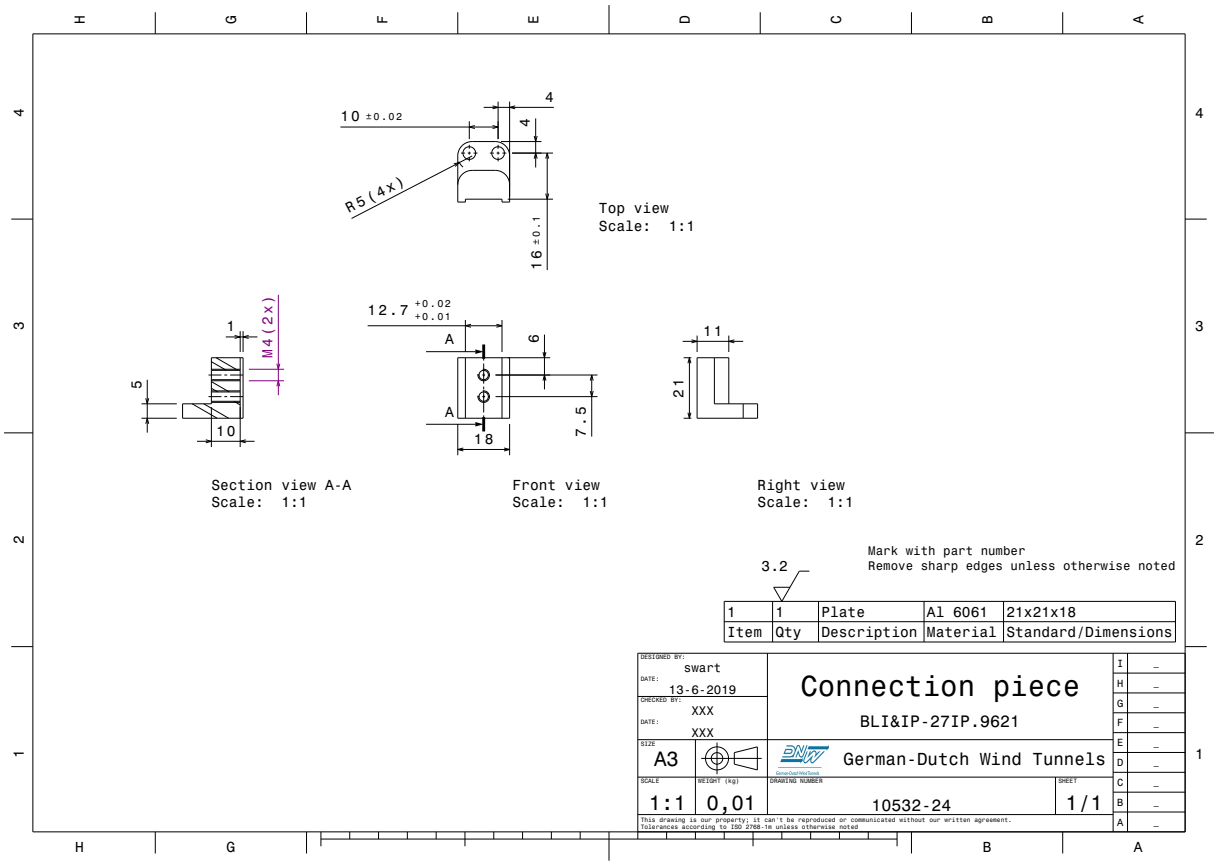
10 ±0.02
4
4
R5 (4x)
16 ±0.1
Top view
Scale: 1:1
1
M4 (2x)
5
10
Section view A-A
Scale: 1:1
12.7 +0.02 +0.01
A
6
A
18
7.5
Front view
Scale: 1:1
11
21
Right view
Scale: 1:1
Mark with part number
Remove sharp edges unless otherwise noted
3.2
1 | 1 | Plate | Al 6061 | 21x21x18
Item | Qty | Description | Material | Standard/Dimensions
DESIGNED BY: swart
DATE: 13-6-2019
CHECKED BY: XXX
DATE: XXX
Connection piece
BLI&IP-27IP.9621
SIZE A3
German-Dutch Wind Tunnels
SCALE 1:1
WEIGHT (kg) 0,01
DRAWING NUMBER 10532-24
SHEET 1/1
This drawing is our property; it can't be reproduced or communicated without our written agreement.
Tolerances according to ISO 2768-1m unless otherwise noted

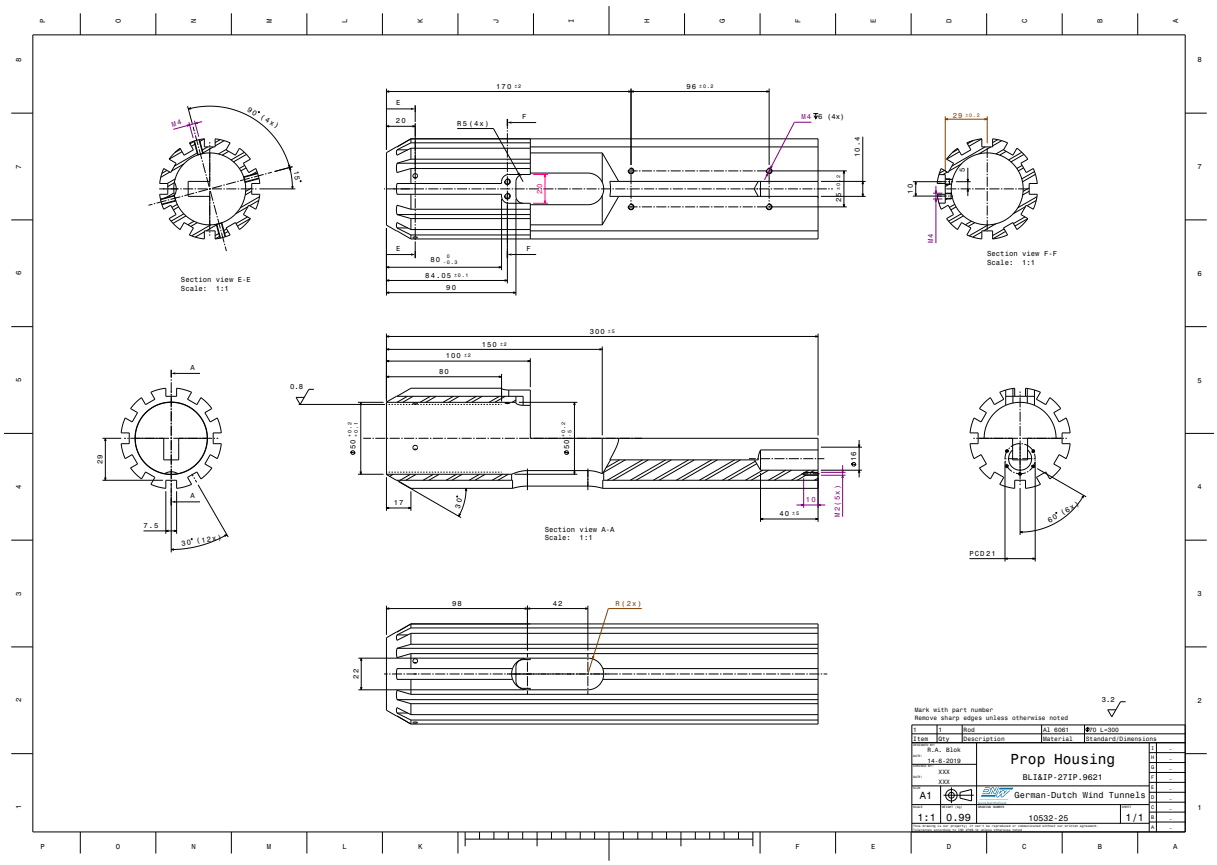
Section view E-E
Scale: 1:1
170 ±2
96 ±0.2
R5 (4x)
M4 ↧6 (4x)
80 0 -0.3
84.05 ±0.1
90
Section view F-F
Scale: 1:1
300 ±5
150 ±2
100 ±2
80
0.8
17
40 ±5
M21 (5x)
Section view A-A
Scale: 1:1
PCD21
98
42
R (2x)
Mark with part number
Remove sharp edges unless otherwise noted
3.2
1 | 1 | Rod | Al 6061 | Ø70 L=300
Item | Qty | Description | Material | Standard/Dimensions
R.A. Blok
14-6-2019
XXX
XXX
Prop Housing
BLI&IP-27IP.9621
A1
German-Dutch Wind Tunnels
1:1
0.99
10532-25
1/1

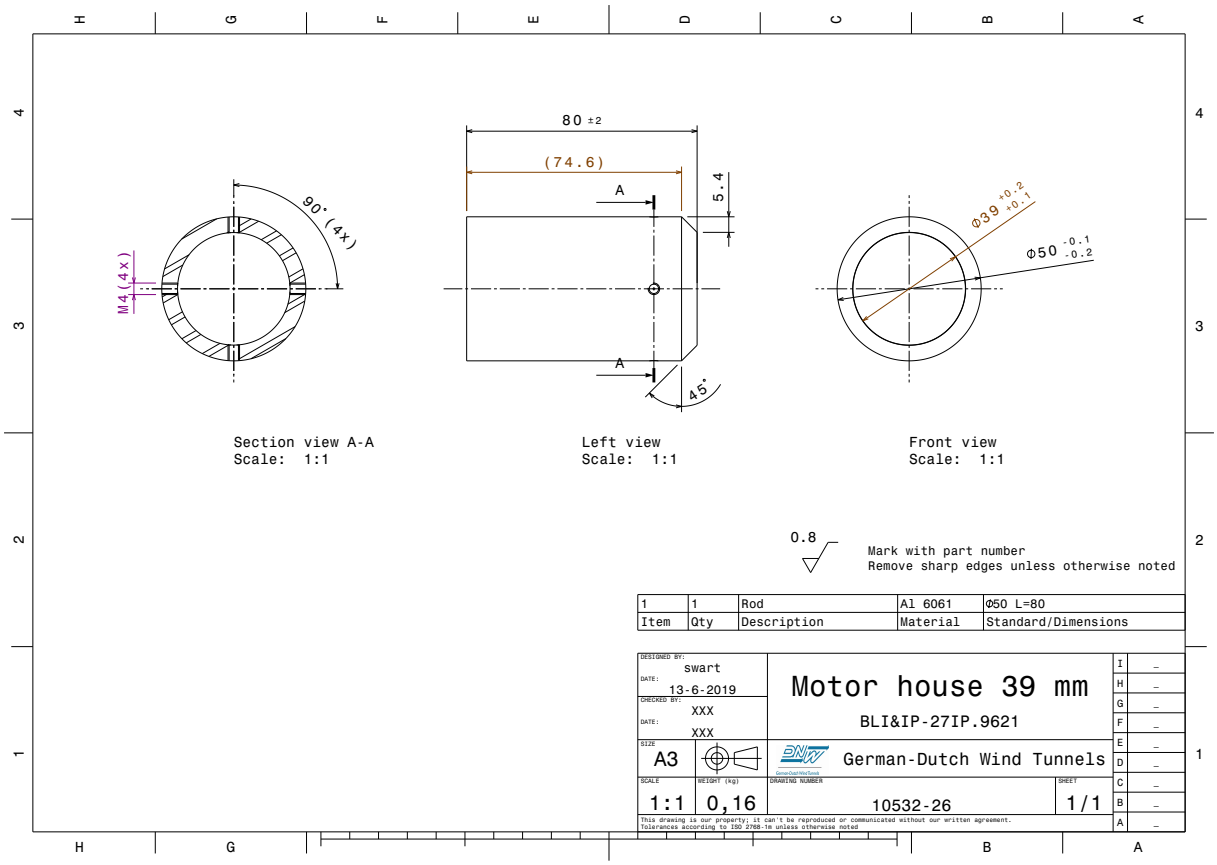
80 ±2
(74.6)
5.4
A
A
45°
90° (4x)
M4 (4x)
Ø39 +0.2 +0.1
Φ50 -0.1 -0.2
Section view A-A
Scale: 1:1
Left view
Scale: 1:1
Front view
Scale: 1:1
0.8
Mark with part number
Remove sharp edges unless otherwise noted
1 | 1 | Rod | Al 6061 | Φ50 L=80
Item | Qty | Description | Material | Standard/Dimensions
DESIGNED BY: swart
DATE: 13-6-2019
CHECKED BY: XXX
DATE: XXX
Motor house 39 mm
BLI&IP-27IP.9621
SIZE A3
German-Dutch Wind Tunnels
SCALE 1:1
WEIGHT (kg) 0,16
DRAWING NUMBER 10532-26
SHEET 1/1
This drawing is our property; it can't be reproduced or communicated without our written agreement.
Tolerances according to ISO 2768-1m unless otherwise noted

Appendix B

Calibration of load cells

The load cell calibration procedure is explained in this section. The body's load cell is tested by attaching a rope to the body and connecting it to a set of weights. Figure B.1 depicts the testing procedure. The weights were added consecutively, then then all the weights are taken off and again added randomly. This is to avoid any type of bias or hysteresis effect with the load cell. A 10 second integration time is taken per measurement. Figure B.2 shows the calibration curve comparing the measured values against the actual values.

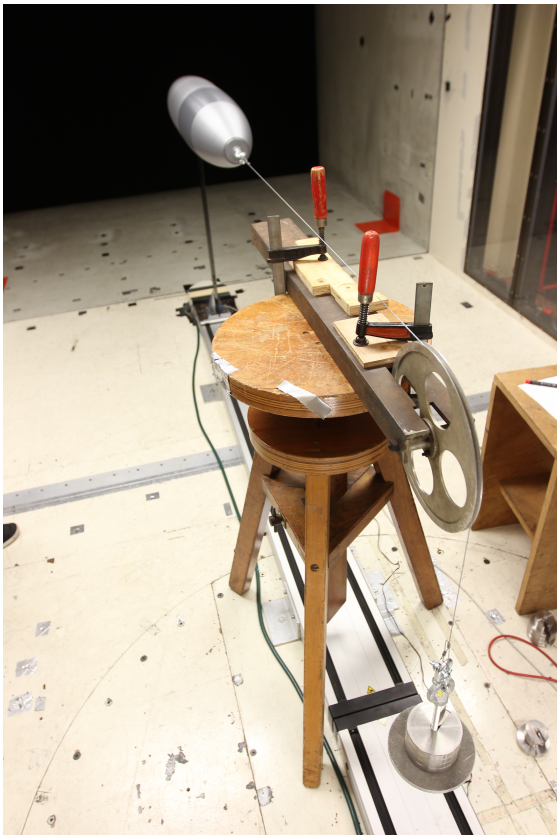

Figure B.1: Calibration of the body's load cell

Figure B.3 shows the set-up for the load cell calibration of the propulsor. The load cell was tested in the same manner as the load cell of the body. The calibration curve is shown in Figure B.4. It can be concluded that for both load cells deviate 0.98% from the true value.

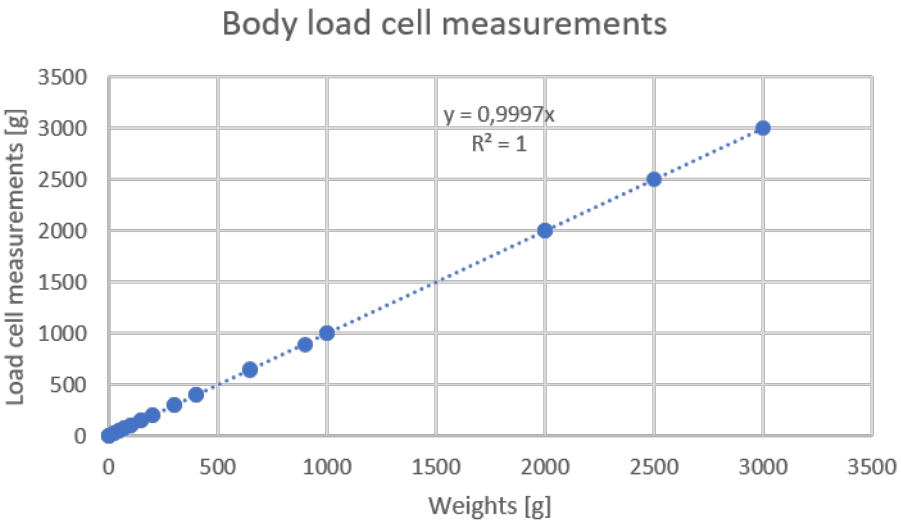

Figure B.2: Load cell calibration curve

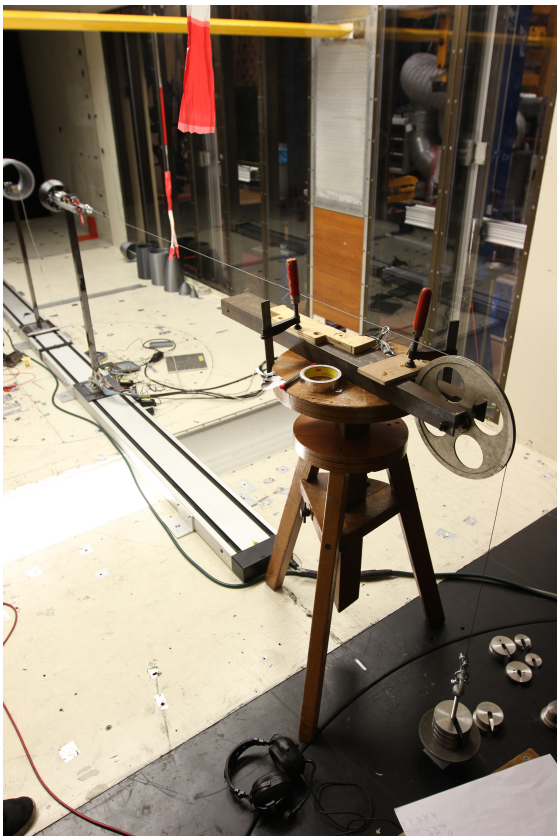

Figure B.3: Calibration of the propulsor's load cell

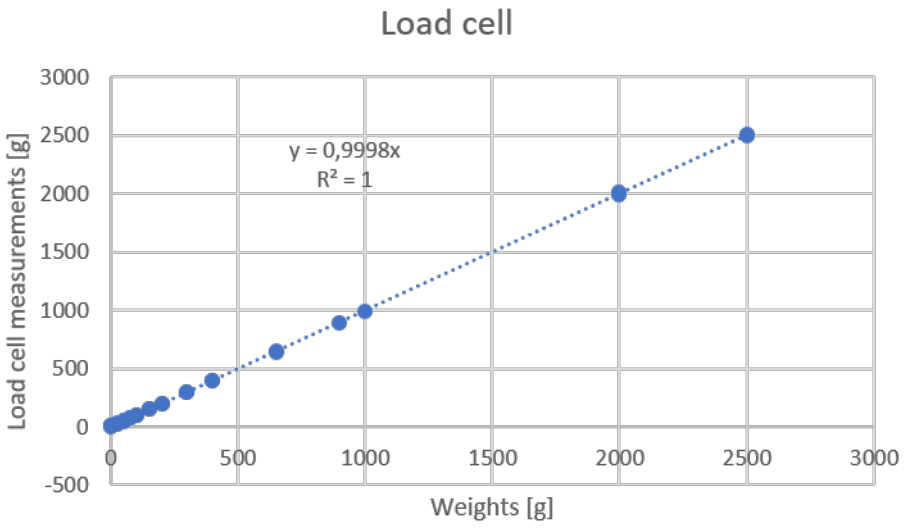

Figure B.4: Load cell calibration curve

Appendix C

Particle Image Velocimetry

Experimental testing is carried at wind tunnels to understand the flow physics. There are several techniques to measure the flow velocities and they are divided in two groups: intrusive and non-intrusive. Examples for intrusive measurement techniques are Pitot tubes and hot-wire anemometry. On the other hand, examples for non-intrusive techniques are laser Doppler velocimetry and Particle Image Velocimetry (PIV).

PIV consists on the measurement of the displacement of small particles, also named tracer particles, that are carried by the fluid (air in the case of a wind tunnel) during a short time interval. The tracer particles must be sufficiently small to precisely follow the air motion and not alter the flow characteristics. The tracer particles are illuminated by a thin laser sheet generated from a laser (pulsed light source). The laser light is then scattered by the tracer particles and recorded by a digital camera. Two images are taken within a short time interval. With these two images the particle's flow velocity can be determined. Figure C.1 shows a schematic of a PIV set-up. (Scarano, 2013)

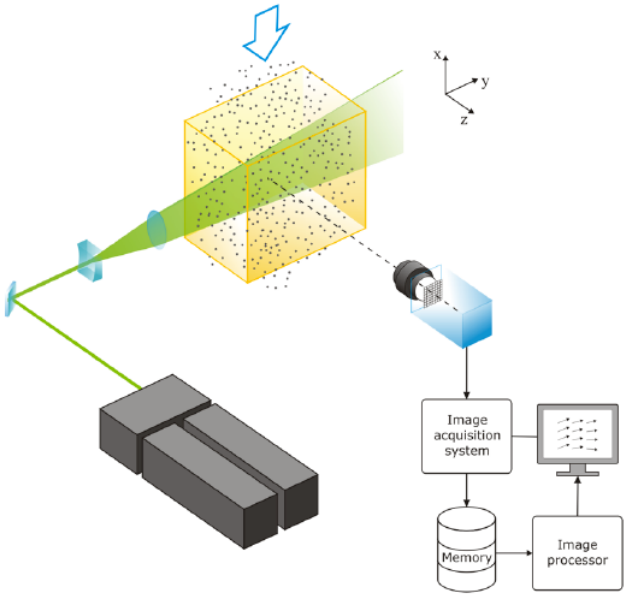

Figure C.1: Schematic of a PIV system (Scarano, 2013)

For the purpose of this research the three components of velocity were needed. Therefore, stereoscopic imaging was necessary. Stereoscopic imaging means that there are two simultaneous views (two CCD cameras for example) on the planar field defined by the light sheet. The advantage of PIV is that it is a non-intrusive measurement technique, therefore it does not influence the flow characteristics. However, it does require optical access for the cameras and the light sheet. The test set-up for this experiment

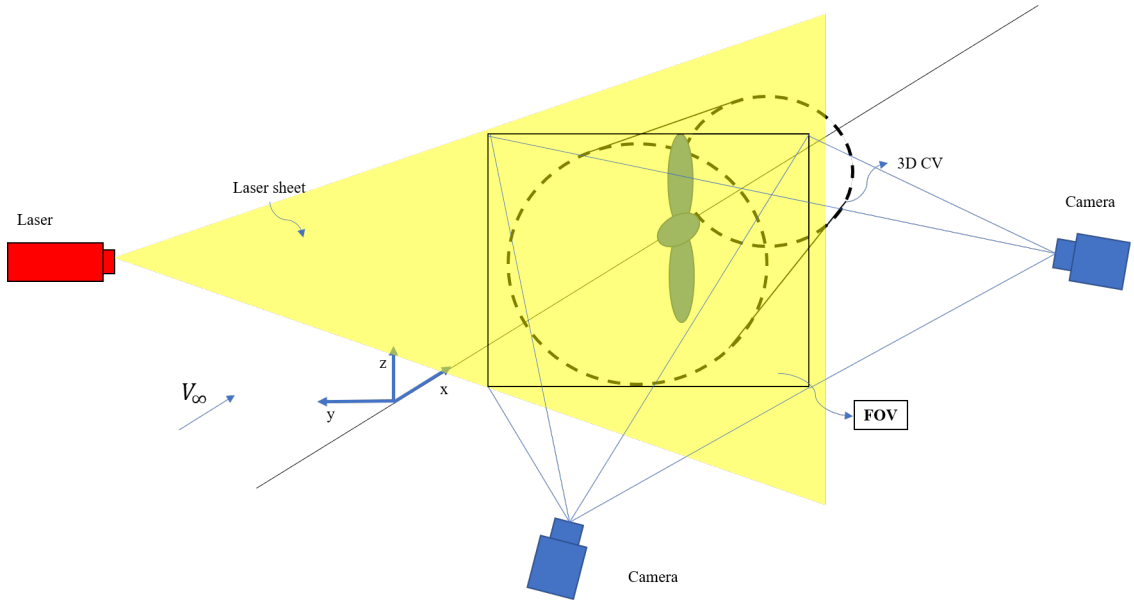

Figure C.2: Stereoscopic PIV set-up intended for measuring the three components of flow velocity at inlet and outlet planes of the propulsor

consisted in measuring two planes, one at the front of the propulsor and one at the back, as shown in Figure C.2. The reason for these measurements is to check the axisymmetry of the flow and validate the five-hole probe measurements.

With the rail system, the entire configuration can be shifted upstream or downstream. Thus, there is no need to set-up and calibrate the PIV cameras several times. Since setting up the PIV system requires considerable time, shifting the entire model reduces significantly the time constructing and calibrating the system. The PIV test set-up is summarized in Table C.1. The installed cameras can be observed in Figure C.3. *Unfortunately the Evergreen laser was broken, thus PIV measurements were not possible to be carried out.*

Table C.1: System parameters of the stereoscopic PIV

Lenses	105 mm
Scale factor:	5.80687px/mm
Cameras	sCMOS 2560(width)x2160(height)
Pixel size:	6.5 micrometers
Laser:	Evergreen 200
FoV width	530.6 mm
FoV height	375.4 mm
Seeding system	DEHS = di-ethyl-hexyl-sebacate

Figure C.3: sCMOS cameras set-up outside the wind tunnel walls